

Optical coherence tomography - principles and applications

To cite this article: A F Fercher *et al* 2003 *Rep. Prog. Phys.* **66** 239

View the [article online](#) for updates and enhancements.

Related content

- [Theory, developments and applications of optical coherence tomography](#)
- [Advances in broad bandwidth light sources for ultrahigh resolution optical coherence tomography](#)
- [Image processing techniques for noise removal, enhancement and segmentation of cartilage OCT images](#)

Recent citations

- [Coherent Stokes and anti-Stokes high-order components generation by biharmonic pumping via stimulated low-frequency Raman scattering](#)
M.A. Shevchenko *et al*
- [Sandra J. Perdomo *et al*](#)
- [Model Test on the Soil Arching Effect of Pile-Supported Embankments Using Transparent Soil](#)
Xuanming Ding *et al*



IOP | ebooks™

Bringing together innovative digital publishing with leading authors from the global scientific community.

Start exploring the collection—download the first chapter of every title for free.

Optical coherence tomography—principles and applications

A F Fercher¹, W Drexler¹, C K Hitzenberger¹ and T Lasser²

¹ Institute of Medical Physics, University of Vienna, Waehringer Strasse 13, A-1090 Wien, Austria

² Laboratoire d'optique biomédicale, Institut d'imagerie et optique appliquée, EPFL Lausanne, CH-1015 Ecublens, Switzerland

E-mail: adolf.friedrich.fercher@univie.ac.at

Received 23 October 2002

Published 20 January 2003

Online at stacks.iop.org/RoPP/66/239

Abstract

There have been three basic approaches to optical tomography since the early 1980s: diffraction tomography, diffuse optical tomography and optical coherence tomography (OCT). Optical techniques are of particular importance in the medical field, because these techniques promise to be safe and cheap and, in addition, offer a therapeutic potential. Advances in OCT technology have made it possible to apply OCT in a wide variety of applications but medical applications are still dominating. Specific advantages of OCT are its high depth and transversal resolution, the fact, that its depth resolution is decoupled from transverse resolution, high probing depth in scattering media, contact-free and non-invasive operation, and the possibility to create various function dependent image contrasting methods. This report presents the principles of OCT and the state of important OCT applications.

OCT synthesises cross-sectional images from a series of laterally adjacent depth-scans. At present OCT is used in three different fields of optical imaging, in macroscopic imaging of structures which can be seen by the naked eye or using weak magnifications, in microscopic imaging using magnifications up to the classical limit of microscopic resolution and in endoscopic imaging, using low and medium magnification. First, OCT techniques, like the reflectometry technique and the dual beam technique were based on time-domain low coherence interferometry depth-scans. Later, Fourier-domain techniques have been developed and led to new imaging schemes. Recently developed parallel OCT schemes eliminate the need for lateral scanning and, therefore, dramatically increase the imaging rate. These schemes use CCD cameras and CMOS detector arrays as photodetectors. Video-rate three-dimensional OCT pictures have been obtained. Modifying interference microscopy techniques has led to high-resolution optical coherence microscopy that achieved sub-micrometre resolution.

This report is concluded with a short presentation of important OCT applications. Ophthalmology is, due to the transparent ocular structures, still the main field of OCT application. The first commercial instrument too has been introduced for ophthalmic

diagnostics (Carl Zeiss Meditec AG). Advances in using near-infrared light, however, opened the path for OCT imaging in strongly scattering tissues. Today, optical *in vivo* biopsy is one of the most challenging fields of OCT application. High resolution, high penetration depth, and its potential for functional imaging attribute to OCT an optical biopsy quality, which can be used to assess tissue and cell function and morphology *in situ*. OCT can already clarify the relevant architectural tissue morphology. For many diseases, however, including cancer in its early stages, higher resolution is necessary. New broad-bandwidth light sources, like photonic crystal fibres and superfluorescent fibre sources, and new contrasting techniques, give access to new sample properties and unmatched sensitivity and resolution.

Contents

	Page
1. Introduction	243
1.1. Basic schemes	243
1.2. Mathematical treatment	245
2. OCT signal properties	246
2.1. Single scattering and optical tomography	246
2.2. Multiple scattered sample light	250
2.3. Probing depth	251
2.4. Sensitivity	253
2.5. Speckle	254
2.5.1. Speckle properties	254
2.5.2. Interferogram speckle	256
2.5.3. Suppression of speckle in OCT	256
2.6. Resolution	257
2.6.1. OCT PSF and resolution	257
2.6.2. Deconvolution	259
2.6.3. Dispersion compensation	259
2.6.4. Limited diffraction beams	260
3. OCT light sources	260
3.1. Coherence properties	260
3.2. Wavelength	261
3.3. Spectral structure	264
3.3.1. Spectral width	264
3.3.2. Spectral modulation	265
3.3.3. Spectral phase	265
4. Low-coherence interferometry and OCT	266
4.1. Time-domain OCT	266
4.1.1. Reflectometry OCT	266
4.1.2. Dual beam OCT	269
4.1.3. <i>En-face</i> OCT	269
4.1.4. Heterodyne detection and delay lines	269
4.2. Fourier-domain OCT	271
4.2.1. Spectral interferometry Fourier-domain OCT	271
4.2.2. Wavelength tuning Fourier-domain OCT	274
4.3. Parallel OCT	275
5. Functional OCT	276
5.1. Polarization-sensitive OCT	277
5.2. Doppler OCT	280
5.2.1. Fourier-transforming the fringe data	282
5.2.2. Sequential scan processing	283
5.2.3. Fourier-domain DOCT	284

5.2.4. Hardware solutions	284
5.3. Wavelength-dependent OCT	285
5.3.1. Spectrometric OCT	286
5.3.2. Fourier-domain SOCT	287
5.3.3. Differential absorption OCT	287
5.3.4. Coherence spectrotomography	288
5.3.5. Refractometric OCT	289
6. Applications of OCT	290
6.1. OCT in ophthalmology	291
6.2. Other medical fields: OCT biopsy and functional OCT	292
6.2.1. High-resolution OCT in gastroenterology and dermatology	292
6.2.2. Endoscopic OCT in intra-arterial imaging	295
6.2.3. PS-OCT in dentistry	295
6.2.4. Spectroscopic OCT in gastroenterology	296
6.2.5. DOCT in haemostatic therapy	297
6.3. Non-medical OCT	297
Acknowledgments	298
References	298

1. Introduction

Tomographic techniques generate slice images of three-dimensional objects. Optical tomographic techniques are of particular importance in the medical field, because these techniques can provide non-invasive diagnostic images. There is a fundamental difference between optical tomography techniques and x-ray and magnetic resonance techniques. Since optical techniques are dominated by diffraction the Fourier slice theorem cannot be used. There are two fundamental optical tomography techniques: diffuse optical tomography (DOT), and optical diffraction tomography (ODT). Optical coherence tomography (OCT) is physically founded on ODT. The vast majority of applications of these techniques is in the biomedical field.

DOT uses diffusely propagating photons. Spatially and/or temporally modulated light is launched into the tissue and multiple scattered. Back-projection methods, perturbation methods, and nonlinear optimization methods are used to derive tomographic images from the transmitted light (Arridge and Schweiger 1997, Depeursinge 2002). ODT uses single scattered light and derives tomographic images by the Fourier diffraction projection theorem (Born and Wolf 1999). Recently, it has been shown, that standard diffraction tomographic methods can also be used for imaging with diffuse-photon density waves (Li *et al* 1997).

OCT uses ballistic and near-ballistic photons. Laterally adjacent depth-scans (similar to the more familiar A-scans of ultrasound imaging technology) are used to obtain a two-dimensional map of reflection sites in a sample. Initially, OCT techniques were based on low time-coherence interferometry (LCI) depth-scans performed in the time domain. In a first approach towards tomographic imaging a cross-sectional topographic image of the retinal pigment epithelium (RPE) of a human eye obtained *in vivo* by the dual beam LCI technique was presented at the ICO-15 SAT conference by Fercher (1990) and published by Hitzenberger (1991). OCT using fibre optic Michelson LCI was pioneered by Fujimoto and co-workers (Huang *et al* 1991). First *in vivo* tomograms of the human retina were published by Fercher *et al* (1993a) and Swanson *et al* (1993). Later Chinn *et al* (1997) used wavelength tuning interferometry (WTI) to synthesize OCT images, whereas Häusler and Lindner (1998) generated OCT images using spectral interferometry. For a review of early work in LCI and OCT see the selection of key papers published by Masters (2001).

1.1. Basic schemes

Figure 1 depicts the standard OCT scheme. A low time-coherence light source is used in a standard Michelson interferometer. Note that there are basically two scan procedures in OCT: the OCT depth-scan is performed by the reference mirror. The lateral OCT scan is either performed by moving the sample or by scanning the probe beam illuminating the sample.

OCT synthesizes cross-sectional images from a series of adjacent LCI depth-scans. In contrast to classical interferometry, LCI measures absolute distances. LCI is based on the occurrence of fringes if the optical path lengths of reference and sample beams coincide within the ‘coherence gate’, which is of the size of the so-called round trip coherence length l_C :

$$l_C = \frac{2 \ln 2}{\pi} \frac{\bar{\lambda}^2}{\Delta\lambda}, \quad (1.1)$$

where $\bar{\lambda}$ is the mean wavelength and $\Delta\lambda$ the spectral width (Gaussian spectrum assumed; see section 4.1.1). For example, using a superluminescent light diode (SLD) as a low time-coherence light source and data from table 1 ($\bar{\lambda} = 820$, $\Delta\lambda = 20$ nm) yields a round trip coherence length and thus depth resolution (see also section 2.6.1) of $l_C \approx 15$ μ m.

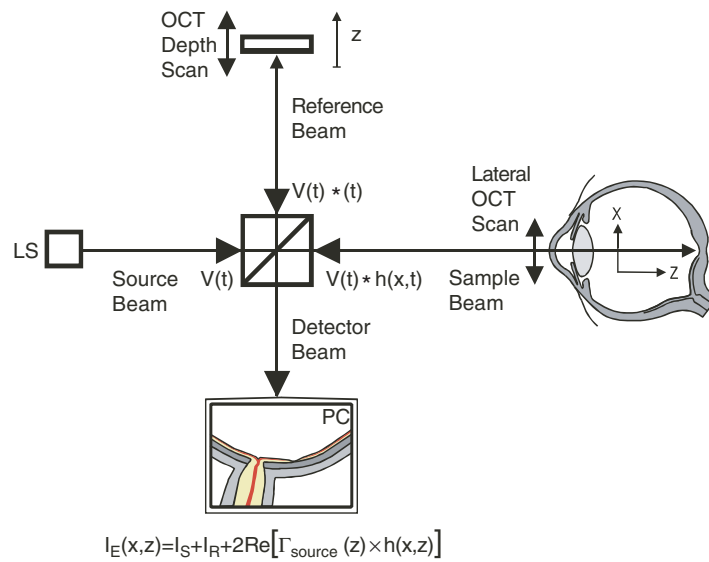


Figure 1. Standard OCT scheme based on a low time-coherence Michelson interferometer. The intensity I_E at the interferometer exit depends on the sample response $h(x, z)$ convolved with the source coherence function $\Gamma_{\text{Source}}(z)$. LS = low time-coherence light source; PC = personal computer.

OCT has, therefore, some outstanding properties: first of all, depth resolution is decoupled from transverse resolution. High depth resolution is possible even at sites not accessible by high numerical aperture (NA) beams, like the fundus of the eye. If, however, high NA beams can be used, high transversal resolution is obtained too; this technique is called optical coherence microscopy (OCM). Second, depth resolution in the histological $1 \mu\text{m}$ range is possible. Third, the interferometric technique provides high dynamic range and sensitivity ($> 100 \text{ dB}$). Imaging of weakly scattering structures even in a scattering environment is possible, enabling ‘*in situ* optical biopsy’. Last, but not the least, it is important to note that in medical terms LCI and OCT are non-invasive techniques that yield *in vivo* data.

At present, OCT uses exclusively time-coherence properties. There are, however, first attempts towards space-coherence OCT. A corresponding technique using a space-coherence gate has recently been investigated by Rosen and Takeda (2000). These authors suggested that the spatial spectrum of the beam illuminating the object be varied by spatial masks in order to use the longitudinal component of the spatial coherence as a coherence gate for depth ranging. In a first demonstration Fresnel zone plate structures have been used to move the coherence gate. An advantage of this technique is that it is independent of the source spectrum. The disadvantage of the technique is, however, that depth resolution becomes dependent on the NA, as in classical imaging.

Also, OCT uses exclusively linear optics at present. Two-photon interferometry, however, has just been shown to have the potential of still higher sensitivity, furthermore, to have the potential of an enhancement of depth resolution by a factor of two, and of cancellation of dispersion. The two-photon interferometer makes use of a nonclassical entangled or correlated twin-photon light source. How far this so-called ‘quantum-OCT’ can replace existing linear interferometry techniques will largely depend on the practicability of the spontaneous parametric down-conversion light sources needed in that technique (Abouraddy *et al* 2002).

1.2. Mathematical treatment

In this chapter we shall represent light waves as scalar, stationary, ergodic, random analytic signals and follow the treatment given by Mandel and Wolf (1995). We shall also ignore field quantization and polarization (except in section 5.1) and use the following Fourier transform (FT) representation of the electric field $E(t)$:

$$\hat{E}(\nu) = \int_{-\infty}^{\infty} E(t) \exp(2\pi i \nu t) dt = \text{FT}\{E(t)\} \quad (1.2)$$

with the corresponding analytic signal

$$V(t) = 2 \int_0^{\infty} \hat{E}(\nu) \exp(-2\pi i \nu t) d\nu = A(t) \exp[i\Phi(t) - 2\pi i \bar{\nu} t], \quad (1.3)$$

$A(t) e^{i\Phi(t)}$ is the complex envelope of $V(t)$, $A(t) = |V(t)|$ the real envelope, and $\bar{\nu}$ the mean frequency of the power spectrum of $V(t)$. Furthermore, we define the instantaneous intensity by

$$I(t) = V^*(t) V(t). \quad (1.4)$$

We shall furthermore describe interference phenomena of light waves as second-order correlation phenomena. The mutual coherence function of such light waves V_S (sample wave) and V_R (reference wave) is a second-order cross-correlation function,

$$\Gamma_{SR}(\tau) = \langle V_S^*(t) V_R(t + \tau) \rangle, \quad (1.5)$$

where the angle brackets mean ensemble average. Since we are concerned with stationary and ergodic waves, all ensemble averages are independent of the origin of time and may be replaced by time-averages. The averaged intensity is the auto-correlation $\text{ACF}_V(\tau)$ at $\tau = 0$:

$$\bar{I} = \langle I(t) \rangle = \langle V^*(t) V(t + \tau) \rangle|_{\tau=0} = \text{ACF}_V(\tau)|_{\tau=0} = \Gamma(\tau)|_{\tau=0}. \quad (1.6)$$

We shall make extensive use of the interference law: after introducing a time delay Δt , light from a sample beam interferes with light from a reference beam at the interferometer exit (index E):

$$V_E(t; \Delta t) = V_S(t) + V_R(t + \Delta t). \quad (1.7)$$

The averaged intensity at the interferometer exit is

$$\begin{aligned} \bar{I}_E(\Delta t) &= \langle I_E(t; \Delta t) \rangle = \Gamma_{EE}(0; \Delta t) = \langle V_E^*(t; \Delta t) V_E(t; \Delta t) \rangle \\ &= \langle I_S(t) \rangle + \langle I_R(t) \rangle + G_{SR}(\Delta t). \end{aligned} \quad (1.8)$$

The interferogram $G_{SR}(\Delta t)$ is twice the real part of the cross-correlation of the analytic signals of the two interfering beams:

$$\begin{aligned} G_{SR}(\Delta t) &= 2\text{Re} \{ \langle V_S^*(t) V_R(t + \Delta t) \rangle \} = 2\text{Re} \{ \Gamma_{SR}(\Delta t) \} \\ &= 2\sqrt{\langle I_S(t) \rangle \langle I_R(t) \rangle} |\gamma_{SR}(\Delta t)| \cos[\alpha_{SR} - \delta_{SR}(\Delta t)]. \end{aligned} \quad (1.9)$$

$\gamma_{SR}(\Delta t)$ is the complex degree of coherence of the two waves, $|\gamma_{SR}(\Delta t)|$ is their degree of coherence; $\delta_{SR}(\Delta t) = 2\pi \bar{\nu} \Delta t$ is the phase delay, $\Delta t = (\Delta z/c)$ the time delay, Δz the path difference between the beams and c the speed of light. α_{SR} is a constant phase.

Since $\Gamma(\tau)$ is an analytic function it can be obtained from its real part $G(\tau) = 2\text{Re}\{\langle V^*(t) V(t + \tau) \rangle\}$ by analytic continuation:

$$\Gamma(\tau) = \frac{1}{2} G(\tau) + \frac{i}{2} \text{HT}\{G(\tau)\}, \quad (1.10)$$

where HT means Hilbert transform, and $G(\tau)$ is obtained from the LCI signal.

LCI and OCT are based on the photoelectric signal $U_G(t)$ of the interferogram G_{SR} in a low-coherence interferometer (obtained by band-pass filtering of the photoelectric heterodyne interferometer ac signal). Photodiodes are generally used as detectors as they can provide near-shot-noise limited operation in OCT configurations. The photodiode signal is measured as current because of its better linearity, offset, and bandwidth performance compared to voltage measurement. The generated photocurrent is proportional to the incident light power and is converted to voltage using a transimpedance electronic amplifier circuit. We shall call $U_G(t)$, and, sometimes, just G_{SR} , the ‘LCI signal’ or ‘OCT signal’:

$$U_G(t) \propto i_G(t) = \frac{q_e \eta}{h \bar{\nu}} \int_{Ar(\mathbf{r})} G_{SR}(\mathbf{r}, t) d^2\mathbf{r}, \quad (1.11)$$

$i_G(t)$ is the photoelectric current, q_e the electronic charge, η the quantum efficiency of the detector, h the Planck’s constant, $\bar{\nu}$ the mean optical frequency, and $Ar(\mathbf{r})$ the sensitive detector area. Frequently, the envelope of the LCI signal is generated by rectification of the photoelectric ac signal followed by low-pass filtering. Alternatively, amplitude and phase (or the corresponding quadrature components) of the photoelectric ac signal are determined using a lock-in amplifier.

If the photodetector surface at the interferometer exit is coplanar with the wavefronts of the interfering beams, we have

$$G_{SR}(\mathbf{r}, t) = G_{SR}(t) \propto i_G(t) \quad (1.12)$$

and obtain the real envelope of the coherence function $\Gamma_{SR}(t) = A_\Gamma(t) e^{i\Phi_\Gamma(t)}$ from

$$A_\Gamma(t) = \frac{1}{2} \sqrt{(G_{SR}(t))^2 + (\text{HT}\{G_{SR}(t)\})^2} \quad (1.13)$$

and its phase from

$$\Phi_\Gamma(t) = \arctan \left[\frac{\text{HT}\{G_{SR}(t)\}}{G_{SR}(t)} \right]. \quad (1.14)$$

Finally, we shall use the corresponding spectral relations; these are obtained with the help of the Wiener–Khinchine theorem. First, we note that the power spectrum of a light wave is obtained as the FT of its self-correlation:

$$S(\nu) = \text{FT}\{\Gamma(\tau)\}. \quad (1.15)$$

Furthermore, the cross-spectral density function of two waves (V_S and V_R) is obtained as the FT of the cross-correlation function:

$$W_{SR}(\nu) = \text{FT}\{\Gamma_{SR}(\tau)\}, \quad (1.16)$$

and the spectral interference law is obtained as

$$S(\nu; \Delta t) = S_S(\nu) + S_R(\nu) + 2\text{Re}[W_{SR}(\nu)] \cos(2\pi \nu \Delta t), \quad (1.17)$$

with the interferometric time delay Δt .

2. OCT signal properties

2.1. Single scattering and optical tomography

Unscattered photons like x-rays and γ -rays have been used to obtain tomographic straight ray projections for a long time. The mathematical problem of reconstructing a function from its straight ray projections has already been presented by Radon (1917). Its solution, the Fourier slice theorem, shows that some of the three-dimensional Fourier data of the object can be obtained from two-dimensional FTs of its projections. Because of its analogy to the Fourier

diffraction theorem (Wolf 1969), we shall have a closer look at this theorem: from the FT of an object function $F(x, y, z)$ (which, e.g. in x-ray computer tomography (CT) characterizes the two-dimensional distribution of the linear x-ray attenuation coefficient),

$$\hat{F}(u, v, w) = \text{FT}\{F(x, y, z)\} = \iiint F(x, y, z) \exp[2\pi i(ux + vy + wz)] dx dy dz, \quad (2.1)$$

it follows readily, that the projection $P(x, y) = \int F(x, y, z) dz$ has the two-dimensional FT

$$\text{FT}_{x,y}\{P(x, y)\} = \iint \left\{ \int F(x, y, z) dz \right\} \exp[2\pi i(ux + vy)] dx dy = \hat{F}(u, v, 0). \quad (2.2)$$

Hence, slices of the three-dimensional Fourier data of the object can be obtained from a FT of its two-dimensional projections. In the CT technique, a series of such projections at different directions is used to obtain depth resolution. To correct for the radial dependence of the Fourier data density introduced by the projection procedure a filtering step is applied (Kak and Slaney 1988).

Optical tomography techniques and, in particular, OCT, deviate in several respects from that more known CT concept: (1) DOT uses highly diffracted and scattered radiation; straight ray propagation can only be assumed for a fraction of the photons; the reconstruction algorithm must take care of diffraction. (2) OCT images are synthesized from a series of adjacent interferometric depth-scans performed by a straight propagating low-coherence probing beam; that leads to an advantageous decoupling of transversal resolution from depth resolution. (3) OCT uses backscattering; light propagates twice through the same object region.

Figure 2 depicts two implementations of OCT. A rotating mirror is used to provide the lateral OCT scan. Note that, to implement the confocal scheme too (the core diameter of single-mode fibres is approximately $5 \mu\text{m}$) a pinhole is used in front of the photodetector in the free-space optics scheme). Thus, light from outside the sample focus volume is suppressed.

Let us consider a weakly inhomogeneous sample illuminated by the waist of an optical Gaussian probe beam. Hence, within a depth extension of the order of magnitude of the Rayleigh length we can assume plane-wave illumination with incident waves:

$$V^{(i)}(\mathbf{r}, \mathbf{k}^{(i)}, t) = A^{(i)} \exp(i\mathbf{k}^{(i)} \cdot \mathbf{r} - i\omega t), \quad (2.3)$$

$\mathbf{k}^{(i)}$ is the wave vector of the illuminating wave, $|\mathbf{k}^{(i)}| = k = 2\pi/\lambda$ the wave number.

Then, using the outgoing free-space Green's function $G_H(\mathbf{r}, \mathbf{r}') = (e^{ik|\mathbf{r}-\mathbf{r}'|}/|\mathbf{r}-\mathbf{r}'|)$ of the Helmholtz operator, the first-order Born approximation yields the scattered wave as an approximate solution of the Helmholtz equation (Wolf 1969, Born and Wolf 1999):

$$V_S(\mathbf{r}, \mathbf{k}^{(s)}, t) = V^{(i)}(\mathbf{r}, \mathbf{k}^{(i)}, t) + \frac{1}{4\pi} \int_{\text{Vol}(\mathbf{r}')} V^{(i)}(\mathbf{r}', \mathbf{k}^{(i)}, t) \cdot F_S(\mathbf{r}', k) \cdot G_H(\mathbf{r}, \mathbf{r}') \cdot d^3\mathbf{r}'. \quad (2.4)$$

$\mathbf{k}^{(s)}$ is the wave vector of the scattered wave, $|\mathbf{k}^{(s)}| = k$. This integral is extended over wavelets originating from the illuminated sample volume $\text{Vol}(\mathbf{r}')$. The relative amplitudes of these wavelets are determined by the scattering potential of the sample

$$F_S(\mathbf{r}, k) = k^2[m^2(\mathbf{r}, k) - 1], \quad (2.5)$$

where m is the complex refractive index distribution of the sample structure:

$$m(\mathbf{r}) = n(\mathbf{r})[1 + i\kappa(\mathbf{r})], \quad (2.6)$$

with $n(\mathbf{r})$ being the phase refractive index, and $\kappa(\mathbf{r})$ the attenuation index.

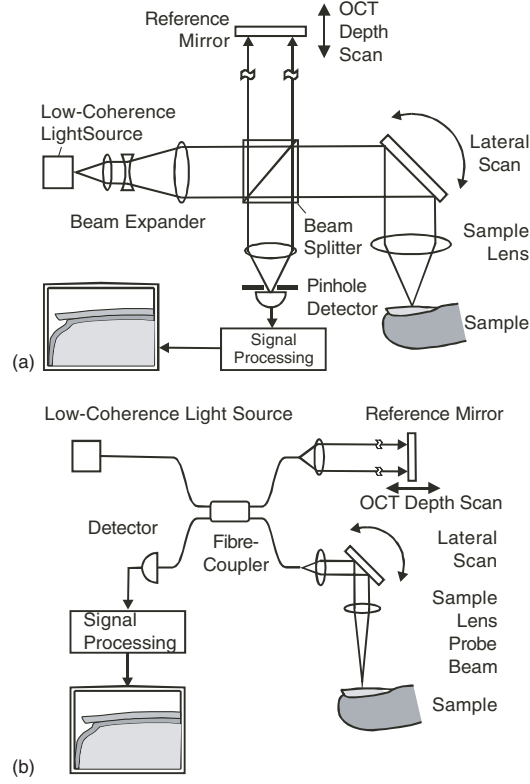


Figure 2. (a) Free-space optics and (b) (single-mode) fibre optics implementation of OCT.

In LCI and OCT, backscattered light originating from the coherently illuminated sample volume is detected at a distance d much larger than the linear dimensions of that volume. Therefore, the scattered wave $V_S(\mathbf{r}, \mathbf{k}^{(s)}, t)$ at d can be written as (Fercher *et al* 1995):

$$V_S(\mathbf{r}, \mathbf{K}, t) = \frac{A^{(i)}}{4\pi d} \exp(i\mathbf{k}^{(s)} \cdot \mathbf{r} - i\omega t) \int_{\text{Vol}(\mathbf{r}')} F_S(\mathbf{r}') \cdot \exp(-i\mathbf{K} \cdot \mathbf{r}') \cdot d^3\mathbf{r}', \quad (2.7)$$

where the amplitude $A^{(i)}$ of the illuminating wave has been assumed constant within the coherent probe volume.

$$\mathbf{K} = \mathbf{k}^{(s)} - \mathbf{k}^{(i)} \quad (2.8)$$

is the scattering vector (see figure 3). Hence, in the far field approximation the amplitude of the scattered sample wave A_S is proportional to the three-dimensional inverse FT (using $\mathbf{K}/2\pi$ as the Fourier variable) of the sample scattering potential F_S :

$$A_S(\mathbf{r}, \mathbf{k}^{(s)}, t) = \frac{A^{(i)}}{4\pi d} \int_{\text{Vol}(\mathbf{r}')} F_S(\mathbf{r}') \cdot \exp(-i\mathbf{K} \cdot \mathbf{r}') \cdot d^3\mathbf{r}' \propto \text{FT}^{-1}\{F_S(\mathbf{r}')\}. \quad (2.9)$$

This result is a simplified version of the basic theorem of diffraction tomography (Born and Wolf 1999): the scattering potential is simply obtained by a Fourier inversion of the scattered field data.

From equation (2.8) and figure 3 it can be seen that all Fourier components of the scattering potential accessible by scattering in different directions are located on a sphere described by the arrowhead of the scattering vector \mathbf{K} . Detecting light scattered in all possible directions

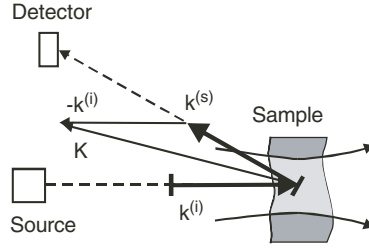


Figure 3. Backscattering geometry. Vectors of the incident and scattered waves, $\mathbf{k}^{(i)}$ and $\mathbf{k}^{(s)}$, respectively, and scattering vector \mathbf{K} .

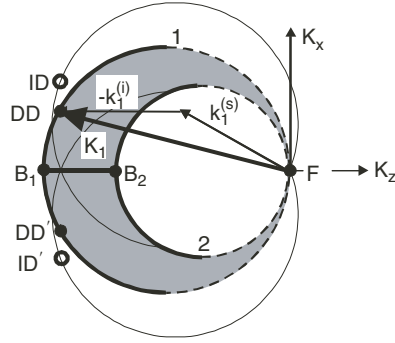


Figure 4. Ewald spheres in Fourier space for wavelengths λ_1 and λ_2 . Forward scattering: dashed semicircles; backward scattering: continuous semicircles. F, $B_{1,2}$, Fourier data obtained by forward and backward scattering. DD and DD', Fourier components obtained by detector position diversity, and ID and ID', Fourier components obtained by illumination direction diversity; both at λ_1 .

lets the arrowhead of \mathbf{K} describe the well-known Ewald sphere in \mathbf{K} -space with its centre at $(-k_x^{(i)}, -k_y^{(i)}, -k_z^{(i)})$, as shown in figure 4.

Using a single wavelength λ_1 yields only one single Fourier component at each scattering direction. For example, forward scattering in the direction of a narrow incident beam at (x, y) yields the projection of the scattering potential at (x, y) in the forward direction $\hat{F}_S(x, y; w = 0) = \int_{\text{Vol}(z)} F_S(x, y, z) dz$ (F in figure 4). In contrast, scattering in the opposite direction of the incident beam yields a solitary high frequency component of the scattering potential (B_1 in figure 4). Such a solitary Fourier component of the scattering potential, however, does not yield any resolution.

We shall now concentrate on backscattering. If one varies the position of the photodetector additional Fourier components (DD and DD' in figure 4) can be detected. Similarly, if the illumination direction is changed Fourier components ID and ID' become accessible. As can be seen from figure 4 these diversities give access mainly to a variety of transversal Fourier components. Using additional wavelengths, e.g. λ_2 , gives access to additional depth components (e.g. B_2). Whereas illumination and detection direction diversity techniques are used in OCT speckle reduction (section 2.5), wavelength diversity is used in LCI. In LCI light scattered back in the opposite direction of the illuminating beam is used for depth localization of light re-emitting sites. Then,

$$\mathbf{K}_j = -2\mathbf{k}_j^{(i)}, \quad (2.10)$$

with $|\mathbf{K}_j| = (4\pi/\lambda_j)$.

Let us now restrict the discussion to LCI. In this case the sample is illuminated by a narrow beam and light backscattered against the illuminating beam is detected. We assume that the scattering potential F_S within the illuminated sample volume does not depend on lateral coordinates. Then, the integrations over x' and y' in equation (2.7) can be replaced by a constant factor and the backscattered light wave at z is

$$V_S(z, K, t) = A_S(K) \exp(-ikz - i\omega t), \quad (2.11)$$

with $K = 2k$. Setting d constant the wavelength-dependent complex field amplitude $A_S(K)$ is proportional to the one-dimensional (inverse) FT of the scattering potential:

$$A_S(K) = a_S(K) e^{i\Phi_S(K)} \propto \text{FT}^{-1} \{F_S(z)\}. \quad (2.12)$$

Inverting that relation yields

$$F_S(z) \propto \text{FT} \{a_S(K) e^{i\Phi_S(K)}\}. \quad (2.13)$$

This is the physical basis of Fourier-domain LCI and OCT. Amplitude $a_S(K)$ and phase $\Phi_S(K)$ represent the complex LCI signal measured by interferometric techniques as detailed in section 4. Whereas the Fourier-domain OCT technique is directly based on the Fourier relation presented by equation (2.13), the time domain technique is based on a convolution operation of the sample response with the source coherence function (see equation (4.4)).

Figure 4 also demonstrates, that LCI and OCT are band-pass techniques. LCI and OCT detect high frequency Fourier components of the scattering potential, which, by the Fourier derivative theorem, are functions of derivatives of the scattering potential. Such considerations play an increasingly important role in tissue optics, where scattering properties give access to pathologic processes. Or, to put it another way, LCI and OCT are sensitive to discontinuities of the scattering potential (which can be caused by discontinuities of the refractive index as well as by discontinuities of the attenuation coefficient).

Another approach to grasp the significance of the LCI signal has been presented by Pan *et al* (1995). These authors developed a model, which can also explain what OCT detects in turbid tissue. From the observation that the irradiance at the detector is obtained by the superposition of the light fields reflected from within the scattering sample, they define a path-length-resolved field density and show, that the LCI signal encodes the square root of the path-length-resolved diffuse sample reflectivity (R).

Approaches which assume particular tissue models have been presented by Schmitt and Kumar (1996, 1998a) and Wang (2000). These authors assume tissue models with the refractive index variations caused by proper size distributions of small particles aggregated to fractal objects and use Mie theory to compute parameters like scattering coefficients and the anisotropy factor g (defined as the mean value of the cosine of the scattering angle).

2.2. Multiple scattered sample light

Multiple scattering can be described in terms of higher order Born approximations. The second-order Born approximation, e.g. includes light scattered twice. Part of the light of the right-hand side of equation (2.4) will be scattered a second time and generate a contribution (Born and Wolf 1999):

$$\int_{\text{Vol}(\mathbf{r}')} \int_{\text{Vol}(\mathbf{r}'')} V^{(i)}(\mathbf{r}', \mathbf{k}^{(i)}, t) \cdot F_S(\mathbf{r}', k) \cdot G_H(\mathbf{r}'', \mathbf{r}') \cdot d^3\mathbf{r}' \cdot F_S(\mathbf{r}'', k) \cdot G_H(\mathbf{r}, \mathbf{r}'') \cdot d^3\mathbf{r}''. \quad (2.14)$$

It would, however, be a formidable task to invert these six-dimensional integrals. Therefore, it seems that only single scattered light is useful to derive structural information about the underlying scattering potential. However, multiple scattering in samples is important, because

it gives access to parameters like absorption coefficients, scattering coefficients, scattering anisotropy, and concentration of particles in a solution. Furthermore, multiple scattered light decisively influences OCT probing depth and signal-to-noise ratio (SNR).

In the end equations (2.9) and (2.14) are based on Maxwell's equations. There are other treatments of scattering based on Maxwell's equations. For example, Brodsky *et al* (2000) use a path-integral analysis of the vector Helmholtz equation. A reasonable agreement has been obtained with experiments on the maximum LCI signal as a function of particle size and concentration by Thurber *et al* (2000). Furthermore, the properties of multiple scattered light have been analysed analytically using the extended Huygens–Fresnel formulation of beam propagation in the turbulent atmosphere developed by Yura (1979) and adapted to the OCT problem by Schmitt and Knüttel (1997) and by Thrane *et al* (2000). These studies have revealed that LCI and OCT probing depths are not only dependent on absorption and scattering coefficients but also on scattering anisotropy, aperture of the sample lens, and, in particular, on the sample distribution between lens and coherence gate.

Alternative treatments of multiple scattering are based on transport theory. In most tissues, for example, light diffusion dominates within a few millimetres of penetration depth. Analytic techniques will then become hopelessly elaborate. A heuristic approach based on transport theory might be used and diffusion equation based techniques like photon density waves (O'Leary *et al* 1992) become useful. These techniques are of outstanding importance in DOT.

2.3. Probing depth

Since multiple scattered light does not contribute to the object's Fourier spectrum it forms a disturbing background. Its effects are a reduction of imaging contrast, a reduction of resolution, and a reduction of penetration depth. An important question, therefore, is the balance between single and multiple scattered light. Considerable work has already been done in order to estimate the share of multiple scattered light.

Usually, the probing beam is focused at the sample as indicated in figure 5, and the coherence matching point is located at or near the focal point of the sample lens. Single scattered light detected by the photodetector will be limited to photons scattered at the coherent probe volume. The coherent probe volume (we use this term to avoid confusion with the term 'coherence volume') equals the depth of the coherence gate multiplied by the corresponding beam cross section (see figure 5).

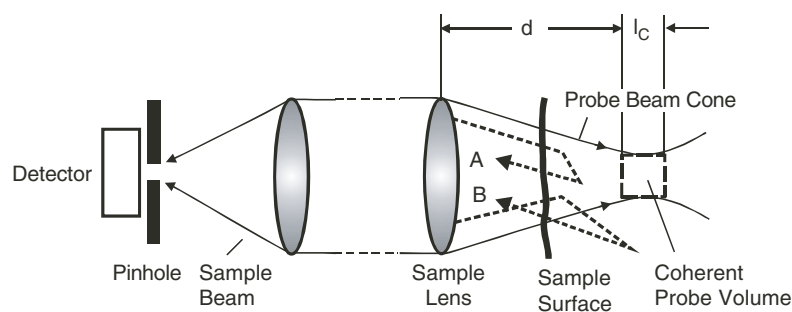


Figure 5. Geometry of sample and probing beam. Trajectories of double scattered photons *not* contributing to the interferogram: trajectory A is outside the coherence gate; the photon moving along trajectory B is within the coherence gate but will miss the fibre or pinhole in front of the photodetector.

Now consider double scattered photons. The first scattering event of double scattered photons must, of course, be located within the illuminating probe beam cone. Because of the coherence condition the second scattering event must be located within or very close to the coherent volume. Hence, it is the path length of single and double scattered photons that determines the probing depth.

With increase in probing depths the number of photons multiple scattered and detected by the photodetector increases. These photons can have their trajectories even outside of the probing beam. Increasing the numbers of scattering events will reduce time-coherence as well as space-coherence of these (near-ballistic) photons. Finally, at large probing depths incoherent diffuse photons will dominate.

The transition from the single scattering regime to diffuse scattering has experimentally been analysed by low-coherence dynamic light scattering (Bizheva *et al* 1998). Experimental studies based on this technique have shown, that the transition from single scattered light to the diffusing light regime occurs at longer path lengths for either lower scattering anisotropy g (figure 6) or a smaller NA of the sample lens (Bizheva *et al* 1998 and Wax *et al* 2001). Therefore, the detected photons have a longer mean free path in the sample than that given by the mean scattering free path $1/\mu_s$, depending on factors such as the NA of the sample lens and the scattering anisotropy g of the sample. It has been shown by Gandjbakhche *et al* (1992), that in the case of anisotropic random walks the probability of a photon to experience n scattering events and then to return to the surface scales as $n(1 - g)/(1 + g)$. Hence, with increasing scattering anisotropy g , the relative number of detected photons with a large number n of scattering events decreases.

Since the linewidth of light that has scattered n times equals n times the width for single scattering (Wax *et al* 2001) the twofold linewidth is a reasonable criterion for LCI and OCT probing depth. That is, we define probing depth as the depth at which double scattered photons begin to dominate. Figure 6 shows the corresponding number of mean free walks as a function of g .

As can be seen from figure 6, LCI and OCT probing depths are in the range of several free random walks. A similar dependence is observed when different NAs of the sample lens are used (Bizheva *et al* 1998). Increasing the NA causes detection of photons with a higher number

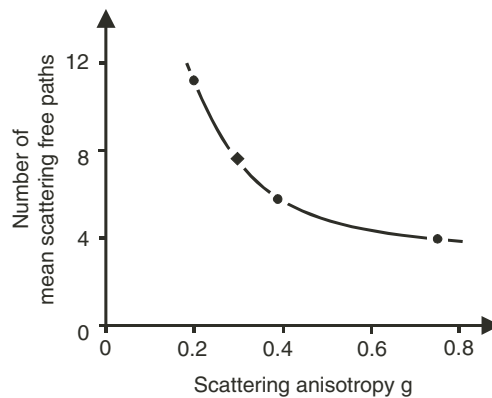


Figure 6. Number of mean scattering free paths ($1/\mu_s$) of detected photons to obtain twofold linewidth in light backscattered from solutions of polystyrene microspheres in water, as a function of scattering anisotropy g . ● particle diameters (from left) 0.22, 0.3 and 0.55 μm ; mean free path $\sim 100 \mu\text{m}$; SLD $\lambda = 850 \text{ nm}$; NA = 0.32; (Bizheva *et al* 1998) ◆ particle diameter 0.258 μm ; mean free path 156 μm ; SLD $\lambda = 845 \text{ nm}$; NA not known (Wax *et al* 2001).

of scattering events. This dependence, however, is not as pronounced as the dependence on the optical anisotropy. In a medium with high optical anisotropy, for example, the aperture cannot efficiently reject multiple scattered light.

Penetration depth is a rather critical parameter in many applications of OCT, in particular, in the biomedical field. Since the main process limiting penetration depth of OCT is scattering there have been attempts to match the refractive indices of tissue components. For example, a 50% increase in transmittance of skin has been achieved by the introduction of anhydrous glycerol (Vargas *et al* 1999). Tuchin *et al* (2002) discuss index matching to enhance the optical penetration depth of whole blood.

Since in the visible spectrum, scattering and absorption in tissue decrease nearly monotonically with increasing wavelength, the red end and the adjacent near-infrared (NIR) wavelength ranges are preferred in OCT (see also section 3.2). At these wavelengths biological tissue has scattering anisotropies of about $g \approx 0.9$ (Schmitt and Kumar 1998a). Hence, forward scattering dominates, and the penetration depth of OCT can roughly be estimated from figure 6 as of the order of three to four mean free random walks $1/\mu_s$.

It must be emphasized, however, that the LCI probing depth not only depends on the thickness but also on the distribution of a scattering medium between probing lens and probing plane. A multiple scattering layer of given thickness, e.g. reduces the probing depth much more, if located close to the sample lens, but reduces the probing depth much less, if located close to the sample. This so-called shower curtain effect (Dror *et al* 1998) has already been known in atmospheric optics and was adapted to OCT by Thrane *et al* (2000).

2.4. Sensitivity

The main parameters of an OCT instrument are its optical power and wavelength, its penetration, resolution and sensitivity, and its image acquisition rate. Whereas these parameters are interdependent, some might be determined by the imaging problem. For example, the choice of the wavelength will be highly dependent on the nature of the sample.

An important feature of an OCT system is the weakest sample reflectivity $R_{S,\min}$ yielding a signal power equal to the noise of the system. Sensitivity S can be defined as the ratio of the signal power generated by a perfectly reflecting mirror ($R = 1$) and that generated by $R_{S,\min}$. Since these signal powers are proportional to the corresponding reflectivities we have:

$$S = \frac{1}{R_{S,\min}} \Big|_{\text{SNR}=1}. \quad (2.15)$$

The effective signal photocurrent at the detector is generated by the interference term, equation (1.11):

$$i_G = \frac{\eta q_e}{h\nu} \sqrt{2P_S P_R}, \quad (2.16)$$

where P_S and P_R are the powers of the sample and reference beams incident on the photodetector.

Standard OCT devices use ac detection. Since in the low frequency range, most amplifiers exhibit flicker noise ($1/f$ noise; with typically 3 dB per octave slope), frequencies above approximately 10 kHz are used. The dominating noise sources then are shot noise $\langle \Delta i_{\text{sh}}^2 \rangle$, excess intensity noise $\langle \Delta i_{\text{ex}}^2 \rangle$, and receiver noise $\langle \Delta i_{\text{re}}^2 \rangle$. Receiver noise can either be calculated from manufacturer's specifications or can be modelled as thermal noise. In the case of broad-bandwidth light the photocurrent noise has two terms: shot noise due to photocurrent variance and excess noise due to self-beating of broad-band light waves (Hodara 1965). The resulting

mean square photocurrent noise is (Podoleanu and Jackson 1999, Rollins and Izatt 1999):

$$\langle \Delta i_p^2 \rangle = \langle \Delta i_{sh}^2 \rangle + \langle \Delta i_{ex}^2 \rangle = 2q_e B \langle i \rangle + (1 + \Pi^2) \langle i \rangle^2 \frac{B}{\Delta \nu_{eff}}, \quad (2.17)$$

where B is the electrical bandwidth, Π the degree of source polarization, $\langle i \rangle$ the mean detector photocurrent and $\Delta \nu_{eff}$ the effective optical line width of the source (Morkel *et al* 1990). For Gaussian spectra this is given by

$$\Delta \nu_{eff} = 1.5 \Delta \nu \quad (2.18)$$

with full width $\Delta \nu$ at half maximum of the power spectrum. The SNR is the ratio of the mean signal power and the noise power:

$$SNR = \frac{2\alpha^2 P_S P_R}{\langle i_{sh}^2 \rangle + \langle i_{ex}^2 \rangle + \langle i_{re}^2 \rangle}, \quad (2.19)$$

with $\alpha = (q_e \eta / h \bar{\nu})$. In a Michelson interferometer with an ideal and symmetric beam splitter we have $P_R = P_{Source} R_R / 4$ and $P_S = P_{Source} R_S / 4$, where P_{Source} is the output power of the light source, R_R the reflectivity of the reference mirror, and R_S the reflectivity of the sample. We model the receiver noise as thermal noise of a resistance limited receiver: $\langle \Delta i_{re}^2 \rangle = 4k_B T B / \rho_L$, where k_B is Boltzmann's constant, T the absolute temperature and ρ_L the load resistor (amplifier noise can be incorporated too into the thermal noise current by replacing ρ_L by an effective load resistor). We furthermore assume the photocurrent dc component $\langle i \rangle$ to be determined only by the reference beam. Thus, we have

$$S = \frac{\alpha^2}{8B} \frac{P_{Source}^2 R_R}{(\alpha/4) P_{Source} R_R [2q_e + (\alpha/4) P_{Source} R_R (1 + \Pi^2) / (\Delta \nu_{eff})] + (4k_B T / \rho_L)}. \quad (2.20)$$

The two addenda in the denominator define two limiting regimes, one where receiver noise dominates and another one, where the light source power is very high. In the intermediate regime, shot noise dominates and the sensitivity is

$$S = \frac{\alpha}{4} \frac{P_{Source}}{q_e} \frac{1}{B}. \quad (2.21)$$

Equation (2.21) expresses the rule of thumb that sensitivity is proportional to the source power and inversely proportional to the electronics bandwidth.

Within the shot noise dominated range, S depends linearly on source power. This regime is usually realized in OCT systems and can be regarded as optimum, since, at lower power, receiver noise would limit sensitivity, and at higher power no additional sensitivity can be gained because of excess noise. In the shot noise limited regime, sensitivities of $S = 10^{11}$ and higher have been reported. Figure 7 illustrates the sensitivity of an OCT system as a function of reference reflectivity for different wavelength bandwidths. A similar plot, employing parameters for OCT of scattering tissues can be found in Rollins and Izatt (1999). Unbalanced versus balanced operation in OCT has been analysed by Podoleanu (2000), who showed that the balanced OCT configuration, besides the attenuation of vibration-induced noise in the depth-scanner and the avoidance of back-reflections to the optical source, has signal-to-noise advantages in particular for fast OCT systems.

2.5. Speckle

2.5.1. Speckle properties. Speckle is generated by interference of waves with random phases. Besides its role as noise in coherent imaging, speckle has become a very useful phenomenon for a series of measurement techniques (Sirohi 1993). For its role in medicine see Briers (2001). In LCI and OCT, 'subjective' speckle (Gabor 1970) arises in the sample beam. The

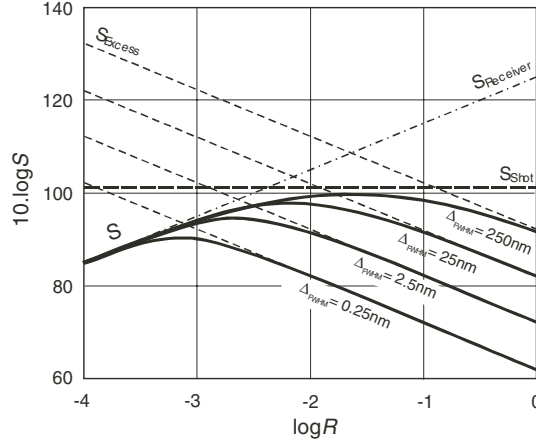


Figure 7. Sensitivity S of an OCT system (—) as a function of the logarithm of reference mirror reflectivity R according to equation (2.20) for Gaussian spectra with spectral widths of: $\Delta\lambda_{\text{FWHM}} = 0.25, 2.5, 25$ and 250 nm. $P_{\text{Source}} = 1.5$ mW; mean wavelength $\bar{\lambda} = 830$ nm; $\eta = 0.8$; $\Pi = 1$; receiver noise current = 0.5 pA/ $\sqrt{\text{Hz}}$; $B = 100$ kHz. The corresponding sensitivities due to single noise sources (shot noise S_{Shot} , excess noise S_{Excess} and receiver noise S_{Receiver}) are shown too.

sample wave is the sum of many wavelets arising at backscattering sites within the coherent volume. These wavelets have random phases due to the random depth distribution of scattering sites in the sample and due to fluctuating refractive index in the sample.

First-order statistical properties of speckle can readily be quoted if amplitudes and phases of the individually scattered contributions are statistically independent, and identically distributed, have phases uniformly distributed over $(-\pi, \pi)$, and have waves that are perfectly polarized. Then we have ‘fully developed’ speckle (George *et al* 1976) and the resultant phasor of the sample wave is a circular complex Gaussian random variable. The corresponding statistics of the sample intensity is negative exponential and the probability density function is (Goodman 1965, 1976)

$$p_{I_S}(I_S) = \begin{cases} \frac{1}{\langle I_S \rangle} \exp\left(-\frac{I_S}{\langle I_S \rangle}\right), & \text{if } I_S \geq 0, \\ 0, & \text{otherwise,} \end{cases} \quad (2.22)$$

with moments

$$\langle I^n \rangle = n! \langle I \rangle^n. \quad (2.23)$$

The contrast of a speckle pattern is defined as

$$C = \frac{\sigma_{I_S}}{\langle I_S \rangle} \quad (2.24)$$

leading to the well known high speckle contrast $C = 1$ of fully developed polarized speckle; σ_{I_S} is the standard deviation of I_S .

Second-order statistics of speckle is concerned with their temporal or spatial structure. A standard means to describe such properties are correlation functions. The characteristic depth extension of speckle in the LCI signal, e.g. can be estimated as correlation length of its intensity fluctuations. We assume statistically independent backscattered wavelets. In this case the intensity correlations can be obtained from the amplitude correlation $G(\tau)$ by (Loudon 1985)

$$\langle I(t)I(t+\tau) \rangle = \langle I(t) \rangle^2 [1 + |G(\tau)|^2]. \quad (2.25)$$

Since the spectrum of light scattered back from the sample has approximately the same spectrum as the probe beam, the correlation length of its intensity fluctuations can be estimated by the corresponding coherence length l_C . In fact the real situation in OCT can be more complex: first, because of the reference beam we do not have fully developed speckle in LCI and OCT. Second, light backscattered at specularly reflecting interfaces does not generate speckle. Third, due to absorption, backscattered light can have a modified spectrum.

2.5.2. Interferogram speckle. The field at the photodetector of a LCI system is the sum of backscattered sample wavelets plus a reference wave (of intensity I_R). Ideally, standard LCI and OCT do not use the total intensity $I = I_S + I_R + G_{SR}$ at the photodetector, but the interferogram G_{SR} . The constant reference beam intensity I_R and the fluctuating sample intensity I_S are removed by heterodyne or related techniques (section 4.1.4). In the heterodyne technique, for example, the interferogram intensity G_{SR} is modulated by the carrier frequency $f_C = 2V_{\text{Mirror}}/\bar{\lambda}$ ($\bar{\lambda}$ is the mean wavelength, V_{Mirror} the speed of the reference mirror), whereas the mean frequency caused by speckle is $f_{\text{Speckle}} = 2V_{\text{Mirror}}/l_C$. Hence, if $l_C \gg \bar{\lambda}$ as in standard OCT, the heterodyne technique can efficiently suppress speckle fluctuations caused by the fluctuating sample intensity I_S , but, of course, not the speckle fluctuations carried by the interferogram. In high-resolution OCT, however, with $l_C \sim \bar{\lambda}$ electronic band-pass filtering must be performed very carefully to eliminate speckle noise contributed by the fluctuating sample intensity I_S . In any case, the speckle noise of the interferogram remains.

Let us assume fully developed sample beam speckle (polarized light). The statistics of the depth-scan signal is determined by the sample wave. The OCT depth-scan signal only contains the interferogram; its statistics is that of the interferogram. The interferogram is twice the real part of the cross-correlation of the analytic signals of sample and reference beam (see equation (1.9)), $G_{SR}(\Delta t) = 2\text{Re}\{\Gamma_{SR}(\Delta t)\} = 2A_S R |\gamma_{SR}(\Delta t)| \cos[\alpha_{SR} - \delta_{SR}(\Delta t)]$. R is the amplitude of the reference beam; the amplitude of the sample beam A_S and its phase α_{SR} with respect to the reference beam are random. Hence, G_{SR} is Gaussian. Standard OCT techniques, however, use the maximum of the real envelope A_Γ (see equation (1.13)) of the interferogram as picture function G of the OCT image. Therefore, G is Rayleigh-distributed (Pircher *et al* 2002):

$$p_G(G) = \frac{2G}{\langle G^2 \rangle} e^{-(G^2/\langle G^2 \rangle)}, \quad \text{if } G \geq 0, \quad (2.26)$$

$$= 0, \quad \text{otherwise,}$$

with mean $\langle G \rangle = 2\langle A_S \rangle R |\gamma_{SR}(0)|$ and second moment $\langle G^2 \rangle = (4/\pi)\langle G \rangle^2$. Hence, the contrast of the OCT signal in the case of fully developed sample beam speckle is $C_G = \sqrt{\langle G^2 \rangle - \langle G \rangle^2} / \langle G \rangle = \sqrt{(4/\pi) - 1} = 0.52$. These fluctuations are caused by the distribution of the scatterers within the coherent probe volume. The corresponding intensity fluctuations of the sample signal occur on a scale of the coherence length and will degrade depth resolution. Note, that contrast of speckle in OCT signals is only about half of the contrast of speckle in standard coherent imaging (Gabor 1970). Furthermore, most OCT images display the logarithm of G . Therefore, the impact of speckle in OCT is much less dramatic if compared with coherent imaging.

2.5.3. Suppression of speckle in OCT. Adding up M uncorrelated fully developed speckle patterns yields a compound speckle pattern with a gamma-distributed probability density and speckle contrast $C = M^{-1/2}$ (Goodman 1965, 1976). Therefore, the corresponding gain in the SNR is $M^{1/2}$. Three conditions, however, must be fulfilled: the summation must occur on an intensity basis; the single speckle patterns must be uncorrelated; and the single object structures

to be imaged must be identical. Goodman (1984) has already discussed techniques to achieve uncorrelated optical speckle, like time, space, frequency or polarization diversity. Further possibilities are depth-scan signal processing (Forsberg *et al* 1991) and image post-processing (Schmitt 1997).

A space-diversity technique has been described by Schmitt (1997). In this technique the compound signal is obtained from a number of single sample signals generated by speckle filling the aperture of the LCI sample lens. It should be noted, however, that in this case these signals are uncorrelated, and transverse resolution has already been degraded below the diffraction limit of the sample lens. In fact, in that case the signals from additional detectors can be used to reduce speckle noise in the depth-scan signal. Nevertheless, the situation is more involved since transversal resolution also depends on the transverse sampling rate. Anyway, using this technique a signal-to-noise gain close to the theoretical attainable factor (two; using four detectors) has been obtained without a significant loss in resolution.

Bashkansky and Reintjes (2000) describe a practical speckle-reduction technique for *en-face* OCT imaging using illumination direction diversity. Xiang *et al* (1998) describe the use of a wavelet filter with nonlinear thresholds for speckle reduction. Another filter technique has been described by Rogowska and Brezinski (2000). These authors use an adaptive speckle suppression filter to enhance image features while suppressing the noisy background. Further experimental speckle-reduction methods are discussed by Schmitt *et al* (1999). The zero-adjustment procedure (Yung *et al* 1999) reduces speckle contrast in regions with high scatterer densities but tends also to blur sharp boundaries between image features. Pircher *et al* (2002) have demonstrated speckle reduction by frequency compounding using two light sources with non-overlapping spectra.

2.6. Resolution

Usually, spatial resolution performance of an imaging system is evaluated by means of the modulation transfer function (MTF). The MTF is the magnitude of the optical transfer function which on its part is the inverse FT of the point spread function (PSF) of the system. Each component of an imaging system has its own MTF. The MTF alone, however, is not sufficient to determine the spatial performance of an OCT system because the electronic system adds noise:

- (a) noise depends on parameters like source power, interferometer parameters, electronics parameters and sample reflectivity, and,
- (b) noise tends to ‘wash out’ higher frequency signals.

To estimate the low light level OCT performance, for example, the SNR versus the frequency curve would be a better predictor of system performance. In this section, however, we shall only consider the PSF of OCT and some signal processing techniques for OCT image enhancement.

2.6.1. OCT PSF and resolution. The OCT resolution is split: depth resolution is defined by the coherence length (equation (1.1)), whereas transverse resolution depends on the minimum waist radius w_F of the focused (Gaussian) probe beam. Within the frame of the ABCD rule—which neglects diffraction at the lens aperture—we obtain (Gerrard and Burch 1975)

$$w_F = \frac{w_P f}{\sqrt{z_1^2 + \pi^2 w_P^4 / \lambda^2}}, \quad (2.27)$$

where w_P is the minimum beam waist radius of the probe beam before focusing, f the focal length of the sample lens and z_1 the distance of the focal plane of the sample lens from the beam waist of the unfocused probe beam. This equation shows that there are two possibilities

to minimize the probe beam waist diameter: either a decrease of the focal length f of the sample lens or an increase of the distance z_1 of the beam waist of the impinging probe beam from the sample lens. In any case, the spot radius of the focused beam is

$$w(\Delta z) = w_F \sqrt{1 + \left(\frac{\bar{\lambda} \Delta z}{\pi w_F^2} \right)^2}, \quad (2.28)$$

where Δz is the distance from the minimum beam waist of the focused beam.

A proper definition of an OCT PSF has been provided by Schmitt (1998a). He defined the PSF as the functional dependence of the OCT signal of a point scatterer scanning throughout the focal space of the sample lens. This function is an amplitude modulated cosine with a mean period of $\bar{\lambda}/2$. If the optical path matchpoint lies at the beam waist of the focused Gaussian probe beam and multiple scattering can be neglected, the envelope of that PSF is

$$\Pi(\Delta r, \Delta z) = e^{-(\Delta z/l_c)^2 4 \ln 2} e^{-(\Delta r/w(\Delta z))^2}, \quad (2.29)$$

where Δz is the displacement of the scatterer from the beam neck in the axial direction and Δr the displacement in the radial direction. (Note that the minimum beam waist of a Gaussian beam generally does not need to coincide with the focal point of the sample lens.)

Since the scattering potential $F_S(z)$ and the complex amplitude $A_S(K)$ of the scattered wave are, besides a constant factor, FT pairs in direct and K -space (see equation (2.12)), the Fourier uncertainty relation yields the depth resolution. For a Gaussian amplitude spectrum $A_S(K) \propto e^{-4 \ln 2 (K/\Delta K_{\text{FWHM}})^2}$ we obtain as product of its full-width at half-maximum (FWHM) in K -space ΔK_{FWHM} and the FWHM of the amplitude in z -space $\Delta K_{\text{FWHM}} \Delta z_{\text{FWHM}} = 8 \ln 2$, or

$$\Delta z_{\text{FWHM}} = \frac{8 \ln 2}{\Delta K_{\text{FWHM}}}. \quad (2.30)$$

This can easily be extended to the wavelength-dependent amplitude spectrum and we obtain as OCT depth resolution:

$$\Delta z_{\text{FWHM}} = \frac{2 \ln 2}{\pi} \frac{\bar{\lambda}^2}{\Delta \lambda_{\text{FWHM}}}, \quad (2.31)$$

where $\bar{\lambda}$ is the mean wavelength. The above uncertainty relations are related to amplitudes and can directly be applied to Fourier-domain OCT (section 4.2). Note, that the time-domain OCT signal too is proportional to the sample beam amplitude (equation (1.9)). In time-domain OCT, the depth resolution equals half the coherence length and the same relation is obtained (see equation (4.9)).

Transversal resolution in OCT is limited either by an insufficient transversal sampling rate or/and the size of the probe beam diameter. We define transversal resolution in analogy to depth resolution as the FWHM diameter Δd_{FWHM} of the probe beam amplitude distribution at the beam waist of the focused probe beam:

$$\Delta d_{\text{FWHM}} = 2\sqrt{\ln 2} w_0 = 2\sqrt{\ln 2} \frac{\bar{\lambda}}{\pi \theta_S}, \quad (2.32)$$

θ_S is the angular spread of the Gaussian beam, $\sin \theta_S$ is the NA of the beam.

A specific problem in OCM and high-resolution OCT is the depth dependence of transversal resolution. Twice the confocal beam parameter of a Gaussian beam can be used to define the depth of focus, DOF:

$$\text{DOF} = 2 \frac{\bar{\lambda}}{\pi \theta^2}. \quad (2.33)$$

For example, a transversal resolution of $\delta r = 20 \mu\text{m}$ at a mean wavelength of $\bar{\lambda} = 830 \text{ nm}$ leads to a depth of focus of $\text{DOF} = 3 \text{ mm}$, whereas a transversal resolution of $\delta r = 2 \mu\text{m}$

reduces the depth of focus to $\text{DOF} = 30 \mu\text{m}$. Since a small beam waist radius is associated with a large NA, a small confocal beam parameter results and vice versa. Hence, a compromise has to be found between a desired transversal resolution and the available depth of focus. A way out of that dilemma is the use of a dynamic focus tracking system. Schmitt *et al* (1997) have described such a system which is now in widespread use in experimental work; Lexer *et al* (1999) have described a system which is capable of high scanning speeds. Alternatively, an image fusion technique has been used by Drexler *et al* (1999), in which separate images with different focal depths were recorded and the corresponding tomograms fused together, similar to C-mode scanning used in ultrasound imaging.

2.6.2. Deconvolution. Depth resolution is primarily degraded by the finite width of the depth PSF envelope. Since the complex depth PSF is the inverse FT of the power spectrum $S_{\text{Source}}(\nu)$ of the source light (equation (4.6)), the latter should be a narrow and smooth function. Any ripple of the spectral structure will lead to spurious image structures. As the OCT signal is a convolution of the sample response with the coherence function of the source light (see equation (4.4)), deconvolution seems the natural technique to compensate for the signal distortions caused by the depth PSF. In Fourier space deconvolution is simply performed by calculating the transfer function:

$$H(\nu) = \frac{W_{\text{SR}}(\nu)}{S_{\text{Source}}(\nu) + \varepsilon}, \quad (2.34)$$

where $W_{\text{SR}}(\nu)$ is the cross-spectral density of the sample and reference beams. $S_{\text{Source}}(\nu)$ must be known and must not contain zeros. Therefore, most deconvolution techniques add a non-zero term— ε in equation (2.34)—to the denominator. It must be noted, however, that deconvolution can be ruined in particular by structured noise.

Several studies, performed for example by Kulkarni *et al* (1997), Bashkansky *et al* (1998b) and Wang (1999), have demonstrated improvements in depth resolution by a factor of 2–3, but had problems with noise.

2.6.3. Dispersion compensation. Dispersion, too, deteriorates depth resolution. Usually dispersive material is deployed in the reference arm of the interferometer to balance the dispersion of the sample arm. The disadvantage of that technique is that changing dispersion balancing requirements dictates the need to move the mechanical components and, therefore, it is slow.

A dispersive medium of path length z adds a frequency-dependent phase to the sample wave (Van Engen *et al* 1998):

$$\Phi_{\text{Disp}}(\omega) = k(\bar{\omega})z + k^{(1)}(\bar{\omega})(\omega - \bar{\omega})z + k^{(2)}(\bar{\omega})\frac{(\omega - \bar{\omega})^2}{2}z + \dots, \quad (2.35)$$

where $k^{(j)}(\bar{\omega}) = (d^j k / d\omega^j)_{\omega=\bar{\omega}}$ is the j th order dispersion. From the Fourier shift theorem, it follows that a multiplication of a function by a phase factor in Fourier space shifts the FT of that function in direct space:

$$\Gamma(\tau + \Delta t) = \text{FT}^{-1}\{S(\omega)e^{-i\omega\Delta t}\}. \quad (2.36)$$

An unmodified shift of the coherence function will only occur if the additional phase in Fourier space is directly proportional to frequency: $\Phi(\omega) = \omega\Delta t$. Therefore, only zero-order dispersion shifts the coherence function without modification. First-order dispersion changes the coherence length to

$$l_{\text{C,Disp}} = \frac{l_{\text{C}}}{n_{\text{G}}}. \quad (2.37)$$

Since the group index n_G is always larger than unity, first-order dispersion improves depth resolution. Second- and higher order dispersion will distort the Fourier spectrum and thus increase the coherence length and degrade OCT depth resolution (Hitzenberger *et al* 1998, 1999a).

A numerical *a posteriori* dispersion compensation technique has been presented by Fercher *et al* (2001). A digital correlation technique is used to compensate for dispersion induced resolution loss. The interference term is numerically correlated with a depth-variant kernel. The advantages of the correlation technique are that this technique is not sensitive to zeros in the response function and that correlation of the experimental signal with a mathematically defined function reduces noise. De Boer *et al* (2001) have numerically corrected the quadratic phase shift in the Fourier domain. They eliminated the broadening effect of group-velocity dispersion on the coherence function by introducing a quadratic phase shift in the Fourier domain of the interference signal. A similar technique has been used by Brinkmeyer and Ulrich (1990) when testing integrated-optical waveguides.

2.6.4. Limited diffraction beams. As mentioned above, focus tracking can be used to maintain a desired transversal resolution along the depth-scan. Another technique is to use adaptive optics, as already proposed for focusing of astronomical optics (Arutyunov and Slobodyan 1985). Lu *et al* (2002) have used Durnin's diffraction-free radiation modes (Durnin *et al* 1987) to increase depth of field and to reduce sidelobes in OCT. Using Bessel beams instead of focused Gaussian beams has been shown to have the potential to increase the depth of focus and maintain reasonable transverse resolution. To reduce the sidelobes, three backscattered diffraction limited Bessel beam signals were recorded with different masks at the sample illuminating system. Results show a lateral resolution of about $4.4\bar{\lambda}$ ($\bar{\lambda} \approx 940$, $\Delta\lambda \approx 70$ nm) and lower than -60 dB sidelobes over an entire depth of field of 4.5 mm. Similar results (10 μ m lateral resolution over a focus depth of 6 mm) have been obtained by Ding *et al* (2002) using an axicon lens to focus the probing beam.

3. OCT light sources

We present some important points concerning parameters of light sources used in OCT. Of course, a major point of view is the power of the source as can be seen from equation (2.20). However, higher power increases excess noise and no additional sensitivity might be gained. Also, many samples, e.g. in ophthalmology, do not tolerate large probe beam powers. A proper selection of the wavelength can reduce scattering and increase probing depth. Furthermore, the shape of the spectrum determines the structure of the depth PSF. A careful selection of the light source, therefore, is important.

3.1. Coherence properties

Temporal coherence determines depth resolution, whereas spatial coherence plays a role in both lateral resolution and depth resolution of LCI and OCT. The techniques dominating since the early development of LCI and OCT rely on single-transverse-mode light. If multiple-transverse-mode light sources with reduced space-coherence are used in these standard LCI and OCT techniques, reduced interferential contrast and, therefore, degraded signal quality results. Hence, techniques have been developed to measure the coherence properties of light sources (Hitzenberger *et al* 1999b).

It was only during the last few years that OCT techniques have been developed using transverse multimode radiation and the potential advantages of that radiation have been

recognized. For example, in parallel OCT reduced space-coherence can reduce coherent cross-talk between OCT channels and thus reduce speckle (Beaurepaire *et al* 1998). Interference microscopy techniques enable the use of thermal light sources in LCI and OCT (Dubois *et al* 1999, Fercher *et al* 2000, De Martino *et al* 2001). In the Linnik interference microscope, for example, the plane of observation at the interferometer exit is conjugate to the sample plane under study. Each point in that plane has an image in the space in front of the interferometer, which might be called the source (and in fact can be the source surface but also any plane in the illuminating system as well). The source is imaged by both the reference beam and the sample beam onto the photodetector at the observation plane. If these two images are congruent space-coherence is warranted even in the case of light sources termed traditionally as ‘incoherent’.

The properties of a laser beam depend on parameters like fluorescence wavelength of the laser medium (wavelength), gain bandwidth and resonator characteristics (coherence properties) as well as mode volume in the laser cavity, population density of laser-active atoms and pump power (beam power). Hence, there is a wide variety of parameter combinations and of lasers qualified for medical applications (Vij and Mahesh 2002). Nevertheless, the class of lasers which can be used in LCI and OCT is, due to their exceptional coherence requirements, rather restricted.

At present, the most popular light source in OCT is the SLD. SLDs operate like edge-emitting laser diodes (EELD); the structure of an SLD too is very similar to that of an EELD. It does not, however, have optical feedback or a cavity. Superluminescence occurs when the spontaneous emission of an EELD experiences gain due to higher injection currents. The higher gain causes a superlinear power increase and an increasing narrowing of the spectral width. The radiation emitted by an SLD is amplified spontaneous emission (ASE) and, therefore, of low time-coherence. Since SLDs are implemented in wave-guide structures, the space-coherence of the emitted radiation is generally high. The wavelength is determined by the material and its layering within the diode semiconductor.

To some extent, the properties of light emitted by thermal sources also depend on the spectral properties of the emitting material, but spectral intensity and time-coherence properties are dominated by Planck’s law. Thermal light sources ideally emit blackbody radiation with a spectral distribution given by Planck’s law for cavity radiation. The coherence-time of blackbody radiation can be estimated by (Fercher *et al* 2000): $\tau_c = (h/(2\pi))/k_B T$; h is Planck’s constant, k_B the Boltzmann’s constant and T the temperature of the source. For a tungsten halogen lamp with a distribution temperature of $T = 3240$ K the corresponding coherence length is $c\tau_c = 0.69 \mu\text{m}$. This extremely short coherence length of thermal light is of interest for OCT. To provide interference between the OCT reference beam, and the probe beam, space-coherence is important. It has been shown, that the coherently emitted light energy flux is $0.307L\bar{\lambda}^2$, where L is the radiance of the source. For example, if a tungsten halogen lamp is used in an interferometer, the maximal energy flux coherently emitted at $\lambda_{\text{max}} = 894 \mu\text{m}$ has been shown to be approximately $0.22 \mu\text{W}$ (Fercher *et al* 2000).

Table 1 gives an overview of some light sources recently used in LCI and OCT.

3.2. Wavelength

Penetration depth of OCT is determined by emission wavelength and source power. Let us consider the wavelength-dependence of absorption of biomedical materials. For soft tissues and optical radiation in the 600–1300 nm range, absorption coefficients are of the order of $\mu_a \sim 0.1\text{--}1 \text{ mm}^{-1}$, and scattering coefficients are of the order of $\mu_s \sim 10\text{--}100 \text{ mm}^{-1}$ (Wilson and Jacques 1990). Absorption of most tissue chromophores tends to decrease with increasing wavelength. Biological tissue, however, is not a homogeneous material. It is constituted of cells

Table 1. Examples of low time-coherence light sources used in OCT.

Light source	$\bar{\lambda}$	$\Delta\lambda$ (nm)	l_C (μm)	Coherent power	Reference
SLD	675 nm	10	20	40 mW	Superlum Diodes Ltd. (2002)
	820 nm	20	15	50 mW	
	820 nm	50	6	6 mW	
	930 nm	70	6	30 mW	
	1300 nm	35	21	10 mW	
	1550 nm	70	15	5 mW	
Kerr lens					
Ti : sapphire laser	0.81 μm	260	1.5	400 mW	Drexler <i>et al</i> (1999)
Cr : forsterite	1280 nm	120	6	100 mW	Bouma <i>et al</i> (1996)
LED	1240 nm	40	17	0.1 mW	Schmitt <i>et al</i> (1997)
	1300 nm				
ASE fibre sources	1300 nm	40	19	60 mW	NTT El. Corp. (2002)
	1550 nm	80	13	40 mW	
Superfluorescence					
Yb-doped fibre	1064 nm	30	17	40 mW	Bashkansky <i>et al</i> (1998a)
Er-doped fibre	1550 nm	80–100	16	100 mW	Bouma <i>et al</i> (1996)
Tm-doped	1800 nm	80	18	7 mW	Bouma <i>et al</i> (1998)
Photonic crystal fibre	1.3 μm	370	2.5	6 mW	Hartl <i>et al</i> (2001)
	725 nm	370	0.75		Povazay <i>et al</i> (2002)
Thermal tungsten halogen	880 nm	320	1.1	0.2 μW	Fercher <i>et al</i> (2000)
					Vabre <i>et al</i> (2002)

maintained in a lattice, the so-called extracellular matrix. This matrix is composed of bundles of structure proteins such as collagen and elastin, and is partially filled with hydrated gel. Therefore, the ratio of scattering to absorption (μ_s/μ_a) is in the range of 100–1000. However, scattering decreases nearly monotonically with increasing wavelength. Furthermore, red and NIR light experiences highly forward-directed scattering interactions in tissue, characterized by an anisotropy parameter $g = 0.8$ – 0.95 . Melanin absorption, too, decreases with increasing wavelength. Hence, the red end of the visible spectrum provides a spectral window for optical radiation, even if water absorption increases there (see figure 8). The so-called ‘therapeutic window’ (Parrish 1981) reaches from about 600 to 1300 nm.

The first light sources used in LCI were multimode laser diodes (Fercher and Roth 1986). Then, later, available SLDs were used (Huang *et al* 1991). SLDs are still the dominating light sources; they span the wavelength range from about 675 to 1600 nm, have output powers up to 50 mW and spectral widths up to 70 nm. Specially developed broad-bandwidth versions based on a tandem structure (Semenov *et al* 1995) have a spectral width up to $\Delta\lambda = 98$ nm at a mean wavelength of $\bar{\lambda} = 820$ nm, but have not yet been commercialized.

LED sources which emit light of high space-coherence but low time-coherence have been developed for LCI applications in fiber technology. Clivaz *et al* (1992) used an EELED at a mean wavelength of $\bar{\lambda} = 1300$ nm with a bandwidth of $\Delta\lambda = 60$ nm in reflectometry. Derickson *et al* (1995) reported on a LED with reduced internal reflections operating at 1300 and 1550 nm, allowing high-sensitivity LCI without spurious responses. Unfortunately, all these light sources provide only beam powers in the range of some microwatts.

One of the most promising light sources for high-resolution and high-dynamic range OCT is the Kerr-lens mode-locked Ti : sapphire laser. Mode-locked operation has been demonstrated across a tuning range from 0.7 to 1.1 μm operating at a mean wavelength of approximately

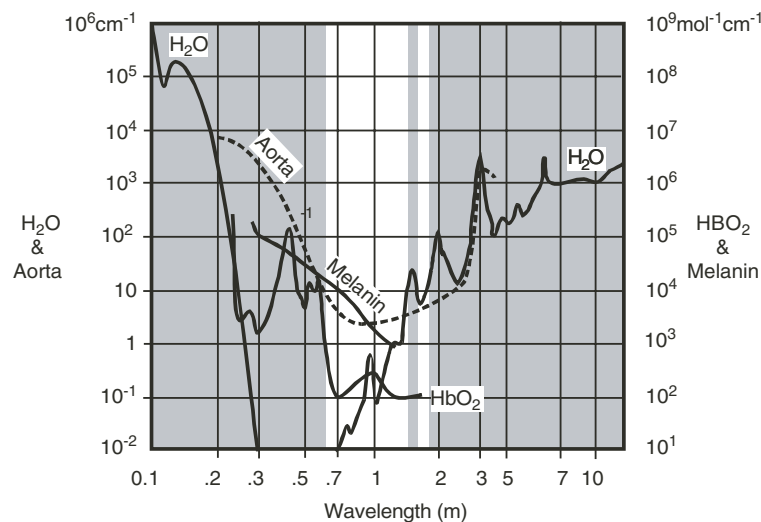


Figure 8. Spectral absorption of some tissue molecules, and of aortic tissue (---; postmortem). The brightened wavelength ranges have already been used in OCT. Adapted from Boulnois (1986) and Berlien and Müller (1989).

$\bar{\lambda} = 800$ nm (Fujimoto *et al* 1998). Using low-dispersion prism material led to greater bandwidth and smoother dispersion characteristics of the used double-chirped dispersion balancing mirrors. This has led to FWHM bandwidths of up to 400 nm at $\bar{\lambda} = 800$ nm at a power of 200 mW (Morgner *et al* 1999). Such a laser has been used in some of the most advanced OCT techniques like spectroscopic OCT (Morgner *et al* 2000) and ultra-high-resolution OCT (Drexler *et al* 1999, 2001).

Other sources of high power and low time-coherence light are ASE light sources. These are based on rare-earth doped optically pumped fibres as used in optical networks to optically amplify signals. The ASE light sources, however, use the ASE generated by these fibres (usually considered as noise in the fibre-optic telecommunications field). ASE light is also used to evaluate fibre optical components by low-coherence reflectometry and as low time-coherence light source in OCT. Rare-earth doped fluoride, tellurite and silica fibres realize broadband light sources operating in the 1.3–1.6 μ m region. Tm-doped fluoride fibres produce output spectra from 1440 to 1500 nm with output powers in the range of 50 mW and more. A superfluorescent Yb-doped high-power fibre ASE source developed by Bashkansky *et al* (1998a) operates at $\bar{\lambda} \sim 1.064$ μ m with a bandwidth of $\Delta\lambda \sim 30$ nm and yields beam powers of some tens of milliwatts. Er-doped and Tm-doped fibre sources have been used for OCT by Bouma *et al* (1998) (see table 1).

Photonic crystal fibres (PCFs) are another promising class of light sources emitting low time-coherence but high space-coherence light. PCFs are made up of a pure silica core surrounded by an array of microscopic air holes running along their entire length. The large refractive-index step between silica and air allows light to be concentrated into a very small area, resulting in enhanced nonlinear effects. Broadening of the spectrum and formation of a supercontinuum increases for increasing peak input powers. However, it has also been demonstrated that ultrafast femtosecond pulses are not needed for efficient supercontinuum generation in photonic crystal fibres (Coen *et al* 2001).

Because of the large waveguide contribution to their group-velocity dispersion, PCFs can exhibit very unusual chromatic dispersion characteristics. Besides fibres, in which light

is guided by a bandgap created by the periodic arrangement of air holes (Ranka *et al* 2000), tapered fibres too (Birks *et al* 2000), can provide supercontinuum light of high space-coherence. Hartl *et al* (2001) have used a 1 m photonic crystal fibre source operating with 100 fs input pulses generated by a Kerr-lens mode-locked Ti:sapphire laser pumped by a frequency-doubled Nd:vanate laser and obtained 6 mW output power. Ultra-high-resolution OCT has been demonstrated with a depth resolution of approximately $2\ \mu\text{m}$ in tissue at $1.3\ \mu\text{m}$ centre wavelength and 370 nm bandwidth.

Experimental modifications of a PCF-based set-up including variations in prechirp and power, different fibre lengths and core sizes as well as dependences on polarization effects have all recently been investigated by Apolonski *et al* (2002). A correspondingly optimized PCF-based light source, pumped by a compact sub-15 fs, commercially available Ti:sapphire oscillator yielded sub-micron axial resolution in a spectral region between 550 and 950 nm. Figure 10(c) (section 3.3.2) depicts the emission spectra (left) and the corresponding interference signal (right). A spectrum with 325 nm FWHM bandwidth centred at 725 nm, with minimal spectral modulations and power output up to 27 mW was generated. Sidelobes that appear in the $\pm 1\text{--}3\ \mu\text{m}$ delay range were less than 5% of the signal maximum. A demonstration of the near-histologic resolution obtainable with such light sources is presented in figure 26.

It will be a matter of intensive further investigation to evaluate the final suitability of novel light sources like ASE light sources and PCFs for OCT, especially for *in vivo* clinical applications. At the moment, they represent an attractive, flexible alternative to investigate new wavelength regions for ultra-high resolution, functional OCT; see also section 6.

3.3. Spectral structure

3.3.1. Spectral width. Three important parameters of the coherence function can be affected by manipulations of the spectrum: width, smoothness and position.

OCT depth resolution (equation (1.1)), as well as spectrometric resolution is defined by the spectral width $\Delta\lambda$ of the light source. Figure 9 demonstrates depth resolution in

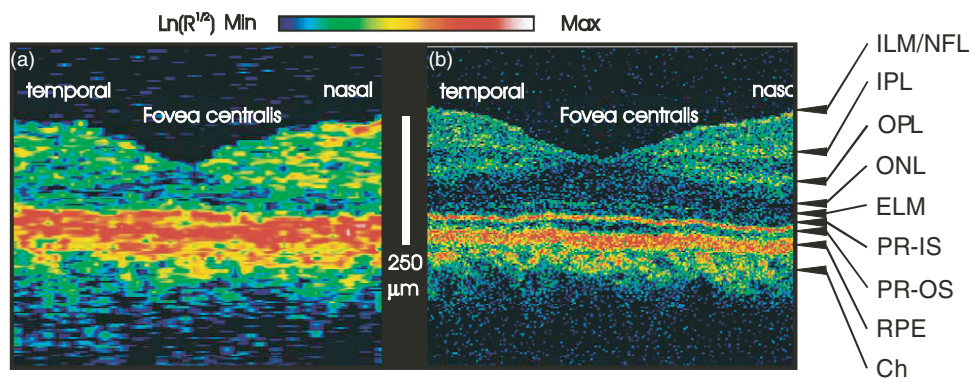


Figure 9. Topographical *in vivo* mapping of retinal layers at the *Fovea centralis* along $\sim 3\ \text{mm}$ of the papillomacular axis. The logarithm of the LCI signal is represented on a false-colour scale shown on top of the figure. (a) SLD: mean wavelength $\bar{\lambda} = 843\ \text{nm}$; $\Delta\lambda = 30\ \text{nm}$; depth resolution $10\ \mu\text{m}$. (b) Ti:Al₂O₃ laser: mean wavelength $\bar{\lambda} = 800\ \text{nm}$; $\Delta\lambda = 260\ \text{nm}$; $3\ \mu\text{m}$ depth resolution. The layers are (from top): ILM/NFL = inner limiting membrane/nerve fibre layer; IPL = inner plexiform layer; OPL = outer plexiform layer; ONL = outer nuclear layer; ELM = external limiting membrane; PR-IS = photoreceptors inner segment; PR-OS = photoreceptors outer segment; RPE = retinal pigment epithelium; Ch = choriocapillaris and Choroid. Adapted from Drexler *et al* (2000). Courtesy of Fujimoto, MIT. Reprinted by permission from Kugler Publications, The Netherlands.

OCT using a superluminescent diode and, for comparison, a state-of-the-art Kerr-lens mode-locked Ti:sapphire laser. Note the clear delineation of retinal layers in figure 9(b), which is a prerequisite for the analysis of several retinal diseases.

The broad bandwidth of the Kerr-lens Ti:sapphire laser is forced by mode-locking. Alternative solutions to obtain comparable broad-bandwidth light were based on fluorescence of Ti:sapphire (Clivaz *et al* 1993, Kowalevich *et al* 2002) but obtained extremely low powers. Higher powers of fluorescent light (9 mW) were obtained using an argon-ion laser pumped 1 μm diameter point fluorescence source in a Rhodamine 590 jet (Liu *et al* 1993), yielding a coherence length of $l_C = 5.8 \mu\text{m}$.

Quite another solution of the spectral-width-problem is to synthesize an optical source by combining several light sources with adjacent spectral bands. The width of the composite auto-correlation function of a synthesized source can be narrower than the single auto-correlation functions. Related work in the OCT field has been published by Schmitt *et al* (1997), Baumgartner *et al* (1998), Zhang *et al* (2001a, b, c) and Tripathi *et al* (2002), but remained insignificant so far.

3.3.2. Spectral modulation. As will be shown in section 4 standard OCT imaging uses twice the real part of the coherence function of the source light $\Gamma_{\text{Source}}(\tau)$ as depth PSF. This function, therefore, must have a narrow half-width and must not have satellites. Since $\Gamma_{\text{Source}}(\tau)$ equals the inverse FT of the source power spectrum the latter must have a smooth shape. Figure 10 presents a comparison of spectra and corresponding depth PSFs of a xenon short arc lamp, a SLD, and a photonic crystal fibre source. The broad pedestal of the xenon spectrum will provide a very narrow PSF, but the irregular spectral attachment adds a fluctuating pedestal to the coherence function. The fluctuating part will not be filtered out by the heterodyne band-pass filter, and will, therefore, reduce image contrast (Fercher *et al* 2000). Most SLDs have, due to their smooth emission spectrum, a more or less ideal smooth depth PSF. Unfortunately, the bandwidth of commercially available SLDs is rather limited. The photonic crystal fibre provides much more power and a much larger bandwidth but suffers from spectral modulation.

The width of the coherence function is ruled by the Fourier uncertainty relation, which says that the product of the variances of a FT pair reaches its minimum for Gaussian functions. Therefore, in the majority of cases a Gaussian power spectrum is aimed by spectral shaping. Three basic possibilities have been used for coherence function shaping: digitally correcting the spectrum of the depth-scans (Tripathi *et al* 2002), time-domain spectral shaping (Chou *et al* 2000), and frequency-domain spectral shaping (Weiner *et al* 1988, 1990), Hillegas *et al* (1994), and Teramura *et al* (1999). These techniques can be used to obtain Gaussian spectra from non-Gaussian sources and can, therefore, simplify the development of new low-cost broadband sources.

3.3.3. Spectral phase. The position of the coherence function is ruled by the Fourier shift theorem, which says, that a shift of a time function is equivalent to a (wavelength-dependent) phase shift of its Fourier components (equation (2.36)). Corresponding experiments have been described by He and Hotate (1999), who scan a coherence function through the sample depth; depth resolution was 475 μm , the detection range was 12.2 mm, both measured in air. A similar technique has been described by Teramura *et al* (1999) who describe linear shifting of the coherence function and image detection of selected planes of a multilayer object without mechanical scanning. These techniques have the potential to replace optical delay lines (section 4.1.4).

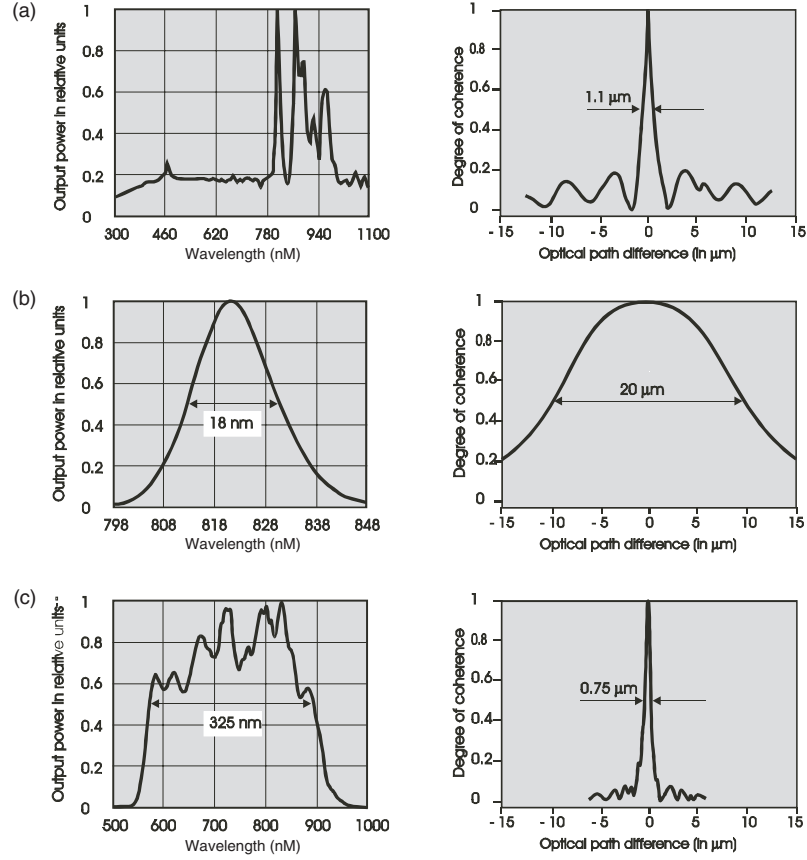


Figure 10. Optical output spectrum (left) and OCT depth spread function (right): (a) xenon short arc lamp (OSRAM XBO 75); (b) a superluminescent diode and (c) a photonics crystal fibre source.

4. Low-coherence interferometry and OCT

4.1. Time-domain OCT

Two scans have to be performed in standard OCT: the lateral OCT scan addresses laterally adjacent sample positions whereas the OCT depth-scan uses time-domain LCI to detect depth positions of light re-emitting sites in the sample. There are two basic low-coherence interferometry techniques in the time-domain; both use two-beam interferometry: in the reflectometer technique the sample is inside the interferometer and illuminated by the sample beam only (figure 11), whereas in the dual beam technique the sample is outside the interferometer and illuminated by both interferometer beams (figure 12).

4.1.1. Reflectometry OCT. This is the traditional OCT technique (Huang *et al* 1991). It is based on the reflectometry LCI principle (Danielson and Whittenberg 1987). In the most straightforward case reflectometry LCI is performed in a Michelson interferometer with the sample in one arm by translating the reference mirror continuously along the beam axis.

The averaged intensity at the interferometer exit is $\bar{I}_E(\tau) = \langle I_S(t) \rangle + \langle I_R(t) \rangle + 2\text{Re}\{\Gamma_{SR}(\tau)\}$ with the interferogram $2\text{Re}\{\Gamma_{SR}(\tau)\} = G_{SR}(\tau) = 2\sqrt{\langle I_S(t) \rangle \langle I_R(t) \rangle} |\gamma_{SR}(\tau)| \cos[\alpha_{SR} - \delta_{SR}(\tau)]$ (see equations (1.8) and (1.9)).

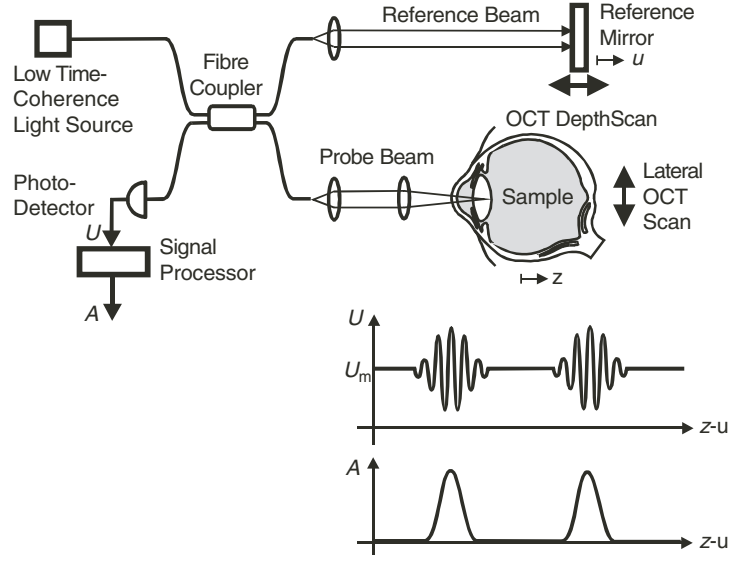


Figure 11. Time-domain reflectometer LCI in fibre optics technology. $U - U_m = U_G(\tau) = \text{LCI}$ signal. A is the real envelope. Signals generated at only two light re-emitting sites (anterior corneal surface and Bruch's membrane in the fundus of the eye) are indicated.

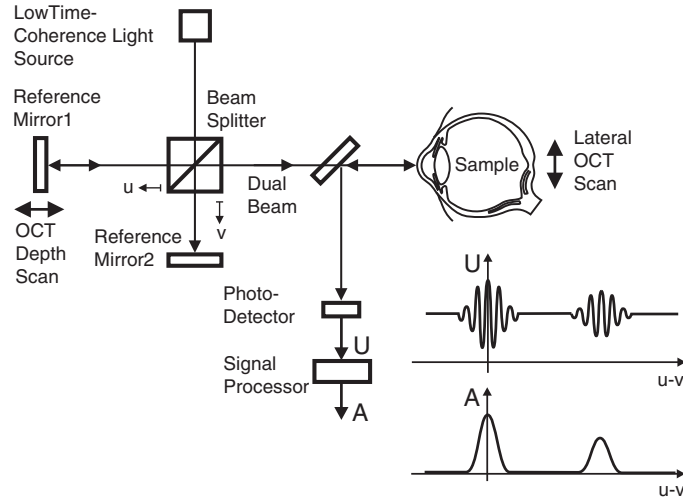


Figure 12. Dual beam LCI in free-space optics technology. The anterior corneal surface serves as the dominating interface. $U - U_m = U_G = \text{LCI}$ signal. A is the real envelope. Only signals of the anterior corneal surface and of Bruch's membrane in the fundus of the eye are indicated.

The interferogram at the interferometer exit without any sample in the interferometer equals—besides a constant depending on beam splitter and mirror reflectivities—twice the real part of the the coherence function $\Gamma_{\text{Source}}(\tau)$ of the source light:

$$G_{\text{SR}}(\tau) = 2\text{Re}\{\Gamma_{\text{SR}}(\tau)\} = 2\text{Re}\{\Gamma_{\text{Source}}(\tau)\} = G_{\text{Source}}(\tau). \quad (4.1)$$

A sample generates a beam, which—treating the interferometer as a linear shift invariant system—can be expressed as

$$V_S(t) = \int_{-\infty}^{\infty} V(t')h(t-t') dt' = V(t) * h(t), \quad (4.2)$$

where ‘*’ means convolution, $V(t)$ is the probe beam and $h(t)$ the response function of the sample. The FT of the sample response function

$$H(\nu) = \text{FT}\{h(t)\} \quad (4.3)$$

is the sample transfer function. Obviously, $h(t)$ is the local (related to z by the speed of light) amplitude reflectivity.

The interferogram with a sample in the probe arm can readily be shown to be twice the real part of the source coherence function $\Gamma_{\text{Source}}(\tau)$ convolved with the sample response function or backscattering profile $h(\tau)$ (Fuji *et al* 1997):

$$G_{\text{SR}}(\tau) = 2\text{Re}\{\Gamma_{\text{SR}}(\tau)\} = 2\text{Re}\{\Gamma_{\text{Source}}(\tau) * h(\tau)\}. \quad (4.4)$$

$2\Gamma_{\text{Source}}(\tau)$ can be interpreted as the complex impulse response function and $G_{\text{Source}}(\tau)$ plays the role of a depth PSF in LCI and OCT. The Fresnel-reflecting interfaces sample model, e.g. associates amplitude reflectivities $\sqrt{R(\tau)}$ with the backscattering profile $h(\tau)$ (Pan *et al* 1995). From a more physical point of view LCI and OCT detect high frequency components of the sample’s scattering potential (see section 2.1).

The spectral interferogram (in the frequency domain) with a sample in the probe arm corresponding to equation (4.4) is

$$W_{\text{SR}}(\nu) = S_{\text{Source}}(\nu)H(\nu), \quad (4.5)$$

where $W_{\text{SR}}(\nu) = \text{FT}\{\Gamma_{\text{SR}}(\tau)\}$ is the cross-spectral density of sample and reference beam,

$$S_{\text{Source}}(\nu) = \text{FT}\{\Gamma_{\text{Source}}(\tau)\} \quad (4.6)$$

is the power spectrum or spectral density of the source light, and $H(\nu)$ the sample transfer function.

The power spectrum of many light sources used in LCI and OCT can be approximated by a Gaussian spectrum

$$S_{\text{Source}}(\nu) \propto e^{-4 \ln 2 ((\nu - \bar{\nu})^2 / \Delta \nu^2)}, \quad (4.7)$$

which yields a depth PSF

$$\text{Re}[\Gamma_{\text{Source}}(z)] \propto e^{-4 \ln 2 (z/l_{\text{FWHM}})^2} \cos\left(\frac{2\pi}{\bar{\lambda}} z\right) = e^{-(\pi \cdot \Delta \nu \cdot z / 2c \sqrt{\ln 2})^2} \cos\left(2\pi \bar{\nu} \frac{z}{c}\right) \quad (4.8)$$

with FWHM-width l_{FWHM} and with FWHM-width $\Delta \nu$. Since backscattered light travels twice through the sample,

$$l_c = \frac{l_{\text{FWHM}}}{2} = \frac{2 \ln 2}{\pi} \frac{\bar{\lambda}^2}{\Delta \lambda} \quad (4.9)$$

is used as a so-called round trip coherence length (equation (1.1)) and used as a measure of depth resolution in OCT (see section 2.6).

Time-domain OCT has a high potential for adaptation to various further developments like spectroscopic OCT, Doppler OCT (DOCT) and other techniques. Its two basic disadvantages are that a depth-scan has to be performed and that it operates point-like. The first disadvantage can be avoided by Fourier-domain OCT (see section 4.2), the second disadvantage can be avoided by parallel OCT (see section 4.3). Nevertheless, reflectometric time-domain OCT is the basis of a commercial OCT instrument (Carl Zeiss Meditec AG).

4.1.2. Dual beam OCT. Dual beam OCT is based on dual beam LCI (Fercher and Roth 1986). The sample is illuminated by both beams exiting from a two-beam interferometer (see figure 12). Interference is observed, if the path difference of the interferometer coincides with path differences between light re-emitting sites within the sample. Hence, on the one hand, depth measurement precision is not degraded by unavoidable movements of a living sample. On the other hand, the depth-scan signal is an auto-correlation signal and does only provide a non-ambiguous image if one interface in sample space (of the sample itself or of a transparent plate deployed in front of the sample) dominates.

Dual beam OCT has initially been used in Fabry–Perot configuration to obtain tomographic images of the eye's fundus (Fercher *et al* 1993a) and later in Michelson configuration in a clinical setting to generate tomographic images of different pathological cases like glaucoma, diabetic retinopathy and age-related macular degeneration (Drexler *et al* 1998).

4.1.3. En-face OCT. This technique has been introduced by Izatt *et al* (1994) to microscopy. It yields transversal sections of the sample. A fast lateral scan is performed by the sample itself or the probe beam, whereas the reference mirror is used to adjust the depth of these scans. The optical scheme of an OCT device implemented in fibre optics technology is shown in figure 13. Since there is no depth-scan-generated heterodyne frequency, a separate phase modulation is either introduced to the reference or the sample beam. Izatt *et al* (1994) have shown that the coherence gate can substantially improve the probing depth of microscopy. In particular, it can enhance confocal microscopy when the collected signal at the focal plane is dominated by light scattered from other planes.

Later, Podoleanu *et al* (1998) used the *en-face* technique to generate OCT images of objects such as a human retina *in vivo*. In an extension of that technique stacks of transversal OCT images were generated and three-dimensional profiles of the tissue thus constructed; longitudinal images could be generated by software at any transversal position in the stack (Podoleanu *et al* 2000). In a further advancement, the area and volume measurement of tissue segments were demonstrated (Rogers *et al* 2001).

4.1.4. Heterodyne detection and delay lines. Since noise associated with optical detection shows either a distinct frequency dependence or is proportional to signal bandwidth, frequency

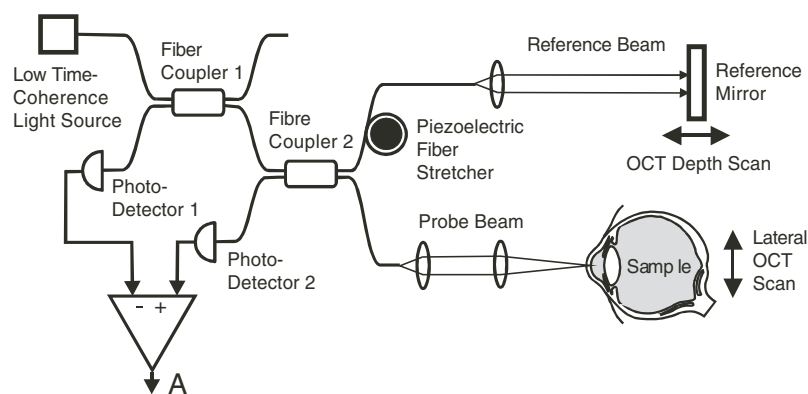


Figure 13. *En-face* OCT implemented in fibre optics technology with dual balanced detection (photodetectors 1 and 2) for intensity fluctuation compensation (Izatt *et al* 1994, Podoleanu *et al* 1998). Light exiting from the one port of the fibre coupler 1 is inserted into a fibre optics Michelson interferometer formed by fibre coupler 2 (light from the second port is not used).

filtering can reduce that noise while still retaining the useful information. In heterodyne detection the sample wave is combined at the interferometer beam splitter with the reference wave derived from the same source but offset in frequency. As a result of this coherent mixing of the two light waves the signal frequency is converted to the difference frequency or heterodyne frequency. The heterodyne signal is detected and analysed by an appropriate electrical circuit.

Most common in LCI and OCT is the use of a delay line to shift the coherence gate along the sample depth. Frequently, a reference mirror moving with speed V_{Mirror} and simultaneously generating a corresponding Doppler frequency shift is used. In many cases that Doppler shift provides a sufficient frequency offset needed to implement the electronic heterodyne detection technique. An exception is the *en-face* OCT technique where a piezoelectric fibre stretcher, an acousto-optic modulator, or another phase modulation technique is used to obtain an adequate heterodyne frequency. Let us have a closer look at the Doppler technique.

Let time t and reference mirror position z be related by $z(t) = V_{\text{Mirror}}t$ and assume a $\delta(z)$ -like sample interface at z_0 . Since the reference mirror moves in air it generates a time delay

$$\tau(t) = 2 \frac{z_0 - V_{\text{Mirror}}t}{c}. \quad (4.10)$$

The corresponding (Doppler-) frequency shift

$$\Delta\nu = \frac{2}{\lambda} V_{\text{Mirror}} \quad (4.11)$$

is the heterodyne frequency.

LCI and OCT are based on the interference of wave groups. Their propagation speed is the group velocity v_G :

$$v_G = \frac{c}{n_G}, \quad (4.12)$$

with the group index $n_G = n - \lambda(dn/d\lambda)$ and the refractive index n , whereas the carrier wave moves with phase velocity v_P :

$$v_P = \frac{c}{n}. \quad (4.13)$$

Hence, a mirror shift Δz is related to a shift d of the coherence degree $\gamma_{\text{SR}}(\tau)$ by the group index:

$$d = \frac{\Delta z}{n_G}. \quad (4.14)$$

Many delay lines are simply based on changing the geometrical and/or optical path length in the sample or reference arm of the interferometer. For example, the reference mirror is mounted on scanning stages moved by stepper motors (Huang *et al* 1991), can be moved by loudspeaker cones (Sala *et al* 1980) and reel-driven stages (Edelstein *et al* 1991), or can be mounted on an oscillating arm (Harde and Burggraf 1981). High speed delay lines have also been implemented with rotating cubes (Ballif *et al* 1997, Szydlo *et al* 1998), rotating mirrors (Campbell *et al* 1981), and circulating or oscillating rooftop prisms (Swanson *et al* 1993). The main disadvantage of such delay lines is that masses have to be moved with high accelerations, which leads to mechanical vibrations and reduces the SNR. Therefore, several attempts have been made to avoid moving of masses. One such attempt uses piezo-actuated fibre stretchers (Tearney *et al* 1996b). But these devices are not temperature stable and suffer from further problems like fibre dispersion. Another non-moving delay line has been proposed on the basis of an acousto-optic Bragg cell device (Riza and Yaqoob 2000).

A shift of the coherence gate can also be achieved by modulating the phases of the monochromatic components of the beam, as can be seen from equation (2.36). Corresponding techniques based on modifying the spectral components have been developed in the field of femtosecond pulse shaping (Weiner *et al* 1988). Kwong *et al* (1993) describe a delay line using the offset of beam components when diffracted by a grating. Tearney *et al* (1997b) have introduced this delay line to OCT. Rollins *et al* (1998) demonstrated its high speed capability in an OCT imaging system operating at up to video rate. Zeylikovich *et al* (1998) describe a related technique to generate two-dimensional tomograms where both, depth- and transverse-scanning are based on the diffraction grating technique.

4.2. Fourier-domain OCT

Fourier-domain OCT is based on equation (2.9). Whereas in standard OCT two scans have to be performed, only the lateral OCT scan has to be performed in the Fourier-domain technique. Depth-scan information is provided by an inverse FT of the spectrum of the backscattered light. The backscattered field amplitude $A_S(K)$ is obtained either by spectral interferometry techniques or by wavelength tuning techniques.

4.2.1. Spectral interferometry Fourier-domain OCT. This technique is based on equation (2.12):

$$F_S(z) \propto \text{FT}\{A_S(K)\}. \quad (4.15)$$

Here the spectrum of the backscattered sample light amplitude $A_S(K)$ is obtained using a spectrometer. Indeed, since the interferogram and the cross-spectral intensity (equation (1.16)) are FTs of each other (Born and Wolf 1999), the inverse FT of the spectral interferogram intensity at the interferometer exit yields the same signal as obtained by low coherence interferometry (Fercher *et al* 1993b). The optical scheme of a corresponding interferometer is shown in figure 14. In contrast to time-domain techniques only the lateral OCT scanning procedure remains. The time-consuming mechanical OCT depth-scan can be put aside. It is replaced by a spectrometric measurement. There are again two basic techniques: the correlation technique and the phase shifting technique. Both techniques use the spectrally

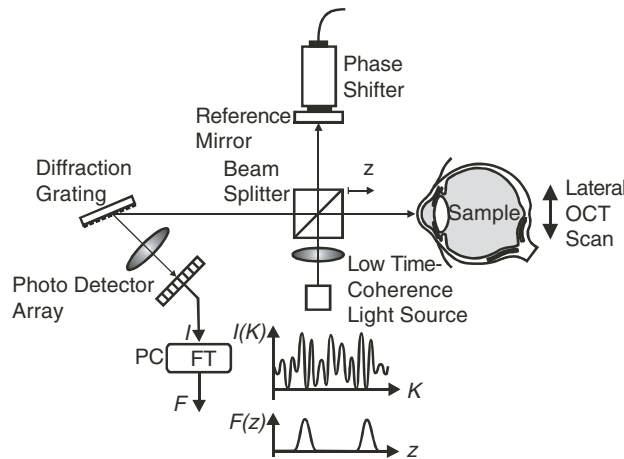


Figure 14. Spectral interferometry. FT = signal processor performing the FT. I = spectral intensity; F = scattering potential.

resolved interferogram obtained with a spectrometer at the exit of an interferometer. With the sample in one arm of a Michelson interferometer, as depicted in figure 14, the spectral intensity at the interferometer exit is:

$$I_{SR}(K) = I_S(K) + I_R(K) + 2\sqrt{I_S(K)I_R(K)}\text{Re}\{\mu(K)e^{i[\Phi_S(K)-\Phi_R(K)]}\}. \quad (4.16)$$

$I_S(K) = |A_S(K)|^2$ is the spectral intensity (or power spectrum) of the sample beam, and $A_S(K) = a_S(K)e^{i\Phi_S(K)}$ its complex amplitude. $I_R(K)$ is the power spectrum of the reference beam, and $\mu(K)$ the spectral degree of coherence ($=1$, if light sources emitting spatial monomode light are used). $\Phi_S(K)$ is the spectral phase of the sample wave and $\Phi_R(K)$ the spectral phase of the reference beam.

Depth resolution in both, in time-domain OCT (equation (4.9)) as well as in Fourier-domain OCT (equation (2.31)) depends on the spectral width $\Delta\lambda$ of the optical source. OCT depth field of view (FOV), however, is quite different in time- and Fourier-domain OCTs. Whereas in the time-domain technique the extent of depth FOV is limited by the scanning range of the reference beam (and system sensitivity), depth FOV in Fourier-domain OCT is limited by the resolution of the spectrometric device. Let us assume, e.g. the reference mirror at $z = 0$ and a δ -like object structure at z_S . With $\mu(K) = 1$ the interferogram of equation (4.16) is $2\sqrt{I_S(K)I_R(K)}\cos\{Kz_S\}$ with the spectral interferogram frequency

$$\omega_K = z_S \quad (4.17)$$

in K -space. From the sampling theorem (Bracewell 2000) it follows that

$$N = \frac{\Delta K}{\pi} z_S \quad (4.18)$$

equidistant sampling points are required to specify that interferogram or, to specify the position z_S of the sample (with depth resolution corresponding to ΔK). Hence, depth FOV is limited by the number N of single detectors, whereas depth resolution is limited by the spectral width ΔK comprehended by the detector array.

Unfortunately, the Fourier components $A_S(K)$ of the scattering potential $F_S(z)$ cannot be obtained in a straightforward manner. The correlation technique, for example, plainly FTs the spectral intensity $I(K)$ at the interferometer exit (Fercher *et al* 1991). Since $I(K)$ equals the squared magnitude of the inverse FT of the sum $F(z)$ of the scattering potentials of the sample and reference arm: $I(K) = |V^{(S)}(K)|^2 \propto |\text{FT}^{-1}\{F(z)\}|^2$, we have

$$\text{FT}\{I(K)\} \propto \langle F^*(z) \cdot F(z+Z) \rangle = \text{ACF}_F(Z). \quad (4.19)$$

With a δ -like reflectivity (magnitude R) of the reference mirror at z_R the complete backscattering potential is $F(z) = F_S(z) + \sqrt{R} \cdot \delta(z - z_R)$ and the auto-correlation yields four terms:

$$\text{ACF}_F(Z) = \text{ACF}_{F_S}(Z) + \sqrt{R} \cdot F_S^*(z_R - Z) + \sqrt{R} \cdot F_S(z_R + Z) + R \cdot \delta(Z). \quad (4.20)$$

The first term on the right-hand side yields the auto-correlation of the sample structure centred at $Z = 0$; the second term yields a complex conjugate version of the sample centred at $Z = z_R$; the third term yields—besides the constant factor \sqrt{R} —a true representation of the sample structure, centred at $Z = -z_R$, and the last term yields an additional peak at the origin of the reconstructed sample space. To avoid overlapping of the reconstructed terms, the reference mirror must be put at a position twice the sample depth apart from the next sample interface.

The technique described so far, also called ‘spectral radar’, has been implemented in free-space optics LCI (Fercher *et al* 1995) for the measurement of intraocular distances as well as in fibre optics OCT (Häusler and Lindner 1998) to obtain tomograms of human skin and the structure of multilayered printed circuit boards (Lindner *et al* 2002). Zuluaga and

Richards-Kortum (1999) presented a parallel Fourier-domain OCT technique using an imaging spectrograph to obtain spatially resolved spectra. Their technique avoids moving parts even to perform the lateral OCT scan. Two-dimensional images of subsurface structures were obtained in real-time. A similar parallel Fourier-domain OCT technique has been developed by Yasuno *et al* (2002a). Instead of digitally performing the FT these authors use analog-optical FT of the spectrum, performed by a BBO light modulator, to obtain the spatial depth structure. Using one-dimensional focusing of the probe beam at the sample, a one-shot near-real-time OCT imager has thus been realized.

The main advantage of the spectral technique is that no OCT depth-scan is needed and, therefore, data acquisition can be very fast. Its disadvantages are the expensive detector array (camera) and their small dynamic range. A specific disadvantage of the correlation technique is that the width of the auto-correlation of the object structure in object space equals twice the width of the object structure itself. Therefore, in object space, a range equal to twice the object depth is not available for representing the object structure and a considerable part of the bandwidth of the signal processing system is wasted.

The phase shifting LCI technique avoids the latter disadvantage. This technique uses the complex spectrally resolved amplitude $A_S(K)$. The real amplitude $a_S(K)$ can simply be obtained from the magnitude of the spectral interference term of equation (4.16), since the reference intensity is known. The spectral phases $\Phi(K)$ of the interference term of equation (4.16) can be obtained by a fitting procedure for the interferogram cosine function (Schwider 1990): if the reference phases are equidistantly distributed the magnitude $M(K)$ and the phase $\Phi(K)$ of the interferogram can be obtained from

$$M(K) = \sqrt{V^2(K) + W^2(K)} \quad \text{and} \quad \Phi(K) = \tan^{-1} \left[\frac{W(K)}{V(K)} \right] \bmod \pi, \quad (4.21)$$

with

$$V(K) = \sum_{n=1}^N I^{[n]} \cos \phi_n \quad \text{and} \quad W(K) = \sum_{n=1}^N I^{[n]} \sin \phi_n, \quad (4.22)$$

where

$$I^{[n]} = I_{\text{SR}} \left[\phi_0(K) + (n-1) \frac{\pi}{2} \right] \quad (4.23)$$

are the spectral intensities at wavelengths $\lambda = 4\pi/K$ recorded with reference phase settings $n = 0, 1, \dots, 4$, $\phi_0(K) = \Phi_S(K) - \Phi_R$.

Since the interference term contains three unknown functions a minimum of three different reference phases is needed. To minimize phase calibration errors, Fercher *et al* (1999), e.g. adopted a 5-frame method introduced by Schwider *et al* (1983) and calculated the phase of the interferogram by the formula

$$\Phi(K) = \tan^{-1} \frac{-I^{[1]} + 4I^{[2]} - 4I^{[4]} + I^{[5]}}{I^{[1]} + I^{[2]} - 6I^{[3]} + 2I^{[4]} + I^{[5]}}. \quad (4.24)$$

Equation (2.13) then yields the depth-scan OCT signal or sample scattering potential along the probing beam.

This technique has been used to generate dermatological OCT images (Fercher *et al* 1999, Hitzengerger and Fercher 2002) and in ophthalmological imaging (Wojtkowski *et al* 2002a, b). Its advantage is that the whole object depth offered by the detector array can be exploited. A disadvantage, however, is that five (at least three) spectra have to be recorded. Recently, Leitgeb *et al* (2002) have presented another technique for removing the disturbing auto-correlation of the sample structure. The spectral interferogram recorded by the photodetector array is from equation (4.19):

$$I(K) = \text{FT}^{-1}\{\text{ACF}_F(Z)\} = |\hat{F}(K)|^2 = |\hat{F}_S(K)|^2 + R + 2\sqrt{R}|\hat{F}_S(K)| \cos(Kz_R). \quad (4.25)$$

The sample auto-correlation is generated by Fourier-transforming the magnitude square of the dc term R and the sample spectrum $|\hat{F}_S(K)|^2$. Both terms can be removed from the spectral interferogram by recording two spectral interference patterns in phase opposition and subtracting the second spectrum from the first one; a similar technique has been used by Schlueter (1980) to remove the dc term from interference patterns. Thus, the disturbing auto-correlation term disappears and the full sample space is utilizable.

4.2.2. Wavelength tuning Fourier-domain OCT. Wavelength tuning interferometry (WTI) too, is based on equation (2.12). But, whereas spectral interferometry records the spectrally resolved intensity $I_{SR}(K)$ at the interferometer exit by a spectrometer detector array simultaneously in a parallel mode, WTI records $I_{SR}(K)$ sequentially (Fercher *et al* 1995). A single photodetector is used at the interferometer exit and the spectrum is recorded while tuning the light source. WTI has a previous history. Hymans *et al* (1960) described a radar system using a sawtooth frequency sweep. Later, fibre-optic frequency-domain reflectometry techniques were described using a rf-modulated laser beam (MacDonald 1981) and using a frequency tuned He-Ne laser (Eickhoff and Ulrich 1981). At present, the most promising tunable light sources are semiconductor lasers and solid-state lasers. To achieve wavelength tuning, either the gain margins of the cavity modes have to be rearranged or the frequency of the cavity modes must be shifted. Several techniques like distributed Bragg reflector lasers (Takada and Yamada 1996), multisection distributed feedback lasers, multiple cavity lasers, external cavity lasers with rotating-grating reflectors, and filter techniques have been developed (Koch and Koren 1990).

Two WTI techniques have been used so far in LCI and OCT. The first technique used in OCT is based on the beat frequency when interfering two delayed versions of a frequency sweeping (or ‘chirped’) light wave. In fact, let $\beta = d\omega/dt$ be the constant chirp rate. Then, the instantaneous light frequency is $\omega(t) = \omega_0 + \beta t$ and the phase delay between sample and reference beam is

$$\delta_{SR}(\Delta z) = \frac{\Delta z}{c} \frac{d\omega}{dt} t. \quad (4.26)$$

Hence, the interferogram beats with the depth-related chirp frequency $(\Delta z/c) \cdot \beta$, Δz is the object depth based on the reference mirror position. Fourier transforming the beat signal yields the sample depth structure: the magnitude of the beat signal defines the amplitude reflectance and the beat frequency defines the depth position of light re-emitting sites in the sample. Chinn *et al* (1997) used a grating-tuned external cavity superluminescent LED with a peak gain at 840 nm to obtain the first WTI OCT images of a sample of glass cover slips. Instead of rotating the grating, an intermediate mirror mounted upon a rotating galvanometer was used. A sweep frequency of 10 Hz was achieved at 35 mW output power. In a similar approach (‘Chirp OCT’), Haberland *et al* (1998) used a three-section laser diode. Modulating the injection current a mode-hop free tuning range of 0.8 nm, at 852 nm centre wavelength, at a mean output power of 6 mW has been obtained. The tuning speed was 160 nm s^{-1} . The generation of OCT images of solid phantoms and DOCT images of tubes filled with liquids has been demonstrated. Golubovic *et al* (1997) used a cw chromium-doped forsterite laser and obtained a tuning range of 1200–1275 nm that could be swept in less than 500 μs . Depth-scans could be performed with a scan rate of 2 kHz and an axial resolution of 15 μm .

A second WTI technique (Lexer *et al* 1997) is based on recording the wavelength-dependent interferometer exit signal $I_{SR}(K)$ and has been designed according to the correlation technique, described in section 4.2.1. Here too, an external-cavity tunable laser diode was used as the light source. The centre wavelength was 780 nm with a mode-hop free tuning range of $\Delta\lambda \sim 9 \text{ nm}$. A coarse tuning mode over the whole wavelength range of about 35 nm

accomplished by a low speed picomotor with a maximum tuning rate of about 0.33 nm s^{-1} was used for distance measurements on a model eye. A fine tuning mode over a narrow bandwidth of $\Delta\lambda \sim 0.18 \text{ nm}$ could be performed with a piezoelectric transducer at a maximum tuning rate of about 36 nm s^{-1} . *In vivo* measurements of intraocular distances have been performed in the latter case, however, the precision of these measurements was low (0.61 mm).

4.3. Parallel OCT

Standard time-domain OCT as well as *en-face* OCT are single-point detection techniques. Such techniques have already been used to generate two-dimensional OCT images up to video rate. Rollins *et al* (1998) recorded the beating heart of a *Xenopus laevis* embryo with an image acquisition rate of up to 32 frames per second and 125 depth-scans per frame. Podoleanu *et al* (2000) generated 112 *en-face* OCT images of a human optical nerve head at a rate of 2 frames per second and mounted these pictures to a three-dimensional data set, which can be used to observe the tissue volume from different viewing angles and to show slices with different orientations. At the end, however, single-point detection schemes at video rate have either limited sensitivity or a limited space-bandwidth product (resolved pixels per dimension). Parallel OCT uses linear or two-dimensional detector arrays of, respectively, N and N^2 single detectors. Since the variance of a random variable equals the square root of its mean, the SNR of a photodetector signal should roughly be proportional to the reciprocal square root of the number of photoelectrons—at least in the shot noise limit (see section 2.4). Therefore, provided a CCD array has the same quantum efficiency as a PIN diode and there are no light power constraints, the SNR when using linear or two-dimensional detector arrays can roughly be, respectively, \sqrt{N} and N times larger, compared to the single detector signal.

The disadvantages of using standard CCD sensors are, that due to their time-integrating operation, no ac-technique and no mixing and mode-lock detection seem possible. The

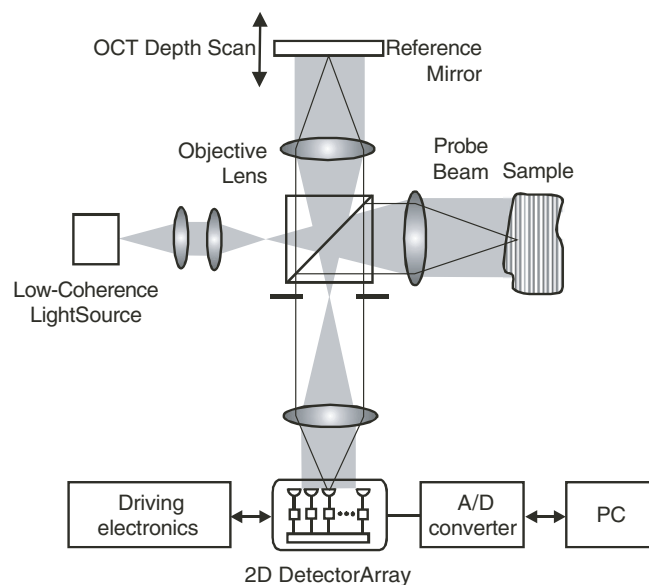


Figure 15. Parallel OCT set-up with a two-dimensional 58×58 pixel CMOS detector array where each single detector performs heterodyne detection in parallel (Bourquin *et al* 2001).

lack of an ac-mode opens the door to various $1/f$ noise sources, and the lack of narrow-band heterodyne demodulation techniques opens the door to bandwidth-dependent noise contributions like shot noise and excess noise. Two solutions to that discrepancy have been presented: Beaurepaire *et al* (1998) use synchronous illumination instead of the usual synchronous detection to obtain lock-in detection on every pixel of a CCD array-detector, whereas Bourquin *et al* (2000) have developed novel CMOS detector arrays with each 'smart pixel' consisting of photodetector and analog signal-processing electronics. In the CMOS detector array each single detector performs heterodyne detection in parallel thus dramatically increasing the dynamic range compared to a CCD array. A first one-dimensional array allowed optical signals to be detected at Doppler frequencies of 10 kHz up to 1 MHz, with a sensitivity of 66 dB, a dynamic range of 57 dB, and at a pixel readout rate of up to 3 MHz. Measurements on a test sample with 64 pixels in the lateral direction and 256 pixels in depth were performed with a depth resolution of $16.8\ \mu\text{m}$ ($\bar{\lambda} = 850\ \text{nm}$, $\Delta\lambda = 20\ \text{nm}$, $P_{\text{Source}} = 690\ \mu\text{W}$) at a frame rate of $25\ \text{s}^{-1}$. A corresponding two-dimensional 'smart pixel detector array' that made it possible to record a data set of 58×58 pixels and 33 slices with an acquisition rate of 6 Hz has been presented by Bourquin *et al* (2001) see figure 15. OCT pictures from scattering samples were obtained with volumetric pixel rates of $2.5 \times 10^6\ \text{s}^{-1}$ (Ducros *et al* 2002) and video-rate three-dimensional OCT pictures have been acquired at a sensitivity of 76 dB (at a sample beam power of 100 mW) using the two-dimensional smart pixel detector array (Laubscher *et al* 2002).

The synchronous illumination technique developed by Beaurepaire *et al* (1998) uses two modulations: first, a sinusoidal phase shift is introduced between the reference and sample beams providing an ac-signal. Of course, only the interferogram is modulated, not the incoherent background. Second, synchronous stroboscopic illumination is used to sample the interferometer signal at particular times within the phase shift period (Dubois *et al* 2002). The time-integrated signal at each pixel will then be dominated by synchronously detected interferometer signal contributions. Hence, band-pass character is obtained. A Linnik interference microscope (Steel 1983) has correspondingly been modified and yielded potential resolutions better than $1\ \mu\text{m}$ in depth and $0.5\ \mu\text{m}$ in the transverse direction with a sensitivity of $\sim 80\ \text{dB}$ at a $1\ \text{image s}^{-1}$ acquisition rate. High-resolution OCT images of onion epithelium were obtained using an infrared LED with a centre wavelength of 840 nm, a coherence length of $20\ \mu\text{m}$ and 40 mW output power.

To improve depth resolution a thermal light source has been used by De Martino *et al* (2001). A low power light bulb in a Linnik interferometer yielded full field interferometric images at 50 Hz acquisition rate with a fast CCD camera. Vabre *et al* (2002) used a 100 W tungsten halogen thermal lamp in a modified Linnik microscope and obtained a depth resolution of $1.2\ \mu\text{m}$. Water immersion has been used to compensate dispersion; corresponding immersion-objective lenses with a NA of 0.3 provided a transverse resolution of about $1.3\ \mu\text{m}$. A three-dimensional OCT image of a *Xenopus laevis* tadpole eye has been synthesized from 300 tomographic images (see figure 16).

5. Functional OCT

Function determines shape. At the molecular level, the enzymatic function of a protein determines its shape; at the organism level, specific niches available for animals determine corresponding morphological changes. Almost all entities in nature display a form which can be intimately related to their purpose and function. As a matter of fact, even plain morphologic images bear an intimate relation to the function of the corresponding entity and there is a smooth transition from morphologic to functional features. In this section we define as morphologic

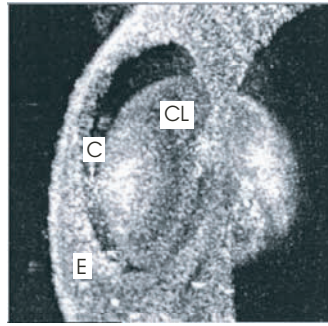


Figure 16. Reconstruction of the three-dimensional structure of a *Xenopus laevis* tadpole eye from 300 single tomographic images obtained with a Linnik-type interference microscope illuminated by a tungsten halogen lamp. C = cornea; CL = crystalline lens; E = exterior of the eye. Reproduced from Vabre *et al* (2002) by permission of the Optical Society of America.

features those which are related to the geometrical (or architectural) distribution of scalar scattering and reflection properties of the sample, and as functional properties those which include additional function dependent properties.

The interest in functional parameters from a medical point of view is based on the fact that functional disturbances usually precede morphological changes. Therefore, functional parameters are useful for early diagnosis of diseases. Such changes can be a modified blood flow, a change in tissue water content, a change in tissue oxygen pressure, and changes in tissue histology and architecture. The furthest advanced functional OCT techniques are Doppler techniques. Spectral OCT techniques are just making the step to clinical applications, whereas elastography, i.e. is still in an emerging state (Schmitt 1998b). Some of the more important functional techniques developed in OCT are presented in this section.

5.1. Polarization-sensitive OCT

A review by Wolman (1975) has already pointed to possibilities of selective visualization of anisotropic structures in tissue and the detection of morphological and functional changes using polarized light penetrating human tissue. Bickel *et al* (1976) have pointed out the fact that polarization effects in scattered light too can yield useful information about biological material. Later, a technique based on the degree to which light is depolarized when propagating inside tissues has been demonstrated for optical imaging in biomedical systems by Demos *et al* (1997). In a related work Schmitt and Xiang (1998b) showed that cross-polarized backscatter is caused by single scattering from non-spherical particles and by multiple scattering by large-diameter particles or particle clusters. Whereas differences in polarization cannot be used as a measure of the deviation of particles from spheres (Mishchenko and Hovenier 1995), birefringence of tissue can be estimated. Therefore, differences in the polarization state of the emerging light allows for the discrimination of different types of tissues.

Birefringence in tissue can be caused by two mechanisms: (a) intrinsic birefringence caused by anisotropic properties of the molecules, and (b) form birefringence caused by structure anisotropy resulting from ordered linear structures. Intrinsic birefringence can be found in dental enamel which consists of birefringent hydroxyapatite crystals. Form birefringence caused by linear and circular anisotropic proteins, such as collagen fibres which build up the extracellular matrix, can be found in many biological tissues. Form birefringence caused by nerve fibres oriented in parallel bundles is used, e.g. in the Nerve Fibre Analyser,

a confocal scanning laser ophthalmoscope with an integrated polarimeter used in glaucoma diagnostics to detect thinning of the retinal nerve fibre layer (NFL). It is based on retardation caused by birefringence of the peripapillary retina (Dreher *et al* 1992, Zangwill *et al* 2001).

The first polarization-sensitive (PS) LCI technique capable of characterizing the phase retardation between orthogonal linear polarization modes backscattered from a birefringent sample has been described by Hee *et al* (1992). Later, de Boer *et al* (1997, 1998) used PS-OCT for imaging of thermally damaged tissue and Everett *et al* (1998) and Schoenenberger *et al* (1998) used PS-OCT to measure birefringence and to generate birefringence maps of porcine myocardium. Hitzenberger *et al* (2001) used PS-OCT to generate OCT images depicting phase retardation and fast axis orientation in chicken myocardium.

Both birefringence and scattering change the polarization state of light propagating in turbid media. Furthermore, biological tissue cannot be assumed to be linearly birefringent with a fixed fast axis. Therefore, a complete description of polarization properties of light and samples should use Stokes parameters and Mueller matrices. The Mueller matrix \mathfrak{M} linearly relates the Stokes vector of the backscattered light \mathbf{P}' with the Stokes vector \mathbf{P} of the illuminating light (Huard 1996):

$$\mathbf{P}' = \mathfrak{M} \cdot \mathbf{P}. \quad (5.1)$$

A PS-OCT system, capable of yielding the full 4×4 Mueller matrix has been presented by Yao and Wang (1999) (see figure 17). The sample is illuminated by four different Stokes polarization states, achieved by rotating the half-wave plate and the quarter-wave plate in the source arm of the interferometer. With the variable wave-plate positioned in the reference arm four Stokes polarization states are sequentially generated for each of the four incident polarization states. From the reference intensity and the OCT-signal all 16 Mueller matrix element PS-OCT images can be obtained. Yasuno *et al* (2002b) have presented Mueller matrix images of human skin using spectral interferometry OCT.

De Boer *et al* (1999) used a depth resolved Stokes parameter technique and showed that polarization changes in fibrous tissue can be attributed to birefringence and that in some cases the optical axis can be determined when circularly polarized light is incident upon the sample. For a discussion of the effect of multiple scattering and speckle on the accuracy and noise of the computed Stokes parameters see de Boer and Milner (2002). A study on the application

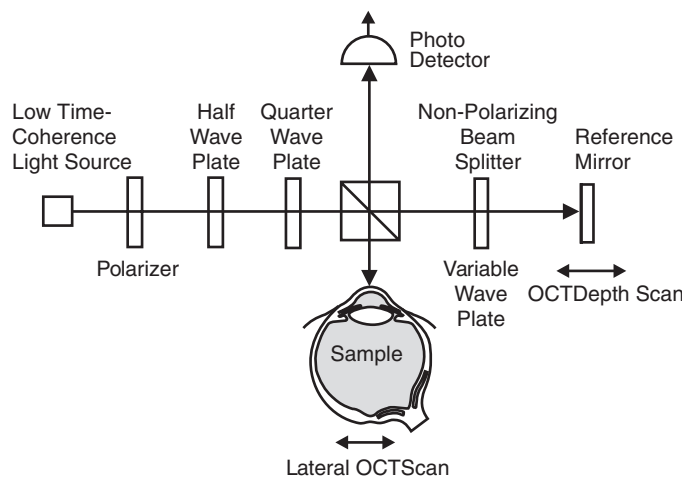


Figure 17. Mueller matrix element PS-OCT device. Redrawn from Yao and Wang (1999).

of PS-OCT for diagnosis of dental caries have been performed by Baumgartner *et al* (2000) and Fried *et al* (2002). Ducros *et al* (2001) used Stokes parameters for birefringence imaging and retinal NFL birefringence measurement in the Rhesus monkey retina.

Since in single-mode fibres orthogonal polarization states are degenerate, a straightforward implementation of PS-OCT in fibre optics technology is not possible. Furthermore, even polarization-maintaining fibres do not preserve the relative phase of their wave components; hence even these fibres cannot directly be used to determine the Stokes parameters of the sample beam. Saxer *et al* (2000) describe a high speed fibre-based PS-OCT system which can be used for *in vivo* measurements of the Stokes parameters of human skin. Insensitivity to differential phase delay between the degenerate orthogonal polarization states of single-mode fibres was achieved by a technique modulating the incident beam over four polarization states. Thus eight independent images (two independent Stokes vectors) are generated from which further polarization properties like retardance and optical axis orientation are obtained. Roth *et al* (2001) use three different polarization states to illuminate the sample sequentially and measure the component in the backscattered light returning in the same polarization state.

OCT, however, detects the coherent part of the backscattered light. Hence, the Jones matrix can be used in OCT as well (Jiao and Wang 2002). A large amount of work has already been based on the Jones formalism. The first PS-LCI set-up based on that formalism has been described by Hee *et al* (1992). It measures retardance independent of sample axis orientation, and therefore, many studies are based on that system. The basic scheme is a low-coherence Michelson interferometer, as shown in figure 18. A double-channel PS detection unit and polarizing components are attached. The sample is illuminated by a circularly polarized beam.

From the magnitudes of the envelopes $|I_V(z, \Delta z)|$ and $|I_H(z, \Delta z)|$ of the interference terms at the detectors of the vertical (index V) and horizontal (index H) polarization channels, sample reflectivity $R(z)$ and retardance $\delta_S(z)$, are obtained:

$$R(z) \propto |I_H(z, 0)|^2 + |I_V(z, 0)|^2, \quad (5.2)$$

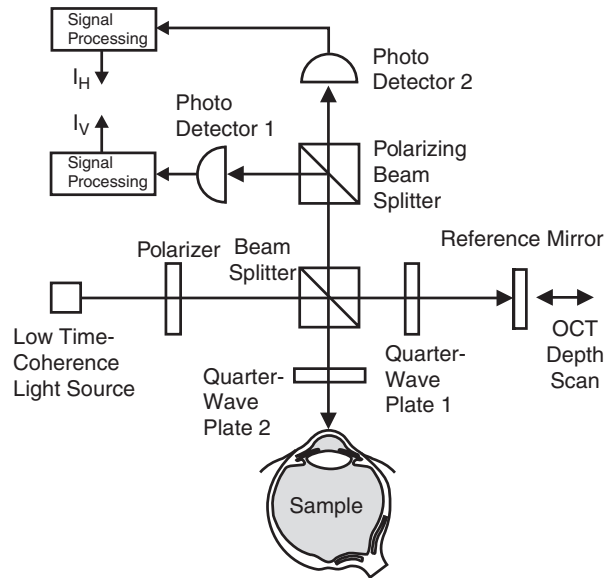


Figure 18. Optical scheme of a PS-LCI device according to Hee *et al* (1992). I_H , I_V = photodetector signals of horizontal and vertical polarization channel.

$$\delta_S(z) = \arctan \left(\frac{|I_V(z, 0)|}{|I_H(z, 0)|} \right). \quad (5.3)$$

The envelopes $|I_V(z, \Delta z)|$ and $|I_H(z, \Delta z)|$ can be obtained by demodulating the photodetector signals $I_V(z, \Delta z)$ and $I_H(z, \Delta z)$, at the carrier frequency $2k(d(\Delta z)/dt)$, or, after a phase sensitive recording of the full interferometric signals, by analytic continuation (since these signals do not contain negative frequency components), using the HT:

$$|I_{H,V}(z, \Delta z)| = \sqrt{(I_{H,V}(z, \Delta z))^2 + (\text{HT}\{I_{H,V}(z, \Delta z)\})^2}. \quad (5.4)$$

The information on the optic axis orientation is encoded entirely in the phase difference $\Delta\Phi = \Phi_V - \Phi_H$ of the two signals (de Boer *et al* 1997, Schoenenberger *et al* 1998, Hitzenberger *et al* 2001):

$$\theta_S = \frac{\pi - \Delta\Phi}{2}. \quad (5.5)$$

The angle of the fast axis with the x -direction, θ_S , is obtained from Φ_H and Φ_V , which can be derived by

$$\Phi_{H,V} = \arctan \left[\frac{\text{HT}\{I_{H,V}(z, \Delta z)\}}{I_{H,V}(z, \Delta z)} \right]. \quad (5.6)$$

Note that layered samples yield the depth-cumulated retardation and optic axis orientation.

Figure 19 presents a retardance image representing form birefringence of a human cornea. The cornea is a layered structure. Approximately 90% of the corneal thickness is constituted by stroma, consisting of stacked lamellae of collagen fibrils. This is a highly anisotropic structure. There are approximately 200 lamellae, extending from limbus to limbus and oriented at various angles to one another, less than 90° in the anterior stroma but nearly orthogonal in the posterior stroma (Kaufman *et al* 1998).

5.2. Doppler OCT

The Doppler effect is named after the Austrian physicist Christian Johann Doppler (1803–53) who explained and mathematically described the wavelength shift of the light of stars by their movement relative to earth (Doppler 1842). A hundred and sixty years later Doppler sonography has a 50 year story of achievements in the medical field (Duck *et al* 1998). Since the invention of the laser optical Doppler techniques have been developed and have successfully been introduced into the ophthalmological field by Riva *et al* (1972). LCI and OCT have led to a considerable expansion of optical Doppler techniques, due mainly to their localization property.

Besides their intrinsically diverse nature, medical sonographic and optical techniques are different mainly due to their dissimilar penetration depths. For example, the ultrasonic instrument designer's rule of thumb (Webb 1988) predicts an intensity attenuation coefficient of ultrasound of approximately $\mu_{US} = 10 \text{ dB cm}^{-1}$ for soft tissue at a frequency of 10 MHz (diagnostic ultrasonic imaging devices typically use frequencies between 1 and 15 MHz; in that frequency range μ_{US} is directly proportional to frequency). In contrast, with a typical optical scattering coefficient of soft tissue of $\mu_S = 10 \text{ mm}^{-1}$ (Schmitt and Kumar 1998a) and taking into account the high scattering anisotropy of soft tissue (figure 6, $g \approx 0.9$) we obtain an effective intensity attenuation of approximately 108 dB cm^{-1} for NIR light.

Optical Doppler techniques are based on the interference phenomenon if light scattered by moving particles interferes with a reference beam. The resulting interferogram beats at the Doppler angular frequency

$$\omega_D = \mathbf{K} \cdot \mathbf{v}_S. \quad (5.7)$$

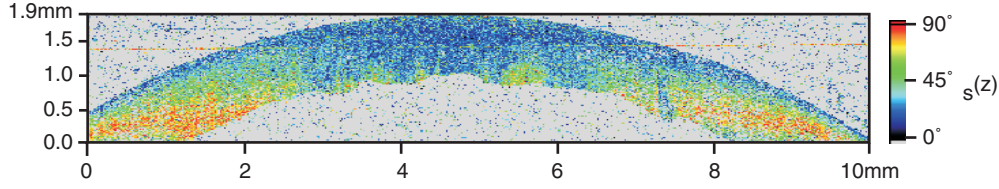


Figure 19. Retardance $\delta(z)$ of a human cornea illuminated from top (*in vitro*). The central part appears isotropic. Birefringence is observed towards the periphery. Courtesy of Götzinger.

\mathbf{K} is the scattering vector, and \mathbf{v}_S the velocity vector of the moving particles. The frequency resolution $\Delta\omega$ of corresponding measurement techniques is subject to the well known Fourier uncertainty relation (Bracewell 2000):

$$\Delta t \cdot \Delta\omega \geq \frac{1}{2}. \quad (5.8)$$

Δt is the measurement time, which plays a central role in the development and application of Doppler techniques.

The first laser Doppler technique has been described by Yeh and Cummins (1964). They used optical mixing spectroscopy, which is a direct analogue of the mixing of electrical signals in nonlinear circuit elements: whereas in the homodyne technique, beating occurs at the optical difference frequencies of the monochromatic components of the scattered light impinging at the photodetector, in the heterodyne approach, the sample light is mixed with a reference beam at the photodetector. The beats of these two waves are the basis of the Doppler techniques described in this section. The photocurrent is

$$i_{SR}(t) = \frac{qe\eta}{h\nu} G_{SR}(t), \quad (5.9)$$

see section 1. In general, i_{SR} will have stochastic properties; its power spectrum is obtained as the FT of the photocurrent auto-correlation function $ACF_i(\tau)$:

$$S_i(\nu) = \text{FT}\{ACF_i(\tau)\}, \quad (5.10)$$

where

$$ACF_i(\tau) = \langle i_{SR}(t)i_{SR}(t+\tau) \rangle. \quad (5.11)$$

If the reference intensity is much larger than the mean sample beam intensity the photocurrent power spectrum is

$$S_i(\nu) = q_e i_R + 2\pi i_R^2 \delta(\nu) + 2i_R \langle i_{SR} \rangle \text{FT}\{\text{Re}[\gamma_{SR}(\tau)e^{2\pi i\nu_R\tau}]\}, \quad (5.12)$$

where the first term is the shot noise, the second is the dc-term, and the third term is the heterodyne beating spectrum. Hence, the photocurrent beating spectrum equals the optical spectrum of the sample beam shifted to the centre frequency $\nu - \nu_R$ (Cummins and Swinney 1970).

Yeh and Cummins (1964) used light scattered from monodispersed polystyrene suspension laminar flow superimposed to a frequency-shifted reference beam. The minimum detectable velocity was obtained as $40 \mu\text{m s}^{-1}$. Localization was achieved by illuminating the flow parallel to the flow axis and detecting the scattered light from the side. Frequency shifts were measured at five radial positions and confirmed a parabolic velocity profile of laminar flow. Later, low-coherence interferometry has been introduced to photon correlation spectroscopy. Bizheva *et al* (1998) used the coherence gate to analyse the transition from single scattered light to light diffusion and its dependence on the system parameters, whereas Johnson *et al*

(1998) used low-coherence heterodyne interferometry to suppress multiple scattered light and extend the applicability of photon correlation spectroscopy into the multiple scattering regime.

Riva *et al* (1972) used the laser Doppler technique for blood velocity measurements at the fundus of the human eye and developed a bidirectional technique which allowed absolute measurements of the flow speed (Riva *et al* 1981). In these techniques the photodetector output was fed after amplification into a real-time spectrum analyser which provided the square root of the Doppler shift frequency spectrum at its output (which was then fed into an analog squaring module and the resultant spectrum displayed on an oscilloscope). A related low-coherence modification of that technique has recently been described by Logean *et al* (2000). By using light of varying coherence length and the vessel front wall as the reference mirror the velocity of red blood cells at different depths of retinal vessels could be selectively measured.

5.2.1. Fourier-transforming the fringe data. Gusmeroli and Martinelli (1991) described the first use of coherence gating in heterodyne laser Doppler velocimetry (LDV). They measured the velocity profile of seeded particles in water flowing in a duct by Fourier transforming the Doppler fringe signal. A superluminescent diode was used as a low time-coherence light source in a LCI configuration. Wang *et al* (1995) were the first to demonstrate, simultaneously, structural data and velocity data in a LCI experiment. They used the power spectrum of the interference fringe intensity measured with a spectrum analyser. A velocity profile of microspheres suspended in the fluid was measured using the centroid of the Doppler-shifted spectrum at each position in the conduit. The velocity profile in a turbid cylindrical collagen conduit was measured with an uncertainty of 7%.

Fourier transforming the time-dependent interferogram data seems the most straightforward approach to DOCT. Fringe data are defined by the corresponding mutual coherence function. With the analytic signal of the Doppler shifted sample beam,

$$V_S(t) = A(t) \exp[i\phi(t) - i(\omega_0 - \omega_D)t], \quad (5.13)$$

we have

$$\Gamma_{SR}(\tau) = \Gamma_{Source}(\tau) \exp(-i\omega_D\tau), \quad (5.14)$$

where ω_D is the Doppler frequency; $\tau = 2v_S t/c + \tau_0$ has been used setting the time offset $\tau_0 = 0$; v_S is the sample velocity component parallel to the scattering vector with $(v_S/c) \ll 1$. Therefore, the cross-spectral density or power spectrum of the interferogram is

$$W(\omega) = S_{Source}(\omega) * \delta(\omega - \omega_D), \quad (5.15)$$

and the Doppler frequency can easily be estimated, provided ω_D is larger than the width of the source power spectrum $S_{Source}(\omega)$, or in the case of a Gaussian spectrum, $\omega_D > 8 \ln 2/t_C$, where t_C is the coherence time.

Two basic possibilities of Fourier-transforming the interferogram fringe data were presented in 1997:

- (a) Chen *et al* (1997) generated first DOCT images by sequential lateral scans followed by an incremental sample movement in the vertical direction. The Doppler frequency shift at each pixel has been obtained by a fast FT of the interference fringe intensity and calculating the difference between the carrier frequency and the centroid frequency of the power spectrum at that pixel; structural information has been obtained from the same signal by calculating the magnitude of the power spectrum at the carrier frequency. Velocity resolution is dependent on the time available per pixel (equation (5.8)).
- (b) Izatt *et al* (1997) used the magnitude of the coherently demodulated interferometric depth-scan signal to derive the structure and the depth localized Doppler signal by applying

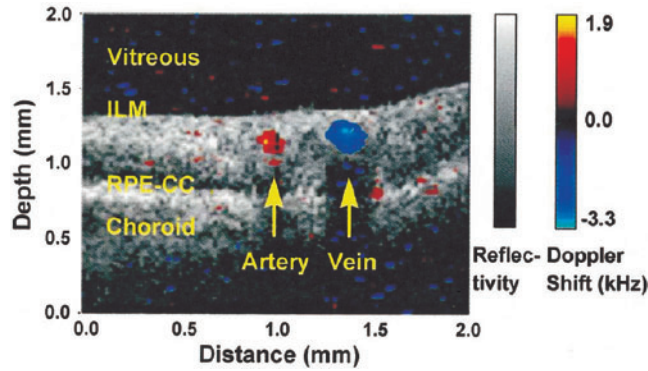


Figure 20. *In vivo* DOCT image of human retina superior to the optic nerve head. Velocity data were thresholded, colour coded and superimposed on the conventional OCT image encoded in grey scale. Reprinted from Yazdanfar *et al* (2000) by permission of the Optical Society of America.

the short-time fast FT (STFT) algorithm. Depth resolution of the velocity estimate is connected to the STFT window length by the Fourier uncertainty relation. Hence, velocity resolution and depth resolution are coupled. Figure 20 presents an example obtained by the so-called ‘colour DOCT technique’ where the detected velocity is colour coded to indicate the magnitude and the direction of flow. Such imaging can be used for studying the pathogenesis of ocular diseases. In contrast to angiography, DOCT is entirely non-invasive.

Several further developments of these techniques have been presented in the subsequent years. For example, Ren *et al* (2002) have shown that under certain conditions the two extreme Doppler shifts caused by the two optical rays at the two outer boundaries of the probe beam can be used to determine flow velocity without precise determination of the flow direction; this technique can extend the unambiguous detection range of DOCT by factors of 10–20. A technique, which extends the physiological relevance of DOCT to higher velocities such as those that occur in blood flow through atherosclerotic lesions, has been described by van Leeuwen *et al* (1999).

5.2.2. Sequential scan processing. The most severe limitation of the fringe data techniques is their limited velocity sensitivity. One technique to overcome this limitation is phase resolved DOCT using sequential depth-scans. This technique also decouples velocity resolution from spatial resolution. Corresponding techniques have been developed by Zhao *et al* (2000) and by Yazdanfar *et al* (2001). The Doppler shift is determined from the phase change of the sample beam between sequential depth-scans at the same location or even between sequential frame scans:

$$\omega_D \approx \frac{\Delta\phi}{T}, \quad (5.16)$$

where $\Delta\phi$ is the measured phase change, and T the time interval between successive depth-scans or frames at the same location, respectively. The phase difference $\Delta\phi$ between two sequential depth-scans (j) and ($j + 1$) is obtained from the complex coherence functions

$$\Delta\phi = \arg[\Gamma_j(\tau)] - \arg[\Gamma_{j+1}(\tau)]. \quad (5.17)$$

As sequential depth-scan signals at the same location are compared, speckle modulations cancel each other and speckle noise is reduced in the velocity image.

Signal processing across sequential scans can be performed either with the complex mutual coherence function $\Gamma(\tau)$ obtained by on-line phase-sensitive demodulation of the photodetector current (Izatt *et al* 1997) or, as described by Zhao *et al* (2000), using the complex coherence function, determined from the photodetector LCI signal by analytic continuation according to equation (1.10). Recently, an optical implementation of the HT has been described, enabling real-time images of *in vivo* blood flow in human skin (Zhao *et al* 2002).

Correlation processing is another technique to increase velocity sensitivity (Yazdanfar *et al* 2001): this technique performs the correlation integral on sequential depth-scan signals m and $m + 1$:

$$\langle \tilde{i}_m^*(t) \tilde{i}_{m+1}(t + T) \rangle, \quad (5.18)$$

$\tilde{i}_m(t)$ is the complex signal obtained by phase sensitive demodulation of the detector current. The local Doppler frequency is obtained from the change in the phase of the cross-correlation:

$$f_D = \frac{1}{2\pi} \frac{(d/d\tau)[\langle \tilde{i}_m^*(t) \tilde{i}_{m+1}(t + T) \rangle]_{\tau=0}}{\langle \tilde{i}_m^*(t) \tilde{i}_{m+1}(t + T) \rangle_{\tau=0}}. \quad (5.19)$$

Phase sensitive sequential scan processing techniques yield sensitivities in the $10 \mu\text{m s}^{-1}$ -range.

5.2.3. Fourier-domain DOCT. In Fourier-domain OCT, instead of scanning the depth with the help of a delay line, the light scattered back by the whole sample depth together with the interferometric reference beam, is dispersed by a spectrometer on an array-detector. Depth information is spread over the whole spectrometer signal. The local sample structure is obtained by Fourier-transforming the spectrometer signal. Hence, the local Doppler frequency shift at z_0 can be obtained from the phase change $\Delta\Phi_F(z_0, t)$ of the corresponding local scattering potential:

$$\omega_D(z_0, t) = \left. \frac{\Delta\Phi_F(z, t)}{\Delta t} \right|_{z_0}. \quad (5.20)$$

The phase of the scattering potential is obtained from the spectral intensity $I_{SR}(K)$ at the interferometer exit with equation (4.16):

$$\Phi_F(z, t) = \tan^{-1} \frac{\text{Im}\{\text{FT}[I_{SR}(K, t) - I_S(K, t) - I_R(K, t)]\}}{\text{Re}\{\text{FT}[I_{SR}(K, t) - I_S(K, t) - I_R(K, t)]\}} \quad (5.21)$$

and the phase difference between sequential depth-scans yields the depth-dependent Doppler frequency:

$$f_D(z, t) = \frac{1}{2\pi} \frac{\Phi_{F,m+1}(z, t) - \Phi_{F,m}(z, t)}{T}, \quad (5.22)$$

where m is the depth-scan number and T the time interval between successive depth-scans. Hence, the depth distribution of the Doppler frequency can be obtained from two spectral records of the scattered spectrum.

An important advantage of Fourier-domain DOCT is the high phase stability and speed of Fourier-domain set-ups. Leitgeb *et al* (2002) have shown that longitudinal velocity components from $\sim 10 \mu\text{m s}^{-1}$ to 2 mm s^{-1} can be measured at a rate of 10^4 depth-scans per second without readjusting the instrumental parameters.

5.2.4. Hardware solutions. An urgent issue in DOCT is the bandwidth problem. To optimize the SNR in PCI and OCT the optimal detection electronics bandwidth is chosen as approximately twice the frequency of the photocurrent signal due to the heterodyne modulation

(Swanson *et al* 1992). In DOCT, however, the detection bandwidth must be chosen to match the much wider width corresponding to the range of velocities with the consequence of degrading the SNR. To overcome that problem, a frequency tracking band-pass filter based on a modified phase-lock loop has been suggested by Zvyagin *et al* (2000).

Speed of data processing is another important issue in DOCT. Zhao *et al* (2002) have replaced the time-consuming digital HT by an optical HT using polarization optics. In another approach, hardware-implemented auto-correlation enabled a frame rate of 8 s^{-1} with 480 depth-scans per image and 800 samples per depth-scan (Westphal *et al* 2002).

5.3. Wavelength-dependent OCT

Wavelength-dependent images are a basic source of information in various fields of science and technology. Quantitative tissue spectroscopy is a diagnostic tool in biomedicine with many potential and a few implemented applications like foetal brain oxygenation measurement. One problem, e.g. is that Beer's law needs the penetration path length of light. In particular, since light penetration in tissue is low (see section 2.3), backscattering geometry must be used in the majority of cases. This geometry, however, leaves the penetration depth of the photons largely unknown; no quantitative measurements are possible. Furthermore, no real tissue is homogeneous. All techniques based on mean value assumptions, therefore, are questionable. Here, LCI and OCT yield the solution. These techniques provide the missing penetration depths, even in highly scattering tissues.

In principle, optical tissue spectroscopy can be used to identify absorbing substances like oxygenated and deoxygenated haemoglobin, cytochrome aa3, NADH, lipids, melanin and other tissue chromophores, and thus enable functional studies. Tissue oxygenation is a direct indicator of tissue haemodynamics and metabolism (Jobsis 1977) and, e.g. is closely related to eye diseases such as diabetic retinopathy and glaucoma.

Optical refractometry is a technique for diagnosing various solutions on the basis of the refractive index. It is used to determine the dissolved solids content of fruits, grasses and vegetables during all stages of growth, and salinity refractometry is used to monitor water quality parameters and to measure the refractive index of process fluids. Refractometry is also an established clinical method to determine the serum or blood protein concentration. Recently, a non-invasive blood glucose monitoring technique based on the mismatch of the refractive index of the extracellular fluid and cellular components has been described (Esenaliev *et al* 2001).

LCI and, therefore, OCT too allow the implementation of quantitative tissue spectroscopy and refractometry. Any sample in a low-coherence interferometer introduces a frequency-dependent phase $\Phi_{\text{Disp}}(\nu)$ to the sample beam; its amplitude is determined by the square root of a frequency-dependent reflectivity $R(\nu)$. Hence, the cross-spectral density of sample and reference beam is $W_{\text{SR}}(\nu) = S_{\text{Source}}(\nu)H(\nu)$ (equation (4.5)), where $S_{\text{Source}}(\nu)$ is the spectral density of the source light, and $H(\nu)$ the sample transfer function.

The more familiar FT spectrometry (FTS) technique has already been used in tissue diagnostics (Ozaki and Kaneuchi 1989). Note, however, that in FTS the sample is positioned outside the interferometer, and is transmitted by both interferometer beams. The result, therefore, is an auto-correlation of the two beams that lacks any phase information. By inserting the sample into only one arm of the interferometer the cross-correlation interferogram of incident and transmitted light, and therefore, the complete sample transfer function $H(\nu)$ is obtained (Fuji *et al* 1997).

In a backscattering geometry amplitude and phase changes of the sample transfer function $H(\nu)$ are depth dependent,

$$H(\nu; z) = \sqrt{R(\nu; z)} \exp[i\Phi_{\text{Disp}}(\nu; z)], \quad (5.23)$$

with an amplitude spectrum (Schmitt *et al* 1998c)

$$R(\nu; z) = \frac{\sigma_b(\nu; z)}{z^2} \exp \left[-2 \int_0^z \mu_a(\nu; z') dz' \right], \quad (5.24)$$

where $\sigma_b(\nu; z)$ is the spectral backscatter cross section of the sample and $\mu_a(\nu; z)$ the mean spectral attenuation coefficient between the sample surface (assumed at $z = 0$) and the depth in the sample z . The phase spectrum is

$$\Phi_{\text{Disp}}(\nu; z) = 2 \frac{\omega}{c} \int_0^z [n(\nu; z') - 1] dz' = 2 \int_0^z [k(\nu) - \bar{k}] dz', \quad (5.25)$$

where $n(\nu; z)$ is the sample refractive index, $\bar{k} = (2\pi/\bar{\lambda})$. Both the amplitude spectrum $\sqrt{R(\nu; z)}$ and phase spectrum $\Phi_{\text{Disp}}(\nu; z)$ of the sample response function can be recovered from a FT of the interferogram (Fuji *et al* 1997, Hellmuth and Welle 1998).

The measurement and imaging of the spectral sample reflectance $R(\nu; z)$ is the subject of spectrometric OCT techniques (sections 5.3.1 through 5.3.4) whereas measurement and imaging of the phase spectrum $\Phi_{\text{Disp}}(\nu; z)$ is the subject of spectral refractometry OCT techniques (section 5.3.5). Whereas both the absorption coefficient of most tissues (at the red end of the visible spectrum of the order of 0.04 mm^{-1}) and the scattering coefficient (of the order of some 10 mm^{-1}) exhibit strong wavelength and tissue dependences, the refractive index varies very little on a macroscopic scale and varies from 1.33 for water to 1.40 for most tissues and 1.55 for fat.

5.3.1. Spectrometric OCT. Spectrometric OCT (SOCT) is based on the FT of the analytic depth-scan interferogram signal $\Gamma_{\text{SR}}(\tau)$ or the cross-power spectrum $W_{\text{SR}}(\nu)$ of sample and reference waves. The cross-power spectrum, however, is not equal to the power spectrum of the light backscattered by the sample. For example, $W_{\text{SR}}(\nu) \leq \sqrt{S_{\text{S}}(\nu)S_{\text{R}}(\nu)}$, where $S_{\text{S}}(\nu)$ and $S_{\text{R}}(\nu)$ are the spectral intensities of the reference light and sample light, respectively. Furthermore, the spectral intensity of the light at the interferometer exit is not just the sum of the spectral intensities of the two interfering beams but depends on the mutual spectral degree of coherence of the spectral light components backscattered by the sample and also on the spectral degree of coherence with respect to the light reflected at the reference mirror (Mandel and Wolf 1995).

In a preliminary study, Kulkarni and Izatt (1996) used the sample transfer function

$$H(\nu) = \frac{W_{\text{SR}}(\nu)}{S_{\text{Source}}(\nu)}, \quad (5.26)$$

to calculate the spectral characteristics of the interface Fresnel reflections of a sample. They observed that, for Mie scatterers, the average of $|H(\nu)|^2$ correlates with the backscatter power spectrum.

Morgner *et al* (2000) presented the first broadband time-domain SOCT technique. These authors used state-of-the-art femtosecond Ti : Al₂O₃ lasers to obtain spectroscopic information in tissue over a bandwidth from 650 to 1000 nm. Since narrow depth windows give good depth resolution, but poor spectral resolution, whereas wide depth windows give good spectral resolution, but poor depth resolution, the spectrometric characteristics of the sample were determined from a Morlet wavelet transform, WT, of the interferogram:

$$W_{\text{SR}}(\Omega, \tau) = WT\{G_{\text{SR}}(t + \tau)\} = \left| \int G_{\text{SR}}(t + \tau) \exp \left[-\left(\frac{t}{t_0} \right)^2 \right] \exp(i\Omega t) dt \right|^2. \quad (5.27)$$

This transform reduces windowing effects and yields an entire spectrum at each image point. To display this four-dimensional information (transverse and depth coordinates x and τ ,

backscattering intensity, and spectral data) in false colours, the spectral centre of mass has been mapped into hue, while keeping the luminance constant, and mapping the backscattered intensity into saturation.

It must also be kept in mind that we see band-pass components of the object structure illuminated by light that has been attenuated by wavelength-dependent absorption and scattering in the tissue in front of it. Hence, absorption and scattering of deep structures is convolved with properties of the intervening structures. In a sample with strong selective absorption another problem may occur with spectrally distorted sample beams. Since the sample spectrum is determined by Fourier transforming the (depth) interferogram, the Fourier uncertainty relation connects spectral resolution $\Delta\nu$ with depth resolution Δz : $\Delta z \Delta\nu \geq (c/4\pi)$. If, e.g. a spectral resolution of $\Delta\nu/N$ is needed to identify a chemical component of the sample, where $\Delta\nu$ is the spectral width of the source light, the corresponding depth resolution Δz is degraded by the same factor N —it becomes $N\Delta z$.

5.3.2. Fourier-domain SOCT. Leitgeb *et al* (2000) describe the adaptation of Fourier-domain OCT spectroscopic measurements to SOCT. In Fourier-domain OCT the light exiting the interferometer is dispersed by a spectrometer to display its spectral distribution on an array-detector. The detector signal represents the wavelength-dependent scattered field $A_S(K)$, from which the object structure is obtained by a FT (see equation (4.15)). In spectral Fourier-domain OCT a frequency window $w(\Delta K; K_n)$ of width ΔK centred at wave number K_n is mathematically shifted along the spectrum $A_S(K)$. The spectral data within each frequency window are Fourier transformed:

$$\text{FT}\{A_S(K) \cdot w(K_n; \Delta K)\} = F_O(K_n; z) * \hat{w}(\Delta K; z) \exp(iK_n z). \quad (5.28)$$

The object structure is thus reconstructed using a windowed FT. $\hat{w}(\Delta K; z)$ is the Fourier-transformed window function. The central wave number K_n of each window represents a monochromatic wavelength; its width ΔK determines the spectral resolution. Thus the Fourier-domain SOCT image is constructed step by step from monochromatic components. Each component can be encoded by a (false) colour and thus a spectroscopic false-colour image results. Depth resolution is determined by $\Delta z = 8 \ln 2 / \Delta K$ (see section 2.6.1). Experimental SOCT images of a glass filter plate have been presented by Leitgeb *et al* (2000).

5.3.3. Differential absorption OCT. Schmitt *et al* (1998c) have presented a technique to generate OCT images of local concentrations of absorbing substances. A pair of light-emitting diodes (1) and (2) was used to illuminate the OCT interferometer; ideally, one diode emitting in the vibrational band of the chemical compound of interest and the other just outside this band. The operating principle is similar to differential-absorption lidar techniques (Sasano 1988): the integrated differential attenuation within a layer of the sample is obtained in terms of the logarithmic ratio of the intensities I_1 and I_2 of the two beams (wavelengths λ_1 and λ_2 , respectively) measured at the top (z_0) and bottom (z) of the layer:

$$2 \int_{z_0}^z [\mu_{a2}(z') - \mu_{a1}(z')] dz' = \ln \left[\frac{I_1(z)}{I_1(z_0)} \frac{I_2(z_0)}{I_2(z)} \right]. \quad (5.29)$$

Since the interferometer is illuminated by two mutually incoherent broadband light sources, the total power spectrum in the interferometer equals the sum of the two power spectra. From equation (4.5) the power spectrum of the interferogram is the source power spectrum multiplied by the sample transfer function $H(\nu)$:

$$S_S(\nu) = [S_{\text{Source1}}(\nu) + S_{\text{Source2}}(\nu)]H(\nu). \quad (5.30)$$

Hence, the power spectra can be used to estimate the depth-dependent intensities. This is eased by the fact that the two wavelengths generate different carrier frequencies. Schmitt *et al* (1998c) report on *in vitro* experiments. The thinnest layer of water that could be measured was approximately $50\ \mu\text{m}$ thick. This technique can be used to generate differential absorption OCT images of any substance with sufficiently different absorption coefficients.

5.3.4. Coherence spectrometry. Watanabe and Itoh (2000) describe two spectrometric OCT techniques—one is based on parallel OCT with additional band-pass filtering, whereas the second one is based on spectral interferometry OCT with additional sample movement.

The parallel OCT spectrometric technique uses so-called spectrotomograms obtained with a set-up similar to that depicted in figure 14, using a CCD camera as detector and moving the sample in the depth direction. Spectrotomograms are obtained by filtering the depth-scan interferograms with a series $n = 1, 2, \dots, N$ of band-pass filters with filter transfer function $w_n(\nu)$. The spectrotomograms can be expressed as

$$\Gamma_n(z) = \Gamma_{\text{SR}}(z) \otimes \hat{w}_n(z), \quad (5.31)$$

where $\hat{w}_n(z)$ is the response function of the filter. The spectral properties of the sample are thus extracted by a series of filters with different central wavelengths. The authors discuss the application of that technique to determine the refractive index and absorption coefficient on a multilayered model and demonstrate measurements on a multilayered sample made from a red Cellophane sheet sandwiched between two colourless silicone layers.

The spectral interferometry OCT based technique is called dispersive coherence spectrometry; it uses a modified spectral interferometric OCT set-up corresponding to that described by Zuluaga and Richards-Kortum (1999). Watanabe and Itoh (2000) use a prism spectrometer, illuminate the sample by a line focus of a cylindrical lens and move the sample along the depth direction (see figure 21).

Whereas spectral interferometry or spectral radar techniques obtain depth information without moving the sample, in the dispersive coherence spectrometry technique the

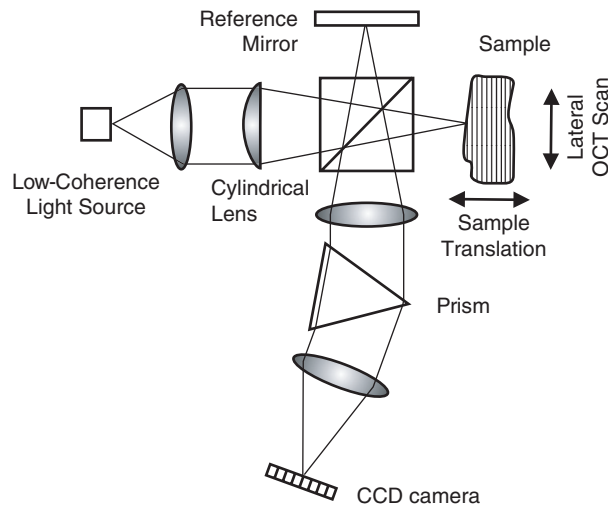


Figure 21. Dispersive coherence spectrometric set-up. Translating the sample along the optical axis provides depth resolved spectrally decomposed two-dimensional interferograms at the CCD camera.

sample is translated. This provides a series of depth located spectral interferograms from which depth and spectral information is extracted. For example, the spectrally decomposed interferograms are integrated according to a series of specially designed spectral filters to synthesize the complete interferogram.

5.3.5. Refractometric OCT. As already mentioned, interference refractometry is a standard analytical laboratory technique; dispersion data are important in environmental science and in diagnostic medicine. Quantitative dispersion data are important in predicting the propagation of light through ocular media, in photorefractive surgery and in tissue diagnostics. Refractive index variations cause phase variations in the sample beam. Hitzenberger and Fercher (1999) and Sticker *et al* (2001) have presented a differential phase-contrast OCT (DP-OCT) technique. This technique is an extension of the more well known Nomarski differential interference-contrast microscopy technique towards quantitative three-dimensional imaging.

DP-OCT probes the sample simultaneously with two transversally shifted probe beams. Figure 22 depicts the optical scheme. A nonpolarizing beam splitter provides reference and probe beam polarized at 45° as generated by a linear polarizer at the light source. The probe beam is split once again by a Wollaston prism and collimated by the sample lens. Two orthogonally oriented beams separated by Δx illuminate the sample. The backscattered beams are combined by the Wollaston prism and separated by the polarizing beam splitter in the detection arm. From the photodetector signals two interferograms $G_1(z)$ and $G_2(z)$ are obtained. The phases of the two interferograms are obtained from the corresponding complex interferograms $\Gamma_{1,2}(z) = \frac{1}{2}G_{1,2}(z) + (i/2)\text{HT}\{G_{1,2}(z)\}$ using HTs. Hence, three images are obtained: two intensity images, $|\Gamma_1(z)|$ and $|\Gamma_2(z)|$, and a phase difference image, $\arg[\Gamma_2(z) - \Gamma_1(z)]$. Experiments have shown that phase differences corresponding to path differences down to the nanometre range can be obtained in transparent media as well as through scattering layers (Sticker *et al* 2001).

Since DP-OCT detects phase contrast in the direction of beam separation, it detects phase gradients caused by transversal variations of the refractive index and/or the phase change on reflection at interfaces. An alternative technique has been presented by Sticker *et al* (2002).

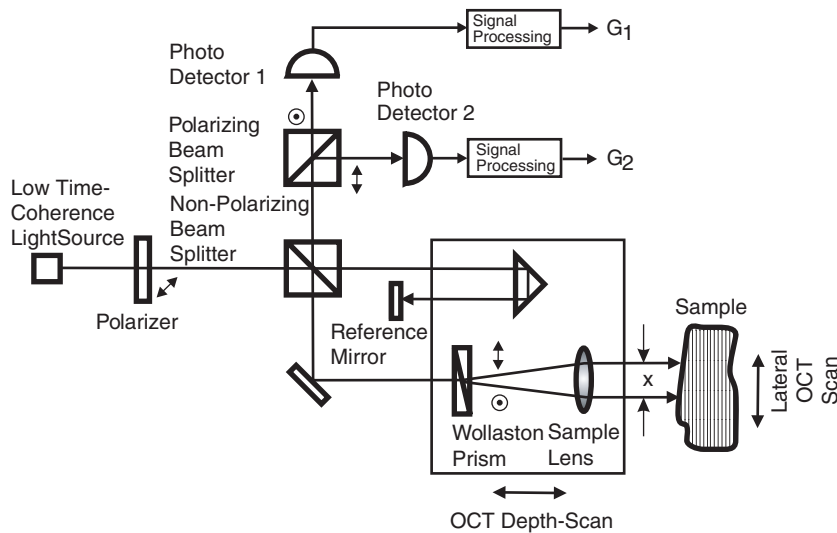


Figure 22. Differential phase-contrast OCT set-up. $G_{1,2}$: interferograms.

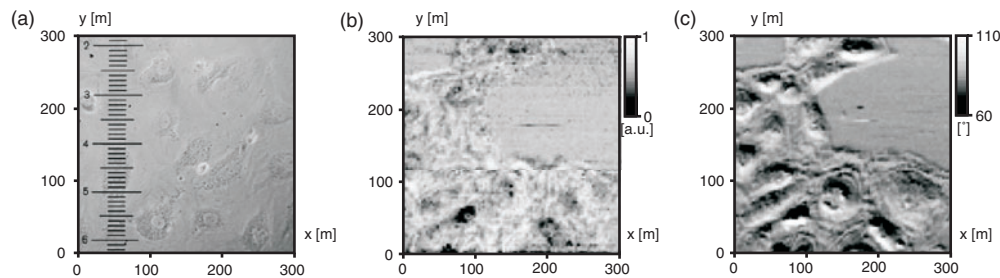


Figure 23. Single cell layer of endothelial cells. (a) Zernike phase contrast micrograph. (b) Intensity based *en-face* OCT image; sample region different from (a). (c) Phase-difference based *en-face* OCT image; same sample region as (b). Reprinted from Sticker *et al* (2002) by permission of the Optical Society of America.

In this technique the two probe beams are coaxial but have different focus diameters. Phase differences that occur between the narrow central probe beam and its immediate neighbourhood are thus measured independent of direction. Figure 23 shows an example. Figure 23(a) is a conventional Zernike phase-contrast microscopic image of human microvascular endothelial cells. Nucleoli, nuclei and organelles are visible. The intensity-based OCT image figure 23(b) clearly differentiates between areas where cells are grown upon the glass surface from areas where no cells are present but no single cells or inner structures are identified. In contrast, the PC-OCT image figure 23(c) clearly delineates the cell boundaries and internal cell structures. The OCT images were obtained with a superluminescent diode ($\bar{\lambda} = 820$, $\Delta\lambda = 22$ nm; FWHM diameters of the probe beam foci were 2.6 and $7.2 \mu\text{m}$, 100×100 depth-scans, lateral separation $3 \mu\text{m}$). The main advantage of the OCT technique here is its larger depth penetration in scattering media as compared, for example, to confocal microscopy.

6. Applications of OCT

OCT was initially applied for imaging in ophthalmology (Swanson *et al* 1993, Fercher *et al* 1993a). Advances in OCT technology have made it possible to use OCT in a wide variety of applications. Medical applications are still dominating (Fujimoto *et al* 1995, Fujimoto *et al* 1999a,b, Bouma and Tearney 2002a). Besides the closely related surface topography techniques, only a few non-medical OCT applications have been investigated so far. Specific advantages of OCT compared with alternative optical techniques are that its

- depth resolution is independent of the sample beam aperture, and that
- the coherence gate can substantially improve the probing depth in scattering media.

The advantages of OCT compared to non-optical imaging modalities are its

- high depth and transversal resolution,
- contact-free and non-invasive operation, and the possibility to create,
- function dependent image contrast. Related contrasting techniques are based on Doppler frequency shift, polarization and wavelength-dependent backscattering.

The main disadvantage of OCT compared to alternative imaging modalities in medicine is its limited penetration depth in scattering media.

In this section we shall only describe the state of some important OCT applications. A more comprehensive presentation can be found in Bouma and Tearney (2002a).

6.1. OCT in ophthalmology

Ophthalmology is still the dominating field of biomedical OCT. The most important reason for that is the high transmittance of ocular media. Another reason is the interferometric sensitivity and precision of OCT which fits quite well the near-optical quality of many ophthalmological structures. Still another reason is the independence of depth resolution from sample beam aperture which enables high sensitivity layer structure recording at the fundus of the eye (Puliafito *et al* 1995). Hence, OCT has already become a routine tool for the investigation in particular, of the posterior part of the eye. There has been less attention to the anterior segment of the eye though OCT can be helpful to image and measure details of corneal pathologies and structural changes of the chamber angle and iris (Hoerauf *et al* 2002). Recently, Bagayev *et al* (2002) have addressed corneal laser ablation monitoring by OCT.

Despite the promising and clinically valuable results of recent OCT studies, however, the axial resolution and performance of standard clinical ophthalmic OCT technology can be significantly improved. Many of the early pathological changes associated with disease are still below the resolution limit of standard OCT. Intraretinal structures, such as the ganglion cell layer, the photoreceptor layer, and the RPE, are often involved in early stages of ocular diseases, but cannot be resolved with standard OCT. Therefore, the potential of new light sources for OCT resolution enhancement is being investigated by several research groups.

Recently, ultra-high-resolution OCT imaging employing a laboratory prototype femtosecond Titanium–sapphire laser light source has been demonstrated. An axial resolution of 1–3 μm in non-transparent and transparent tissue has been achieved, enabling unprecedented *in vivo* imaging of intraretinal sub-cellular structures (Drexler *et al* 1999, 2000). The availability of this technology for clinical research and patient care will depend mainly on the availability of suitable sources for ultra-broad-bandwidth light. A corresponding compact, reliable, user-friendly third generation ultra-high-resolution ophthalmological OCT system based on state-of-the-art laser technology, has been developed just recently (Drexler *et al* 2002).

Figure 24 shows ultra-high-resolution OCT images of a 63-year-old woman with age-related macular degeneration with occult classic neovascularization and serous detachment of the RPE on her right eye. Figures 24(a)–(c) show horizontal cross-sectional ultra-high-resolution OCT images through the foveal region. Figure 24(d) indicates corresponding scan positions on an infrared photo, figures 24(e) and (f), early and late fluorescein angiography photos and figure 24(g) an ICG fundus photo. The ultra-high-resolution OCT images indicate normal appearance of the NFL, ganglion cell layer (GCL), inner and outer plexiform layers, as well as of the inner nuclear layer in all three sections (see figure 9). The external limiting membrane (ELM) is clearly visualized and displaced, indicating good inner segment photoreceptor condition. The outer segment of the photoreceptors, however, is significantly compromised and detached in the foveola regions, overlapping with the temporal region of RPE detachment corresponding with fundus angiographic (FA) and indocyanine-green (ICG) fundus photo appearances (e)–(g). Retinal thickening as well as loss of normal foveal pit appearance are clearly visualized.

As shown in figure 24 ultra-high-resolution ophthalmic OCT enables unprecedented visualization of all major intraretinal layers and the ability to assess changes of retinal morphology associated with retinal pathologies, especially in the complex of the inner and outer segments of photoreceptors, the ELM, and the RPE. Hence, it has the potential to become an important and powerful adjunct to standard ophthalmic diagnostic methods and to contribute to a better understanding of ocular pathogenesis.

6.2. Other medical fields: OCT biopsy and functional OCT

Excisional biopsy imposes problems like the risk of cancer cell spreading, infection and haemorrhage. Optical biopsy promises to assess tissue and cell function and morphology *in situ*. OCT offers properties like high resolution, high penetration depth, and a potential for functional imaging considered as prerequisites for optical biopsy. Standard OCT can clarify the relevant architectural tissue morphology (Fujimoto *et al* 2000). Many diseases, including cancer in its early stages, require higher resolution for accurate diagnosis (Bouma and Tearney 2002b). Ultra-high resolution OCT (Drexler *et al* 1999), therefore, is an important step towards such optical biopsy (Fujimoto *et al* 1995). Below, we mention a few examples of high-resolution and functional OCT.

6.2.1. High-resolution OCT in gastroenterology and dermatology. Imaging of the gastrointestinal (GI) tract is a first example for the need of increased resolution in OCT. Gastroenterological OCT has been initiated by a study performed by Izatt *et al* (1996), who showed that OCT and OCM can delineate sites like internal histological-level tissue microstructure in bulk GI tissue samples. Sergeev *et al* (1997) demonstrated that (endoscopic) OCT ($\bar{\lambda} = 830 \text{ nm}$, $l_C = 10 \mu\text{m}$, $P_{\text{Source}} = 1.5 \text{ mW}$) is a promising technique for early diagnosis of tumours. Similarly, Tearney *et al* (1997a) showed that endoscopic OCT ($\bar{\lambda} = 1300 \text{ nm}$, $l_C = 15 \mu\text{m}$, $P_{\text{Probe}} = 150 \mu\text{W}$) provides information on tissue microstructure that otherwise could only be obtained with conventional excisional biopsy. For example, Rollins *et al* (1999) showed that endoscopic OCT imaging ($\bar{\lambda} = 1310 \text{ nm}$, $l_C = 11 \mu\text{m}$, $P_{\text{Source}} = 22 \text{ mW}$) clearly delineates the substructure of the mucosa and submucosa in GI organs and depicts structures such as glands, blood vessels, pits, villi and crypts. Sivak *et al* (2000) have used a 2.4 mm diameter prototype radial scanning OCT probe ($\bar{\lambda} = 1300 \text{ nm}$, $l_C = 11 \mu\text{m}$) inserted through an endoscope. 72 GI sites at the oesophagus, stomach, duodenum and so forth, have been imaged. Excellent high-resolution images were obtained in the oesophagus. In the stomach the images obtained were of lowest quality. Bouma *et al* (2000) performed endoscopic OCT images on 32 oesophagus patients including Barrett's oesophagus. A 2.0 mm diameter longitudinal OCT catheter ($\bar{\lambda} = 1300 \text{ nm}$, $l_C = 10 \mu\text{m}$, $P_{\text{Probe}} = 5 \text{ mW}$) inserted through the access port of an endoscope has been used. Clear delineation of oesophagus layers has been obtained. Barrett's oesophagus was differentiated from normal oesophagus mucosa, oesophageal adenocarcinoma was distinguished from normal oesophagus and Barrett's oesophagus.

Standard OCT provides a resolution of a few micrometres. It does not resolve subcellular structures, but provides the architecture of tissue. Lesions can be assessed in real-time and without any side effects. An example is shown in figure 25 (Jaekle *et al* 2000). Endoscopic OCT images were obtained from a tubular adenoma of the transverse colon. That tissue exhibits a stratified architecture along with some dark round areas corresponding to expanded adenomatous glands.

Figure 25 demonstrates an important step in cancer diagnosis using OCT based on architectural tissue properties. It shows, like the above mentioned studies, that standard OCT resolves architectural tissue properties that might be useful as tumour screening parameters. In a related (urologic) study Pan *et al* (2001) presented a first systematic OCT study on tumourigenesis in a standard rat bladder model using a dual-wavelength fibre-optic OCT system ($\bar{\lambda} = 830$ and 1320 nm). These authors showed, that the micro-morphology of porcine bladder such as urothelium, submucosa and muscles are identified by OCT and correlated well with the corresponding histological evaluations. OCT detected oedema, inflammatory infiltrates and submucosal blood congestion as well as the abnormal growth of urothelium. Hence,

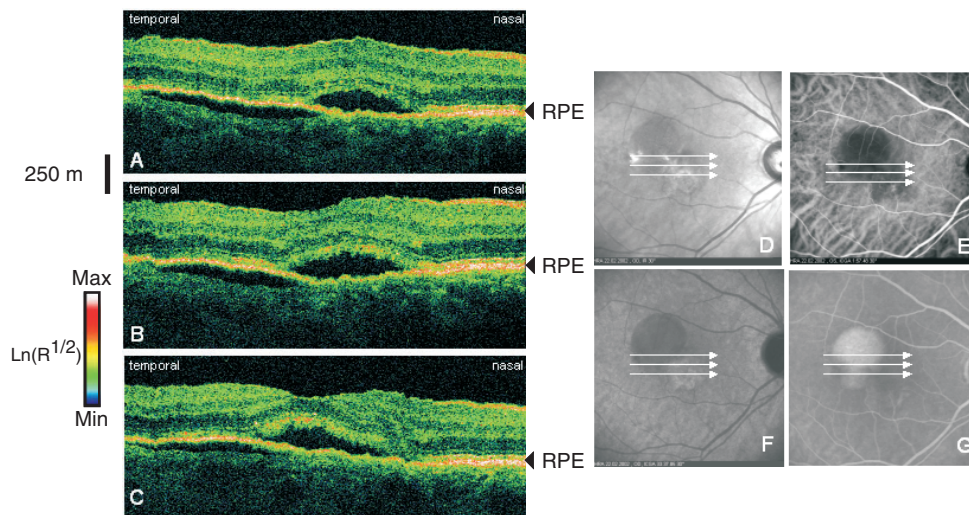


Figure 24. Patient with age-related macular degeneration with occult classic neovascularization and serous detachment of the RPE. (a)–(c) Ultra-high-resolution OCT images through the foveal region (the logarithm of the LCI signal is represented on a false-colour scale shown left of the figures). These pictures clearly delineate the subretinal (above RPE) and RPE detachments (below RPE). (d) Corresponding scan positions on an infrared. (e) and (f) Early and late fluorescein angiography photos. (g) ICG fundus photo.

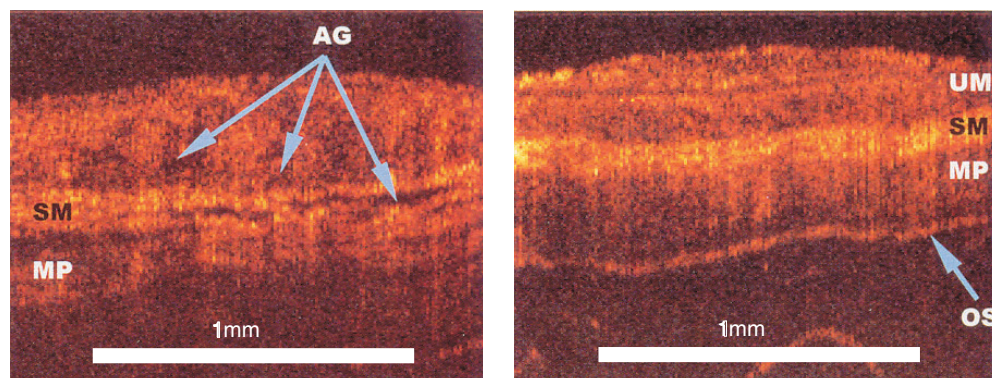


Figure 25. Endoscopic OCT images of: (a) a tubular adenoma and (b) normal transverse colon tissue. OCT endoscopic probe ($\lambda = 1270\text{ nm}$; depth and transversal resolution $l_c = 20\text{ }\mu\text{m}$; $P_{\text{Source}} = 0.5\text{ mW}$) introduced through the biopsy channel of a standard video endoscope. AG = adenomatous gland; MP = *muscularis propria*; SM = submucosa; UM = upper mucosa. Reprinted from Jaekle *et al* (2000) by permission from Georg Thieme Verlag, Stuttgart and New York.

architectural tissue properties might be used as tumour screening parameters identifying pre-malignant tissue states. Standard diagnostic indicators of neoplastic changes, however, are features like accelerated rate of growth, mass growth, local invasion, lack of differentiation, anaplasia and metastasis, which mainly occur on a sub-cellular level. Therefore, the evaluation of sub-cellular structures is absolutely needed for the correct identification and final grading of neoplasias.

A first step to increase OCT resolution close to the sub-cellular level has been achieved using a broad-bandwidth PCF light source. Figure 26 demonstrates near-histologic sub-cellular resolution obtained with a sub-15 fs Titanium:sapphire pumped PCF light source ($\bar{\lambda} = 725$ nm, $\Delta\lambda = 325$ nm, $P_{\text{Source}} = 25$ mW). OCT imaging was performed on human colorectal adenocarcinoma cells HT-29. The figure presents a sequence of six $2\ \mu\text{m}$ spaced, cross-sectional images, each acquired with $0.5\ \mu\text{m}$ axial and $\sim 2\ \mu\text{m}$ transversal resolution, covering an area of $50 \times 50\ \mu\text{m}$, consisting of 500×500 pixels. Histological H&E stained cross section of the same adenocarcinoma HT-29 cells are compared to the OCT results; the correlation of several sub-cellular structures, corresponding to nucleoli or other cellular organelles, can be seen.

A second example where high resolution is a key issue for OCT application is dermatology (Gladkova *et al* 2000). Skin is a highly complex tissue with many inhomogeneities. OCT penetration depth covers the *stratum corneum*, the living epidermis containing mainly keratinocytes, and the *dermis* consisting mainly of a network of collagen and elastin fibres and fibroblasts. Most skin diseases can be diagnosed simply by the naked eye or by epiluminescence microscopy, whereas for cancer diagnosis conventional excisional biopsy is still the gold standard. Clinical studies revealed that standard OCT is of value for diagnosis of some inflammatory and bullous skin diseases (Welzel 2001). It has also been shown that solid skin tumours, e.g. show a homogeneous OCT signal distribution, whereas cystic structures are identifiable by signal-free areas. But cancer diagnosis based on such architectural features is not reliable since the most important diagnostic indicators of neoplastic changes occur on the sub-cellular level. Hence, in dermatology too, high-resolution OCT is a prerequisite for the correct identification and grading of neoplasias.

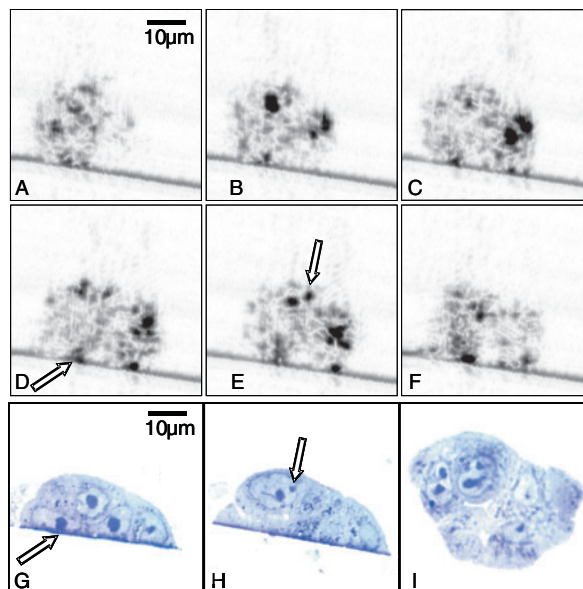


Figure 26. *In vitro* sub-micrometre resolution OCT images of human colorectal adenocarcinoma cells HT-29 with $0.5\ \mu\text{m}$ axial and $\sim 2\ \mu\text{m}$ transverse resolution, over $50 \times 50\ \mu\text{m}$, equally spaced by $2\ \mu\text{m}$ ((a)–(f)). PCF light source ($\bar{\lambda} = 725$ nm; $\Delta\lambda = 325$ nm). Arrows indicate features that may correspond to nucleoli with $\sim 3\text{--}5\ \mu\text{m}$ diameter. Histological sections parallel ((g) and (h)) and perpendicular ((i)) to the OCT imaging direction of typical HT-29 cells. Reprinted from Povazay *et al* (2002) by permission from the Optical Society of America.

6.2.2. Endoscopic OCT in intra-arterial imaging. Depth resolution in OCT is provided by the coherence gate and, therefore, independent of the width of the probing beam. Hence, OCT is predestinated as an endoscopic modality for high-resolution intraluminal imaging of organ systems. Endoscopic and catheter-based procedures are enabling technologies for low-invasive treatments in medicine and, therefore, are growing rapidly. The first endoscopic OCT system has been introduced by Tearney *et al* (1996b, 1997c) for optical biopsy imaging of internal organ systems. First studies of OCT endoscopy of human mucosa in several organ systems indicated a potential of endoscopic OCT for early diagnosis of tumours and precise guiding of excisional biopsy (Sergeev *et al* 1997).

The endoscopic OCT system comprises one arm of the Michelson OCT interferometer. Therefore, fibre-based endoscopy allows the design of extremely narrow endoscopic systems of, e.g. 1 mm in diameter (Tearney *et al* 1996a). Hence, intravascular imaging is possible. Preliminary studies have shown that OCT can detect intramural collections of lipid within the intimal vessel wall (Fujimoto *et al* 1995, Brezinski *et al* 1996). Compared to high frequency (30 MHz) ultrasound, OCT ($\bar{\lambda} = 1300$ nm) yielded superior structural information (Brezinski *et al* 1997). In an experimental study, a high speed catheter-based OCT system of 2.9 F or approximately 1 mm in diameter was used for imaging of the abdominal aorta of New Zealand white rabbits. High contrast was noted between the *media* and the surrounding supportive *adventitia* tissue and fine structural details were visible (Fujimoto *et al* 1999a).

Intracoronary endoscopic OCT imaging on humans has been studied by Bouma and Tearney (2002b). A comparison of OCT ($\bar{\lambda} = 1300$, $\Delta\lambda = 72$ nm, $P_{\text{Source}} = 5$ mW) and histological imaging on diseased cadaveric vessels demonstrated clear differentiation of the *intima*, *media* and *adventitia*. Fibrous plaques appear as homogeneous, high-scattering areas within the vessel wall, whereas calcifications were identified by the presence of high backscattering at the interfaces between calcifications and surrounding tissue. *In vivo* intravascular OCT imaging has been performed in 40 patients. OCT images were obtained with intermittent saline flushes through the guide catheter. Different plaque types were identified including vulnerable plaques needing local treatment. Hence, OCT provides a great potential for improving the understanding of coronary plaque vulnerability and the treatment of acute myocardial infarction.

6.2.3. PS-OCT in dentistry. A field where polarization-dependent backscattering might play an increasingly important role is dental OCT (Colston *et al* 1998). Human teeth consist primarily of enamel, dentin and pulp. The bulk of the tooth is made up of semitransparent dentin, with micrometre-sized dentinal tubules, radiating from the pulp cavity towards the periphery. Near the crown, the outer surface of the tooth is covered by a thin and transparent layer of enamel consisting of microcrystals oriented normally to the surface. Studies of light propagation in dental tissue using PS-OCT revealed strong birefringence in enamel and anisotropic light propagation through dentinal tubules. At $\bar{\lambda} = 856$ nm the group index of refraction for dentin and enamel was 1.50 ± 0.02 and 1.62 ± 0.02 , respectively (Wang *et al* 1999).

Colston *et al* (1998) have presented a fibre-optics based dental OCT system operating at a central wavelength of $\bar{\lambda} = 1300$ nm ($\Delta\lambda = 47$ nm) and a beam power of $P_{\text{Source}} = 15$ mW. Penetration depth varied from 3 mm in hard tissues to 1.5 mm in soft tissue. An optical handpiece was developed for intraoral OCT scans. The sample lens was a gradient refractive index lens with NA = 0.46. The diameter of the sample beam focus was 20 μm ; a SNR of 110 dB was measured. Several structural components of the gingival tissue like the sulcus, the epithelium, and the connective tissue layer were visible in the OCT images. Hard tissue structures identified were enamel, dentin, and dento-enamel junction (see figure 27). Later,

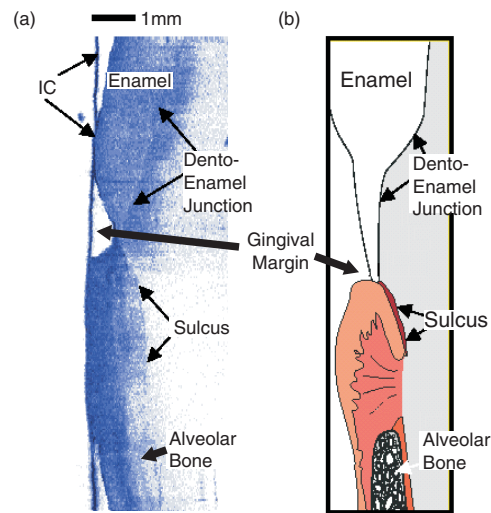


Figure 27. (a) OCT image of anterior tooth. IC = plastic sleeve used for infection control. (b) Cartoon of dental tissues. Adapted from Colston *et al* (1998) by permission from the Optical Society of America.

Amaechi *et al* (2001) used the area under the LCI signal as a measure of the degree of reflectivity of the tissue and showed that this area is related to the amount of mineral loss, and increases with increasing demineralization time. Hence, OCT could possibly be used to quantitatively monitor the mineral changes in a caries lesion.

In the early investigations, birefringence induced artefacts in the enamel OCT image (Colston *et al* 1998). These were eliminated by measuring the polarization state of the returned light. Birefringence detected by PS-OCT, however, has been shown to be useful as a contrast agent indicating pre-carious or carious lesions in both enamel and dentin (Wang *et al* 1999). PS-OCT can provide additional information related to the mineralization status and/or the scattering properties of the dental materials (Baumgartner *et al* 2000).

6.2.4. Spectroscopic OCT in gastroenterology. Spectroscopic OCT (SOCT) combines tissue spectroscopy with high-resolution topographic imaging. This technique is based on broad-bandwidth light sources; spectral information is obtained from the FT of the analytic depth-scan interferogram signal $\Gamma_{SR}(\tau)$ (see section 5.3.1). The basic principles of SOCT have been presented by Morgner *et al* (2000). A first approach to clinical application has been presented by Li *et al* (2000) in a (unblinded) feasibility study to enhance the differentiation of Barrett's oesophagus. Good correlation between high-resolution endoscopic OCT and histologic figures has been obtained. Endoscopic OCT could differentiate normal from Barrett's epithelium in real-time, based on differences in epithelial architecture. Crypt- and gland-like structures, which disrupted the relatively uniform layers of squamous epithelium were readily identified suggesting the ability of OCT for screening applications. In this study, furthermore, spectroscopic OCT imaging has been performed on *ex vivo* specimens. The irregular epithelial morphologies of crypt- and gland-like structures of Barrett's oesophagus showed enhanced long-wavelength scattering. This is, of course, a rather preliminary result. How far spectroscopic features would enhance the OCT potential to grade certain dysplasias still remains to be proved.

6.2.5. DOCT in haemostatic therapy. An important advantage of DOCT as compared to ultrasound techniques is, besides high depth and velocity resolution, its contact-free operation. That enables the measurement of blood flow in subsurface vessels without interference by the pressure exerted by a transducer. Like OCT, of course, the applicability of DOCT is confined to shallow depths in scattering tissue. Therefore, besides ophthalmology (see, e.g. section 5.2) important medical applications are to be found in dermatology, where DOCT has been used to analyse the structure of subsurface dermal blood vessels in port wine stain photocoagulation (Barton *et al* 2001), for *in vivo* monitoring of photodynamic therapy (Milner *et al* 2002) and for recording of cardiac flow dynamics in developmental biology (Boppart *et al* 1997).

In a recent study (colour) DOCT was used to visualize and measure blood flow in subsurface vessels to study haemostatic interventions (Wong *et al* 2002). Measurements were performed on an *in vivo* rat skin model (dorsal flap). The OCT system used a superluminescent diode ($\bar{\lambda} = 1.27 \mu\text{m}$, $\Delta\lambda = 37 \text{ nm}$, $P_{\text{Source}} = 1.2 \text{ mW}$) and a linearly scanning reference arm generating the heterodyne frequency. Demodulating the detector signal at the constant heterodyne frequency yielded the tissue reflectivity. Measuring the mean Doppler frequency shift of the sample beam as a function of depth yielded the velocity estimate within the tissue. Blood flow was significantly reduced after epinephrine injection and became undetectable after local haemostatic interventions like thermal contact coagulation with a heat probe and laser photocoagulation. The response to epinephrine was shown to be only temporary; limited application of heat alone from the heat probe halted blood flow without visually apparent surface injury.

6.3. Non-medical OCT

Low-coherence interferometry has already been used in optical production technology and other technical fields. For example, LCI or ‘interference with white light’ (Hariharan 1985) has been used for many years in industrial metrology, e.g. as position sensor (Li *et al* 1995), for thickness measurement of thin films (Flourney 1972), and for other measurands that can be converted to a displacement (Rao *et al* 1993). Recently, LCI has been proposed as a key technology for high density data storage on multilayer optical discs (Chinn and Swanson 2002).

Dunkers *et al* (1999) analysed the applicability of OCT for nondestructive evaluation of highly scattering polymer-matrix composites to estimate residual porosity, fibre architecture and structural integrity. Using a broad-bandwidth 25 fs mode-locked Cr:forsterite solid-state laser ($\bar{\lambda} = 1.3 \mu\text{m}$, $P_{\text{Source}} = 3\text{--}4 \text{ mW}$) glass reinforced polymer composites could be successfully imaged. High-resolution images with $20 \mu\text{m}$ transverse and $10 \mu\text{m}$ depth resolution were obtained from composite samples. Fibre architecture and voids of glass-reinforced polymer composites have been successfully resolved. Fibre lens effects and interference of backscattered light and surface reflections were identified as the most prominent sources of noise. Compared to ultrasound imaging, OCT provides higher resolution and non-contact operation. A related application of OCT has been described by Bashkansky *et al* (2001). These authors detect the subsurface extent of the Hertzian crack on the surface of a silicon nitride ball to compare it with predictions of crack propagation theories based on principal stresses and on maximum strain energy release.

Nondestructive evaluation of paints and coatings is another promising non-medical OCT application. Xu *et al* (1999) used a free-space optics OCT system (SLD: $\bar{\lambda} = 850 \text{ nm}$, $\Delta\lambda = 20 \text{ nm}$, $P_{\text{Source}} = 8 \text{ mW}$) confocally enhanced by a pinhole and a focusing lens in front of the photodetector. Imaging through a $80 \mu\text{m}$ thick highly scattering polymeric two-component paint layer (corresponding to an equivalent thickness of ten mean free paths) has been demonstrated.

Acknowledgments

Our own contributions to this work are based on projects (P7300-MED, P9781-MED, P10316-MED, P14103-MED, P14218-PSY and Y-159-PAT) financed by the Austrian Fonds zur Förderung der wissenschaftlichen Forschung (FWF), project CRAF-1999-70549 financed by the European Community, project No 7428 supported by the Austrian National Bank, and funded by the Christian Doppler Gesellschaft. We would like to thank K K Bizheva, E Götzinger, B Hermann, R Leitgeb, M Pircher, B Povazay and H Sattmann for communicating their current research results. We also acknowledge the Carl Zeiss Meditec AG help with respect to instruments.

References

- Abouraddy A F, Nasr M B, Saleh B E A, Sergienko A V and Teich M C 2002 *Phys. Rev. A* **65** 053817/1–053817/6
- Amaechi B T, Higham S M, Podoleanu A G, Rogers J A and Jackson D A 2001 *J. Oral. Rehabil.* **28** 1092–3
- Apolonski A, Povazay B, Unterhuber A, Drexler W, Wadsworth W J, Knight J C and Russell P S J 2002 *J. Opt. Soc. Am. B* **19** 2165–70
- Arridge S R and Schweiger M 1997 *Phil. Trans. R. Soc. B* **352** 717–26
- Arutyunov V A and Slobodyan S M 1985 *Instrum. Exp. Tech.* **28** 160–2
- Bagayev S N, Gelikonov V M, Gelikonov G V, Kargapol'tsev E S, Kuranov R V, Razhev A M, Tuchin I V and Zhupikov A A 2002 *J. Biomed. Opt.* **7** 633–42
- Ballif J, Gianotti R, Chavanne Ph, Wälti R and Salathe R P 1997 *Opt. Lett.* **22** 757–9
- Barton J K, Rollins A, Yazdanfar S, Pfefer T J, Westphal V and Izatt J A 2001 *Phys. Med. Biol.* **46** 1665–78
- Bashkansky M, Duncan M D, Goldberg L, Koplow J P and Reintjes J 1998a *Opt. Express.* **3** 305–10
- Bashkansky M, Duncan M D, Reintjes J and Battle P R 1998b *Opt. Photon.* **9** 8138–9
- Bashkansky M and Reintjes J 2000 *Opt. Lett.* **25** 545–7
- Bashkansky M, Lewis D III, Pujari V, Reintjes J and Yu H Y 2001 *NDT E-International* **34** 547–55
- Baumgartner A, Dichtl S, Hitzberger C K, Sattmann H, Robl B, Moritz A, Fercher A F and Sperr W 2000 *Caries. Res.* **34** 59–69
- Baumgartner A, Hitzberger C K, Sattmann H, Drexler W and Fercher A F 1998 *J. Biomed. Opt.* **3** 45–54
- Beaupaire E, Boccaro A C, Lebec M, Blanchot L and Saint-Jalmes H 1998 *Opt. Lett.* **23** 244–6
- Berlien H P and Müller G 1989 *Angewandte Lasermedizin* (Landsberg: Ecomed)
- Bickel W S, Davidson J F, Huffman D R and Kilkson R 1976 *Proc. Natl. Acad. Sci.* **73** 486–90
- Birks T A, Wadsworth W J and Russell P S J 2000 *Opt. Lett.* **25** 1415–17
- Bizheva K K, Siegel A M and Boas D A 1998 *Phys. Rev. E* **58** 7664–7
- Boppart S A, Tearney G J, Bouma B E, Southern J F, Brezinski M F and Fujimoto J G 1997 *Proc. Natl. Acad. Sci.* **94** 4256–61
- Born M and Wolf E 1999 *Principles of Optics* (Cambridge: Cambridge University Press)
- Boulnois J L 1986 *Lasers Med. Sci.* **1** 47–66
- Bouma B E, Tearney G J, Bilinsky I P, Golubovic B and Fujimoto J G 1996 *Opt. Lett.* **21** 1839–41
- Bouma B E, Nelson L E, Tearney G J, Jones D J, Brezinski M E and Fujimoto J G 1998 *J. Biomed. Opt.* **3** 76–9
- Bouma B E and Tearney G J (ed) 2002a *Handbook of Optical Coherence Tomography* (New York: Marcel Dekker)
- Bouma B E and Tearney G J 2002b *Acad. Radiol.* **9** 942–53
- Bouma B E, Tearney G J, Compton C C and Nishioka N S 2000 *Gastrointest. Endoscopy* **51** 467–74
- Bourquin S, Monterosso V, Seitz P and Salathe R P 2000 *Opt. Lett.* **25** 102–4
- Bourquin S, Seitz P and Salathe R P 2001 *El Lett.* **37** 975–6
- Bracewell R N 2000 *The Fourier Transform and its Applications* (Singapore: McGraw-Hill)
- Brezinski M E, Tearney G J, Bouma B E, Izatt J A, Hee M R, Swanson E A, Southern J F and Fujimoto J G 1996 *Circulation* **93** 1206–13
- Brezinski M E, Tearney G J, Weissman N J, Boppart S A, Bouma B E, Hee M R, Weyman A E, Swanson E A, Southern J F and Fujimoto J G 1997 *Heart* **77** 397–403
- Briers J D 2001 *Physiol. Meas.* **22** R35–66
- Brinkmeyer E and Ulrich R 1990 *El Lett.* **26** 413–14
- Brodsky A, Thurber S R and Burgess L W 2000 *J. Opt. Soc. Am. A* **17** 2024–33
- Campbell D J, Krug P A, Falconer I S, Robinson L C and Tait G D 1981 *Appl. Opt.* **20** 335–42
- Chen Z, Milner T E, Dave D and Nelson J S 1997 *Opt. Lett.* **22** 64–6

- Chinn S R and Swanson E A 2002 *Handbook of Optical Coherence Tomography* ed G J Tearney and B E Bouma (New York: Marcel Dekker) pp 385–420
- Chinn S R, Swanson E A and Fujimoto J G 1997 *Opt. Lett.* **22** 340–2
- Chou P C, Haus H A and Brennan J F III 2000 *Opt. Lett.* **25** 524–6
- Clivaz X, Marquis Weible F and Salathe R P 1993 *Proc. SPIE* **2083** 338–46
- Clivaz X, Marquis Weible F, Salathe R P, Novak R P and Gilgen H H 1992 *Opt. Lett.* **17** 4–6
- Coen S, Chau A H L, Leonhardt R, Harvey J D, Knight J C, Wadsworth W J and Russell P S J 2001 *Opt. Lett.* **26** 1356–8
- Colston B W, Sathyam U S, DaSilva L B, Everett M J, Stroeve P and Otis L L 1998 *Opt. Express*. **3** 230–8
- Cummins H Z and Swinney H L 1970 *Prog. Opt.* **8** 134–200
- Danielson B L and Whittenberg C D 1987 *Appl. Opt.* **26** 2836–42
- de Boer J F and Milner T E 2002 *J. Biomed. Opt.* **7** 359–71
- de Boer J F, Milner T E and Nelson J S 1999 *Opt. Lett.* **24** 300–2
- de Boer J F, Milner T E, van Gemert M J C and Nelson J S 1997 *Opt. Lett.* **22** 934–6
- de Boer J F, Saxer C E and Nelson J S 2001 *Appl. Opt.* **40** 5787–90
- de Boer J F, Srinivas S M, Malekafzali A, Chen Z and Nelson J S 1998 *Opt. Express*. **3** 212–18
- De Martino A, Carrara D, Devillon B and Schwartz L 2001 *Proc. SPIE* **4431** 38–42
- Demos S G, Papadopoulos A J, Savage H, Heerdt A S, Schantz S and Alfano R R 1997 *Photochem. Photobiol.* **66** 821–5
- Depeursinge C 2002 *La Tomographie* ed P Grangeat (Paris: Hermes Lavoisier) pp 163–218
- Derickson D J *et al* 1995 *Hewlett-Packard J.* 43–8
- Ding Z, Ren H, Zhao Y, Nelson J S and Chen Z 2002 *Proc. SPIE* **4619** 10–15
- Doppler Ch 1842 *Abh. d K Böhm Ges. d Wiss.* **2** 465–83
- Dreher A W, Reiter K and Weinreb R N 1992 *Appl. Opt.* **31** 3730–5
- Drexler W, Findl O, Menapace R, Kruger A, Wedrich A, Rainer G, Baumgartner A, Hitzenberger C K and Fercher A F 1998 *J. Biomed. Opt.* **3** 55–65
- Drexler W, Morgner U, Ghanta R K, Kärtner F X, Schuman J S and Fujimoto J G 2001 *Nature Med.* **7** 502–7
- Drexler W, Morgner U, Ghanta R K, Schuman J S, Kärtner F X, Hee M R, Ippen E P and Fujimoto J G 2000 *The Shape of Glaucoma* ed H G Lemij and J S Schuiman (The Hague: Kugler Publications) pp 75–104
- Drexler W, Morgner U, Kärtner F X, Pitris C, Boppart S A, Li X D, Ippen E P and Fujimoto J G 1999 *Opt. Lett.* **24** 1221–3
- Drexler W *et al* 2002 *Arch. Ophthalmol. Chic.* submitted
- Dror I, Sandrov A and Kopeika N S 1998 *Appl. Opt.* **37** 6495–9
- Dubois A, Boccara A C and Lebec M 1999 *Opt. Lett.* **24** 309–11
- Dubois A, Vabre L, Boccara A C and Beaurepaire E 2002 *Appl. Opt.* **41** 805–12
- Duck F A, Baker A C and Starritt H C 1998 *Ultrasound in Medicine* (Bristol: Institute of Physics Publishing)
- Ducros M, Marsack J D, Rylander III H G, Thomsen S L and Milner T E 2001 *J. Opt. Soc. Am. A* **18** 2945–56
- Ducros M, Laubscher M, Karamata B, Bourquin S, Lasser T and Salathe R P 2002 *Opt. Commun.* **202** 29–35
- Dunkers J P, Parnas R S, Zimba C G, Peterson R C, Flynn K M, Fujimoto J G and Bouma B E 1999 *Composites* **30A** 139–45
- Durnin J, Miceli J and Eberli J H 1987 *Phys. Rev. Lett.* **58** 1499–501
- Edelstein D C, Romney R B and Scheuermann M 1991 *Rev. Sci. Instrum.* **62** 579–83
- Eickhoff W and Ulrich R 1981 *Appl. Phys. Lett.* **39** 693–5
- Esenaliev R O, Larin K V, Larina I V and Motamedi M 2001 *Opt. Lett.* **26** 992–4
- Everett M J, Schoenenberger K, Colston B W Jr and Da Silva L B 1998 *Opt. Lett.* **23** 228–30
- Fercher A F 1990 Ophthalmic interferometry *Optics in Medicine, Biology and Environmental Research* ed G von Bally and S Khanna (Amsterdam: Elsevier) pp 221–35
- Fercher A F, Hitzenberger C K, Drexler W, Kamp G and Sattmann H 1993a *Am. J. Ophthalmol.* **116** 113–14
- Fercher A F, Hitzenberger C K, Drexler W, Kamp G, Strasser I, Li H C 1993b *Medical Optical Tomography: Functional Imaging and Monitoring* vol IS 11, ed G Müller *et al* (Bellingham: SPIE Press) pp 355–70
- Fercher A F, Hitzenberger C and Juchem M 1991 *J. Mod. Opt.* **38** 1327–33
- Fercher A F, Hitzenberger C K, Kamp G and El Zaiat S Y 1995 *Opt. Commun.* **117** 43–8
- Fercher A F, Leitgeb R, Hitzenberger C K, Sattmann H and Wojtkowski M 1999 *Proc. SPIE* **3564** 173–8
- Fercher A F, Hitzenberger C K, Sticker M, Moreno Barriuso E, Leitgeb R, Drexler W and Sattmann H 2000 *Opt. Commun.* **185** 57–64
- Fercher A F, Hitzenberger C K, Sticker M, Zawadzki R, Karamata B and Lasser T 2001 *Opt. Express* **9** 610–15
- Fercher A F and Roth E 1986 *Proc. SPIE* **658** 48–51
- Flournoy P A, McClure R W and Wyntje G 1972 *Appl. Opt.* **11** 1907–15
- Forsberg F, Healey A J, Leeman S and Jensen J A 1991 *Phys. Med. Biol.* **36** 1539–49

- Fried D, Xie J, Shafi S, Feathersone J D B, Breunig T M and Le C 2002 *J. Biomed. Opt.* **7** 618–27
- Fuji T, Miyata M, Kawato S, Hattori T and Nakatsuka H 1997 *J. Opt. Soc. Am. B* **14** 1074–8
- Fujimoto J G, Brezinski M E, Tearney G J, Boppart S A, Bouma B E, Hee M R, Southern J F and Swanson E A 1995 *Nature Med.* **1** 970–2
- Fujimoto J G, Bouma B, Tearney G J, Boppart S A, Pitris C, Southern J F and Brezinski M E 1998 *Ann. NY Acad. Sci.* **838** 95–107
- Fujimoto J G, Boppart S A, Tearney G J, Bouma B E, Pitris C and Brezinski M E 1999a *Heart* **82** 128–33
- Fujimoto J G, Boppart S A, Pitris C and Brezinski M E 1999b *Japan. J. Laser Med. Surg.* **20** 141–68
- Fujimoto J G, Pitris C, Boppart S A and Brezinski M E 2000 *Neoplasia* **2** 9–25
- Gabor D 1970 *IBM J. Res. Devel.* **14** 509–14
- Gandjbakhche A H, Bonner R F and Nossal R 1992 *J. Stat. Phys.* **69** 35–53
- George N, Christensen C R, Bennett J S and Guenther B D 1976 *J. Opt. Soc. Am.* **66** 1282–90
- Gerrard A and Burch J M 1975 *Introduction to Matrix Methods in Optics* (London: Wiley)
- Gladkova N D *et al* 2000 *Skin Res. Tech.* **6** 6–16
- Golubovic B, Bouma B E, Tearney G J and Fujimoto J G 1997 *Opt. Lett.* **22** 1704–6
- Goodman J W 1965 *Proc. IEEE* **53** 1688–700
- Goodman J W 1976 *J. Opt. Soc. Am.* **66** 1145–50
- Goodman J W 1984 *Laser Speckle and Related Phenomena* ed J C Dainty (Berlin: Springer) pp 9–75
- Goodman J W 1985 *Statistical Optics* (New York: Wiley)
- Gusmeroli V and Martinelli M 1991 *Opt. Lett.* **16** 1358–60
- Haberland U H P, Blazek V and Schmitt H J 1998 *J. Biomed. Opt.* **3** 259–66
- Harde H and Burggraf H 1981 *Opt. Commun.* **38** 211–15
- Hariharan P 1985 *Optical Interferometry* (New York: Academic)
- Hartl I, Li X D, Chudoba C, Ghanta R K, Ko T H, Fujimoto J G, Ranka J K and Windeler R S 2001 *Opt. Lett.* **26** 608–10
- Häusler G and Lindner M W 1998 *J. Biomed. Opt.* **3** 21–31
- He Z and Hotate K 1999 *Opt. Lett.* **24** 1502–4
- Hee M R, Huang D, Swanson E A and Fujimoto J G 1992 *J. Opt. Soc. Am. B* **9** 903–8
- Hellmuth T and Welle M 1998 *J. Biomed. Opt.* **3** 7–11
- Hillegas C W, Tull J X, Goswami D, Strickland D and Warren W S 1994 *Opt. Lett.* **19** 737–9
- Hitzenberger C K 1991 *Invest. Ophthalmol. Vis. Sci.* **32** 616–24
- Hitzenberger C K and Fercher A F 1999 *Opt. Lett.* **24** 622–4
- Hitzenberger C K, Baumgartner A and Fercher A F 1998 *Opt. Commun.* **154** 179–85
- Hitzenberger C K, Baumgartner A, Drexler W and Fercher A F 1999a *J. Biomed. Opt.* **4** 144–51
- Hitzenberger C K, Danner M, Drexler W and Fercher A F 1999b *J. Mod. Opt.* **46** 1763–74
- Hitzenberger C K and Fercher A F 2002 *Handbook of Optical Coherence Tomography* ed G J Tearney and B E Bouma (New York: Marcel Dekker) pp 359–83
- Hitzenberger C K, Goetzinger E, Sticker M, Pircher M and Fercher A F 2001 *Opt. Express* **9** 780–90
- Hodara H 1965 *Proc. IEEE* **53** 696–704
- Hoerauf H and Birngruber R 2002 *Handbook of Optical Coherence Tomography* ed G J Tearney and B E Bouma (New York: Marcel Dekker) pp 487–503
- Huang D *et al* 1991 *Science* **254** 1178–81
- Huard S 1996 *Polarization of Light* (Paris: Wiley)
- Hymans A and Lait M A 1960 *Proc. Inst. Electron. Eng.* **107** 365–72
- Izatt J A, Hee M R, Owen G M, Swanson E A and Fujimoto J G 1994 *Opt. Lett.* **19** 590–2
- Izatt J A, Kulkarni M D, Wang K H, Kobayashi K and Sivak M V 1996 *IEEE J. Select. Top. Quant. Electron.* **2** 1017–28
- Izatt J A, Kulkarni M D, Yazdanfar S, Barton J K and Welch A J 1997 *Opt. Lett.* **22** 1439–41
- Jäckle S *et al* 2000 *Endoscopy* **32** 743–9
- Jiao S and Wang L V 2002 *Opt. Lett.* **27** 101–3
- Jobsis F F 1977 *Science* **198** 1264–7
- Johnson J H, Siefken S L, Schmidt A, Corey R and Saulnier P 1998 *Appl. Opt.* **37** 1913–16
- Kak A C and Slaney M 1988 *Principles of Computerized Tomographic Imaging* (New York: IEEE Press)
- Kaufman H E, Barron B A and McDonald M B 1998 *The Cornea* (Boston: Butterworth-Heinemann)
- Koch T L and Koren U 1990 *J. Lightwave Tech.* **8** 274–93
- Kowalevicz A M, Ko T, Hartl I, Fujimoto J G, Pollnau M and Salathé R P 2002 *Opt. Express* **10** 349–53
- Kulkarni M D and Izatt J A 1996 *OSA Technical Digest* **9** 59–60
- Kulkarni M D, Thomas C W and Izatt J A 1997 *Electron. Lett.* **33** 1365–7

- Kwong K F, Yankelevich D, Chu K C, Heritage J P and Dienes A 1993 *Opt. Lett.* **18** 558–60
- Laubscher M, Ducros M, Karamata B, Lasser T and Salathe R 2002 *Opt. Express*. **10** 429–35
- Leitgeb R, Schmetterer L, Wojtkowski M, Hitzenberger C K, Sticker M and Fercher A F 2002 *Proc. SPIE* **4619** 16–21
- Leitgeb R, Wojtkowski M, Hitzenberger C K, Sticker M, Kowalczyk A and Fercher A F 2000 *Opt. Lett.* **25** 820–2
- Lexer F, Hitzenberger C K, Drexler W, Molebny S, Sattmann H, Sticker M and Fercher A F 1999 *J. Mod. Opt.* **46** 541–53
- Lexer F, Hitzenberger C K, Fercher A F and Kulhavy M 1997 *Appl. Opt.* **36** 6548–53
- Li T, Wang A, Murphy K and Claus R 1995 *Opt. Lett.* **20** 785–7
- Li X D *et al* 2000 *Endoscopy* **32** 921–30
- Li X D, Durduran T, Yodh A G, Chance B and Pattanayak D N 1997 *Opt. Lett.* **22** 573–5
- Lindner M W, Andretzki P, Kiesewetter F and Häusler G 2002 *Handbook of Optical Coherence Tomography* ed G J Tearney and B E Bouma (New York: Marcel Dekker) pp 335–57
- Liu H H, Cheng P H and Wang J P 1993 *Opt. Lett.* **18** 678–80
- Logean E, Schmetterer L F and Riva C E 2000 *Appl. Opt.* **39** 2858–62
- Loudon R 1985 *The Quantum Theory of Light* (Oxford: Clarendon)
- Lu J Y, Cheng J, Li Y and Cameron B D 2002 *Proc. SPIE* **4619** 300–11
- MacDonald R I 1981 *Appl. Opt.* **20** 1840–4
- Mandel L and Wolf E 1995 *Optical Coherence and Quantum Optics* (Cambridge: Cambridge University Press)
- Masters B R 2001 *Selected Papers on Optical Low-Coherence Reflectometry and Tomography* SPIE Milestone Series Vol. MS165 (Bellingham: SPIE)
- Milner T E, Yazdanfar S, Rollins A M, Izatt J A, Lindmo T, Chen Z, Nelson J S and Wang X J 2002 *Handbook of Optical Coherence Tomography* (New York: Marcel Dekker) pp 203–36
- Mishchenko M I and Hovenier J W 1995 *Opt. Lett.* **20** 1356–8
- Morgner U, Drexler W, Kärtner F X, Li X D, Pitris C, Ippen E P and Fujimoto J G 2000 *Opt. Lett.* **25** 111–13
- Morgner U, Kärtner F X, Cho S H, Chen Y, Haus H A, Fujimoto J G and Ippen E P 1999 *Opt. Lett.* **24** 411–13
- Morkel P R, Laming R I and Payne D N 1990 *Electron. Lett.* **26** 96–8
- NTT El Corp 2002 www.nel-world.com
- O'Leary M A, Boas D A, Chance B and Yodh A G 1992 *Phys. Rev. Lett.* **69** 2658–61
- Olsen T 1990 *Acta Ophthalmol. (Copenh)* **67** 141–4
- Otis L L, Everett M J, Sathyam U S and Colston B W Jr 2000 *J. Am. Dent. Assoc.* **131** 511–14
- Ozaki Y and Kaneuchi F 1989 *Appl. Spect.* **43** 723–5
- Pan Y, Lavelle J P, Bastacky S I, Meyers S, Pirtskhalaishvili G, Zeidel M L and Farkas D L 2001 *Med. Phys.* **28** 2432–40
- Pan Y, Birngruber R, Rosperich J and Engelhardt R 1995 *Appl. Opt.* **34** 6564–74
- Parrish J A 1981 *J. Invest. Dermatol.* **77** 45–50
- Pircher M, Götzinger E, Leitgeb R, Fercher A F and Hitzenberger C K 2003 *J. Biomed. Opt.* submitted
- Podoleanu A G 2000 *Appl. Opt.* **39** 173–82
- Podoleanu A G, Dobre G M and Jackson D A 1998 *Opt. Lett.* **23** 147–9
- Podoleanu A G and Jackson D A 1999 *Appl. Opt.* **38** 2116–27
- Podoleanu A G, Rogers J A, Jackson D A and Dunne S 2000 *Opt. Express*. **7** 292–8
- Povazay B *et al* 2002 *Opt. Lett.* **27** 1800–2
- Puliafito C A, Hee M E, Schuman J and Fujimoto J G 1995 *Optical Coherence Tomography of Ocular Disease* (Thorofare: Slack Inc)
- Radon J 1917 *Ber Verh Saechs Akad Wiss Leipzig Math. Phys.* **69** 262–77
- Ranka J K, Windeler R S and Stentz A J 2000 *Opt. Lett.* **25** 25–7
- Rao Y J, Ning Y N and Jackson D A 1993 *Opt. Lett.* **18** 462–4
- Ren H K, Brecke M, Ding Z, Zhao Y, Nelson J N and Chen Z 2002 *Opt. Lett.* **27** 409–11
- Riva C, Ross B and Benedek G B 1972 *Invest. Ophthalmol. Vis. Sci.* **11** 936–44
- Riva C E, Grunwald J E, Sinclair S H and O'Keefe K 1981 *Appl. Opt.* **20** 117–20
- Riza N A and Yaqoob Z 2000 *Proc. SPIE* **4160** 37–42
- Rogers J A, Podoleanu A G, Dobre G, Fitzke F W and Jackson D A 2001 *Opt. Express*. **9** 533–45
- Rogowska J and Brezinski M E 2000 *IEEE Trans. Med. Imaging* **19** 1261–6
- Rollins A M, Kulkarni M D, Yazdanfar S, Ung arunyawee R and Izatt J A 1998 *Opt. Express* **3** 219–29
- Rollins A M and Izatt J A 1999 *Opt. Lett.* **24** 1484–6
- Rollins A M, Ung arunyawee R, Chak A, Wong R C K, Kobayashi K, Sivak M V Jr and Izatt J A 1999 *Opt. Lett.* **24** 1358–60
- Rosen J and Takeda M 2000 *Appl. Opt.* **39** 4107–11
- Roth J E, Kozak J A, Yazdanfar S, Rollins A M and Izatt J A 2001 *Opt. Lett.* **26** 1069–71

- Sala K L, Kenney Wallace G A and Hall G E 1980 *IEEE J. Quant. Electron.* **QE-16** 990–6
- Sasano Y 1988 *Appl. Opt.* **27** 2640–1
- Saxer C E, de Boer J F, Hyle Park B, Zhao Y, Chen Z and Nelson J S 2000 *Opt. Lett.* **25** 1257–355
- Schlueter M 1980 *Opt. Laser Technol.* **12** 93–5
- Schmitt J M 1997 *Phys. Med. Biol.* **42** 1427–39
- Schmitt J M 1998a *J. Biomed. Opt.* **3** 66–75
- Schmitt J M 1998b *Opt. Express*. **3** 121–99
- Schmitt J M and Knüttel A 1997 *J. Opt. Soc. Am. A* **14** 1231–42
- Schmitt J M and Kumar G 1996 *Opt. Lett.* **21** 1310–12
- Schmitt J M and Kumar G 1998a *Appl. Opt.* **37** 2788–97
- Schmitt J M, Lee S L and Yung K M 1997 *Opt. Commun.* **142** 203–7
- Schmitt J M and Xiang S H 1998b *Opt. Lett.* **23** 1060–2
- Schmitt J M, Xiang S H, Yung K M 1998c *J. Opt. Soc. Am. A* **15** 2288–96
- Schmitt J M, Xiang S H and Yung K M 1999 *J. Biomed. Opt.* **4** 95–105
- Schoenenberger K, Colston B W Jr, Maitland D J, da Silva L B and Everett M J 1998 *Appl. Opt.* **37** 6026–36
- Schwider J, Burov R, Elssner K E, Grzanna J, Spolaczyk R and Merkel K 1983 *Appl. Opt.* **22** 3421–32
- Schwider J 1990 *Prog. Opt.* **28** 273–359
- Semenov A T, Batovrin V K, Garmash I A, Shidlovsky V R, Shramenko M V and Yakubovich S D 1995 *Electron. Lett.* **31** 314–15
- Sergeev A M *et al* 1997 *Opt. Express*. **1** 432–40
- Sirohi R S 1993 *Speckle Metrology* (New York: Marcel Dekker)
- Sivak M V Jr, Kobayashi K, Izatt J A, Rollins A M, Ung Runyawee R, Chak A, Wong R C, Isenberg G A and Willis J 2000 *Gastrointest. Endosc.* **51** 474–9
- Sticker M, Hitzenger C K, Leitgeb R and Fercher A F 2001 *Opt. Lett.* **26** 518–20
- Sticker M, Pircher M, Goetzinger E, Sattmann H, Fercher A F and Hitzenger C K 2002 *Opt. Lett.* **27** 1126–8
- Steel W H 1983 *Interferometry* (Cambridge: Cambridge University Press)
- Superlum Diodes Ltd 2002 www.superlumdiodes.com
- Swanson E A, Huang D, Hee M R, Fujimoto J G, Lin C P and Puliafito C A 1992 *Opt. Lett.* **17** 151–3
- Swanson E A, Izatt J A, Hee M R, Huang D, Lin C P, Schuman J S, Puliafito C A and Fujimoto J G 1993 *Opt. Lett.* **18** 1864–6
- Szydio J, Delachenal N, Gianotti R, Walti R, Bleuler H and Salathe R P 1998 *Opt. Commun.* **154** 1–4
- Takada K and Yamada H 1996 *IEEE Phot. Tech. Lett.* **8** 658–60
- Tearney G J, Boppart S A, Bouma B E, Brezinski M E, Weissman N J, Southern F J, Fujimoto J G 1996a *Opt. Lett.* **21** 543–5
- Tearney G J, Bouma B E, Boppart S A, Golubovic B, Swanson E A and Fujimoto J G 1996b *Opt. Lett.* **21** 1408–10
- Tearney G J, Brezinski M E, Southern F J, Bouma B E, Boppart S A and Fujimoto J G 1997a *Am. J. Gastroent.* **92** 1800–4
- Tearney G J, Bouma B E and Fujimoto J G 1997b *Opt. Lett.* **22** 1811–13
- Tearney G J, Brezinski M E, Bouma B E, Boppart S A, Pitris C, Southern F J and Fujimoto J G 1997c *Science* **276** 2037–9
- Teramura Y, Suzuki K, Suzuki M and Kannari M 1999 *Appl. Opt.* **38** 5974–80
- Thrane L, Yura H T and Andersen P E 2000 *J. Opt. Soc. Am. A* **17** 484–90
- Thurber S R, Burgess L W, Brodsky A, Shelley P H 2000 *J. Opt. Soc. Am. A* **17** 2034–9
- Tripathi R, Nassif N, Nelson J S, Park B H, de Boer J F 2002 *Opt. Lett.* **27** 406–08
- Tuchin V V, Xu X and Wang R K 2002 *Appl. Opt.* **41** 258–71
- Vabre L, Dubois A and Boccara A C 2002 *Opt. Lett.* **27** 530–2
- Van Engen A G, Diddams S A and Clement T S 1998 *Appl. Opt.* **37** 5679–86
- van Leeuwen T G, Kulkarni M D, Yazdanfar S, Rollins A M and Izatt J A 1999 *Opt. Lett.* **24** 1584–6
- Vargas G, Chan E K, Barton J K, Rylander H G 3rd and Welch A J 1999 *Lasers Surg. Med.* **24** 133–41
- Vij D R and Mahesh K 2002 *Medical Applications of Lasers* (Boston: Kluwer)
- Wang R K 1999 *J. Mod. Opt.* **46** 1905–12
- Wang R K 2000 *J. Mod. Opt.* **47** 103–20
- Wang X J, Milner T E, de Boer J F, Z Y, Pashley D H and Nelson J S 1999 *Appl. Opt.* **38** 2092–6
- Wang X J, Milner T E and Nelson J S 1995 *Opt. Lett.* **20** 1337–9
- Watanabe W and Itoh K 2000 *Opt. Rev.* **7** 406–14
- Wax A, Yang C, Dasari R R and Feld M S 2001 *Appl. Opt.* **40** 4222–7
- Webb S 1988 *The Physics of Medical Imaging* (Bristol and Philadelphia: Adam Hilger)
- Weiner A M, Heritage J P and Kirschner E M 1988 *J. Opt. Soc. Am. B* **5** 1563–72

- Weiner A M, Leaird D E, Patel J S and Wullert J R 1990 *Opt. Lett.* **15** 326–8
- Welzel J 2001 *Skin. Res. Technol.* **7** 1–9
- Westphal V, Yazdanfar S, Rollins A M and Izatt J A 2002 *Opt. Lett.* **27** 34–6
- Wilson B C and Jacques S L 1990 *IEEE J. Quant. Electron.* **26** 2186–99
- Wojtkowski M, Leitgeb R, Kowalczyk A, Bajraszewski T and Fercher A F 2002a *J. Biomed. Opt.* **7** 457–63
- Wojtkowski M, Kowalczyk A, Leitgeb R and Fercher A F 2002b *Opt. Lett.* **27** 1415–17
- Wolf E 1969 *Opt. Commun.* **1** 153–6
- Wolman M 1975 *J. Histochem. Cytochem.* **23** 21–50
- Wong R C K, Yazdanfar S, Izatt J A, Kulkarni M D, Barton J K, Welch A J, Willis J and Sivak M V J 2002 *Gastrointest. Endosc.* **55** 88–95
- Xiang S H, Zhou L and Schmitt J M 1998 *Proc. SPIE* **3196** 79–88
- Xu F, Pudavar H E and Prasad P N 1999 *Opt. Lett.* **24** 1808–10
- Yao G and Wang L V 1999 *Opt. Lett.* **24** 537–9
- Yasuno Y, Sutoh Y, Nakama M, Makita S, Itoh M, Yatagai T and Mori M 2002a *Opt. Lett.* **27** 403–5
- Yasuno Y, Makita S, Sutoh Y, Itoh M and Yatagai T 2002b *Opt. Lett.* **27** 1803–5
- Yazdanfar S, Rollins A M and Izatt J A 2000 *Opt. Lett.* **25** 1448–50
- Yazdanfar S, Rollins A M and Izatt J A 2001 *Proc. SPIE* **4251** 156–64
- Yeh Y and Cummins H Z 1964 *Appl. Phys. Lett.* **4** 176–8
- Yung K M, Lee S L and Schmitt J M 1999 *J. Biomed. Opt.* **4** 125–36
- Yura H T 1979 *Opt. Acta* **26** 627–44
- Zangwill L M, Bowd C, Berry C C, Williams J, Blumenthal E Z, Sanchez Galeana C A, Vasile C and Weinreb R N 2001 *Arch. Ophthalmol.* **119** 985–93
- Zeylikovich I, Gilerson A and Alfano R R 1998 *Opt. Lett.* **23** 1797–9
- Zhang Y, Sato M and Tanno N 2001a *Opt. Commun.* **187** 65–70
- Zhang Y, Sato M and Tanno N 2001b *Opt. Commun.* **192** 183–92
- Zhang Y, Sato M and Tanno N 2001c *Opt. Lett.* **26** 205–7
- Zhao Y, Chen Z, Saxer C, Shaohua X, de Boer JF and Nelson J S 2000 *Opt. Lett.* **25** 114–16
- Zhao Y, Chen Z, Ding Z, Ren H and Nelson J S 2002 *Opt. Lett.* **27** 98–100
- Zuluaga A F and Richards Kortum R 1999 *Opt. Lett.* **24** 519–21
- Zvyagin A V, Fitzgerald J B, Silva K K M B D and Sampson D D 2000 *Opt. Lett.* **25** 1645–7